International
Progress Report

IPR-03-05

Äspö Hard Rock Laboratory

Äspö Pillar Stability Experiment

Modelling of fracture stability by Fracod
Preliminary results

Mikael Rinne
Shen Baotang
Lee Hee-Suk

Fracom

March 2003

Svensk Kärnbränslehantering AB
Swedish Nuclear Fuel
and Waste Management Co
Box 5864
SE-102 40 Stockholm Sweden
Tel +46 8 459 84 00
Fax +46 8 661 57 19

Äspö Hard Rock Laboratory

Report no.	No.
IPR-03-05	F86K
Author	Date
Mikael Rinne Shen Baotang Lee Hee-Suk	2003-03-26
Checked by	Date
Christer Andersson Derek Martin	2003-03-31
Approved	Date
Christer Svemar	2003-05-22

Äspö Hard Rock Laboratory

Äspö Pillar Stability Experiment

Modelling of fracture stability by Fracod Preliminary results

Mikael Rinne
Shen Baotang
Lee Hee-Suk

Fracom

March 2003

Keywords: APSE, modelling, fracture initiation, fracture propagation, spalling, AE

Abstract

An in-situ experiment is planned at Äspö HRL to investigate the stability of a pillar between two closely located boreholes of deposition hole scale. This full-scale experiment is named the Äspö Pillar Stability Experiment (APSE).

One of the holes will be pressurized with 1 MPa water pressure to simulate confinement by backfill. Thermal stresses will be applied in the pillar by the use of electric heaters to reach the spalling conditions. To quantify the degree of damage during the experiment, an Acoustic Emission (AE) system used and strain measurements will be made.

FRACOD is a two dimensional BEM/DDM code for fracturing analysis in rock material. Here it has been used to model the rock mass response during the planned sequences of excavation-confinement-heating. The models can predict the stress and displacement fields, fracture initiation and propagation, coalescence and the final failure of the rock mass. The presence of pre-existing fractures, which may have significant influence on the pillar behaviour, have also been considered in modelling. This report summarises the work made to update FRACOD and to apply it for various experimental stages.

The report is consisted of 3 parts:

Part I

Two FRACOD models, "Far-field model" and "Pillar model", are presented. The "Far-field model" simulates excavation in an infinite medium without external stress boundaries. The effects of heat induced stresses and the 3D effects caused by the deposition tunnel have been accurately simulated by the "Pillar model".

Part II

FRACOD development has been extended to predict fracture initiation from intact rock and Acoustic Emission (AE) events. Barton-Bandis model has been applied to estimate the fracture properties for newly initiated fractures. The implementation process for the new developments and options has been presented.

Part III

A new boundary element technique to reconstruct the stress distribution obtained from other coupled codes for excavation and thermal modelling is presented. The method has been successfully used to transfer excavation and heat induced stresses from EXAMINE3D and JobFem model into FRACOD.

Fracturing processes and AE events have been evaluated at each stage of heating. The results from this study suggest that the planned test configuration is close to the limit of fracture initiation of microcracks around the boreholes. Slight fracturing may take place at the pillar walls before heating. During thermal loading the pillar may lead to minor spalling. According to preliminary results the effect of pre-existing fractures on the rock mass response seems to be significant.

Sammanfattning

Ett fullskaligt in-situ försök har planerats vid Äspö HRL för att fördjupa kunskaperna i stabiliteten av en pelare mellan två närstående deponeringshål. Detta försök har utnämnts till Äspö Pillar Stability Experiment (APSE).

Ett av deponeringshålen skall pressas med vattentryck av 1 MPa för att simulera svälltrycket av bentonitbuffert. Berget i pelaren skall värmas upp med elektriska värmeelement. Tillskottsspänningar från bergets termiska expansion skall driva berget till brott i hålväggarna. Akustisk emissionsteknik (AE) skall användas och deformations mätningar skall utföras för att utvärdera sprickbildandet inne i pelaren.

FRACOD är en tvådimensionell BEM/DDM kod för sprickanalyser i bergmaterial. Här har koden använts för att modellera bergmassans respons för de planerade faserna av berguttag - vattentryck - uppvärmning. FRACOD modellerna förutser spänningar och deformationer, sprickinitiering och -propagering, sammanväxta sprickor och brott i berget. Bergmassans befintliga sprickor som kan påverka pelarens stabilitet under varierande spänningsförhållanden, har tagits hänsyn till. Denna rapport beskriver modellerna samt de insatser som har utförts för att uppdatera och applicera FRACOD för det planerade försöket.

Rapporten består av tre avgränsade delar;

Part I

Två FRACOD modeller, “Far-field model” och “Pillar model” presenteras. ”Far-field modellen” modellerar berguttag i ett infinit medium utan externa ränder. Värmeinducerade spänningar och inverkan av 3D spänningsfältet orsakad av den närvarande deponeringstunneln har modellerats mer detaljerat med hjälp av ”Pelaremodellen”.

Part II

Utveckling av FRACOD har bedrivits under modelleringsperioden för att kunna förutse sprickinitiering i intakt bergmaterial samt för att kunna modellera akustiska (AE) händelser. Barton-Bandis model har tillämpats för att uppskatta nybildade sprickors egenskaper. Kodutveckling och implementering av de nya egenskaperna i koden beskrivs.

Part III

En ny randelementteknik för att kunna rekonstruera spänningsfält från andra kopplade modeller har presenteras. Den nya metoden har framgångsrikt använts för att hemföra spänningar orsakade av berguttag och värmeflöde från modeller av EXAMINE3D och JobFem till FRACOD.

Med hjälp av modellen kan brottprocessen och ökad AE aktivitet successivt förutses under olika skeden av belastningscykeln. Modelleringsresultaten föreslår att den planerade borrhåls- och spänningskonfigurationen är nära gränsen för sprickinitiering av mikrosprickor vid ränderna av borrhålen. Ringa mängd av sprickbildning kan ske innan uppvärmning. Under den termiska belastningsperioden föreslår beräkningarna att de ökade spänningarna kommer att driva bergpelaren till en begränsad enhet i brott.

Contents

Part I:

Modelling Fracturing Process with Preliminary Data by FRACOD

Part II:

Modelling Fracture Initiation and Acoustic Emission (AE) Using FRACOD

Part III:

Reconstruction of Stress Field Using an Inverse Technique for the APSE Pillar Model

Part I:

Modelling Fracturing Process with Preliminary Data by FRACOD

Mikael Rinne, Baotang Shen, Hee-Suk Lee

Fracom Ltd.

February 2003

Contents of Part I

1 Introduction 13

2 Overview of the APSE project 15
2.1 Objectives 15
2.2 Excavation and loading steps of the planned APSE 15
2.3 Numerical methods and modelling teams 16

3 Preliminary APSE site data 19
3.1 Rock and fracture properties 19
3.2 Stress conditions 21

4 FRACOD models 23
4.1 Boundary conditions 23
4.2 Far-field models 24
4.2.1 One borehole model 24
4.2.2 Two borehole model 25
4.2.1 Summary of the results 28
4.3 Pillar models 29
4.3.1 Section 1.5 m below the tunnel floor 30
4.3.2 Section 0.5 m below the tunnel floor 34
4.3.3 AE evolution 37
4.3.4 Deformation at the pillar boundaries 40
4.3.5 Summary of the results 43

5 Effect of pre-existing fractures and fracture properties 45
5.1 Effect of the pre-existing fracture geometry 45
5.1.1 Crossing fractures with borehole 45
5.1.2 Non-crossing fractures with borehole 46
5.1.3 Effect of large fractures 46
5.1.4 Pillar model 47
5.1.5 Summary of the results 48
5.2 Fracture properties 48
5.2.1 Pre-existing fractures 48
5.2.2 Newly created fractures 49
5.2.3 Summary of the results 51

6 Discussion on fracturing process 53
6.1 Spalling and failure mechanism in boreholes 53
6.2 Fracture mechanism in FRACOD 55
6.3 Involved uncertainties for prediction 58

7 Concluding remarks 61

8 References 63

1 Introduction

An in-situ experiment is planned at Äspö HRL to investigate the stability of a pillar between two closely located deposition holes. This full-scale experiment is named the Äspö Pillar Stability Experiment (APSE).

The experiment requires a new tunnel that is excavated at the 450 m level. In the tunnel two large holes with a diameter of 1.8 m and a depth of 6 m will be bored. The holes will be spaced to create a pillar with the width of 1 m between them. The tunnel will be designed to induce the stresses in the pillar to a stress level close to the limit of spalling. Electric heaters will be used to induce thermal stresses in the pillar that would force the rock in the pillar walls to spall. To simulate the effect of confinement from backfill in real deposition hole, a water pressure of 1 MPa will be applied in one of the holes. The effect of the confining pressure will be further studied by gradually releasing it. The whole experimental stages will be monitored by an acoustic emission (AE) and micro-seismic system. Convergence and strain measurements will also be made in the open hole to check the rock mass behaviour around the boreholes.

The modelling should include the planned steps of excavation-confinement-heating sequence to predict the degree of spalling and fracturing stress and displacement fields together with temperature fields in the pillar region.

FRACOD is a boundary element code for fracture stability analysis in rock material. It has been developed to model fracturing process of the rock material in varying loading conditions. For the APSE project, FRACOD has been updated in many respects including AE monitoring, enhancement of the accuracy to predict fracturing processes and capability to import stresses from other numerical models.

Barton-Bandis model has been applied to estimate the fracture properties for new initiated fractures /Barton 1986, 2002/ and /Bandis, 1986/. The mathematical treatment has been described in Part II, Appendix A. The fracture initiation from intact rock and the AE prediction option are described in Part II: “Modelling Fracture Initiation and Acoustic Emission (AE) Using FRACOD”.

For the simulation of experimental stages, thermal loading should be considered in the FRACOD. However, the current FRACOD cannot directly simulate the effect of thermal loading and an alternative way to transfer thermal and initial stresses from other coupled numerical models has been sought. An inverse boundary element technique to reconstruct stress field for FRACOD calculations has been developed. The data transfer process has been described in Part III.

This part summarizes the results from preliminary FRACOD models. Two kinds of models have been used to simulate fracturing process in the pillar: the “Far-field model” and the “Pillar model”. The “Far-field model” simulates the effect of excavations in infinite medium without external boundaries. Far-field models are also used for estimating parameter sensitivity, effect of pre-existing fractures and numerical stability. To simulate real heating process and 3D excavation effects, the “Pillar model” is used with the aid of the stress reconstruction technique. The effects of pre-existing fractures have also been studied with preliminary data.

2 Overview of the APSE project

2.1 Objectives

The major objectives of the Äspö Pillar Stability Experiment are:

(1) To demonstrate the capability to predict spalling in a fractured rock mass.

(2) To investigate the effect of the backfill (confining pressure) on the rock mass response.

(3) Comparison of 2D and 3D mechanical and thermal predicting capabilities.

Two key components of the FRACOD modelling work are:

(1) To predict properly the fracturing process during the planned sequences of excavation-confinement-heating.

(2) To develop and demonstrate the capacity of FRACOD in predicting Acoustic Emission (AE) during the progressive fracturing process in the pillar.

2.2 Excavation and loading steps of the planned APSE

The description of the planned experiment, instrumentation and the results of preliminary numerical calculations are reported in /Andersson, 2003/ and in /Fredriksson et al., 2003/. These reports present the layout of the experiment, with the locations of the AE monitoring sensors, the heaters and the temperature measurement points during the experiment.

The main APSE excavation and loading steps are as follows:

(a) Excavation of a test tunnel, 5m by 7.5 m in size, with an inverse floor arch at 450 m below ground surface.

(b) Installation of instrumentation, including AE transducers and heaters.

(c) Drilling of the first deposition hole of 1.8 m in diameter, 6 m in depth.

(d) Pressuring the first hole with watertight membrane up to 1 MPa to simulate the effects of swelling pressure of backfill.

(e) Drilling of the second deposition hole (1m pillar thickness).

(f) Heating the pillar with electrical heaters installed near the two deposition holes. The heating continues until failure of the wall of the deposition hole occurs.

(g) Gradual reduction of the confining pressure in the first deposition hole until spalling occurs.

2.3 Numerical methods and modelling teams

A feasibility study for performing the APSE was made by SKB /Andersson, 2003/. The study identifies risks and describes the strategy for the modelling. Also the stress redistribution caused by tunnel and borehole excavation was preliminary analysed using the boundary element code EXAMINE3D and the finite element code PHASE2D.

Three teams and several different numerical codes have been used to simulate the loading steps of the APSE experiment (see Figure 2-1):

Golder Associates performed 2D-coupled thermo-mechanical modelling with the finite element code JobFem. Results from two horizontal cross sections (0.5 m and 1.5 m below the tunnel floor) are obtained in order to consider the difference in stress distribution due to 3D effects. The initial stress distribution after excavation at two levels from the EXAMINE3D modelling has been used to calculate total stresses after heating with JobFem. Different locations of the heaters have been tested /Fredriksson et al., 2003/. Figure 2-2 presents the proposed layout of acoustic emission system and the heaters from the calculation.

Saanio&Riekkola performed 3D-coupled thermo-mechanical modelling with the finite element code FLAC3D /Wanne, 2003/. A 2D-PFC analysis is planning to be performed at later stages.

Fracom performed the simulation of fracturing process using FRACOD to predict explicitly fracturing process of rocks in varying loading conditions.

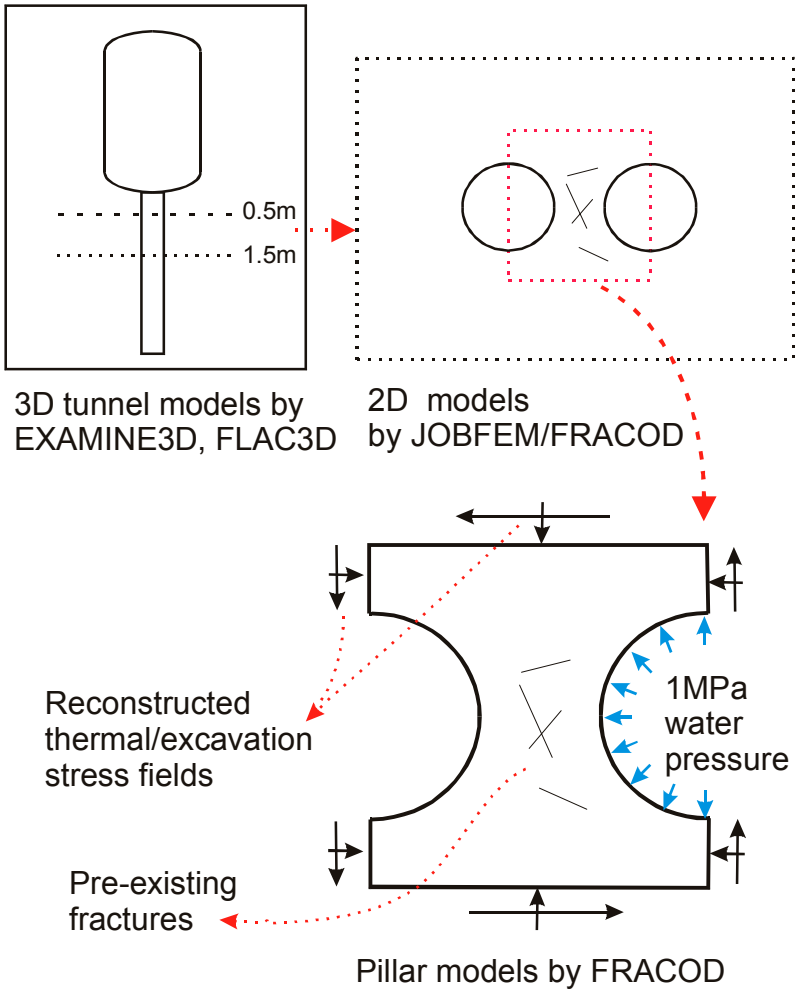

Figure 2-1. *Numerical methods and model geometries used in APSE.*

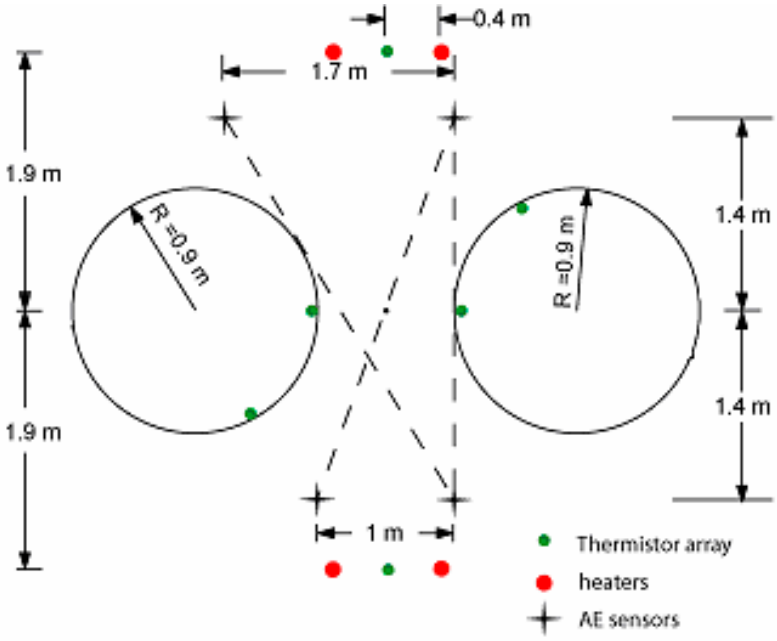

Figure 2-2. *Planned borehole geometry and instrumentations /Fredriksson et al., 2003/.*

3 Preliminary APSE site data

3.1 Rock and fracture properties

All geology and stress data of the rock in the experimental volume are summarized in /Janson et al., 2003/. Also properties based on laboratory investigations by /Nordlund et al., 1999/ and /Klee et al., 2001/ have been considered in modelling. Table 3-1 lists parameters used for FRACOD modelling.

Table 3-1. Input data for FRACOD models.

Parameter	Value and unit
Intact rock	
Young's modulus, intact rock:	68 GPa
Poisson's ratio for intact rock:	0.24
Cohesion, intact rock	31 MPa
Friction angle, intact rock	49°
Tensile strength σ_t	14.8 MPa
Fractures	
Fracture toughness in mode I	2.54 MPa*m$^{1/2}$
Fracture toughness in mode II	6.35 MPa*m$^{1/2}$
Normal stiffness, K_n for pre-existing (old) fractures	61.5 GPa/m
Shear stiffness, K_s for pre-existing (old) fractures	35.5 GPa/m
Fracture friction angle	31°
Cohesion of pre-exiting fractures	1 MPa
Properties of newly created fresh fractures	See Table 3-2 and Table 3-3

For the FRACOD models the rock material has been assumed to be homogeneous, isotropic and linear elastic. In the following it is briefly described how some of the parameters are determined.

Young´s modulus and Poisson's ratio

Young´s modulus and Poisson's ratio have been determined by laboratory investigation on cores from boreholes KA2599G01 and KF0093A01.

Fracture toughness

Fracture toughness K_{IC} of rocks near Äspö area has been determined by /Klee et al., 2001/.

According to laboratory test using anti-symmetric four-point bending test, the K_{IIC} is 2-3 times K_{IC} /Rao, 1999/. For this study we apply

K_{IIC} =2.5, K_{IC}=6.35 MPa*m$^{1/2}$.

Fracture stiffness for pre-exist fractures (joints)

The fracture properties have been investigated by /Stille and Olsson,1989/, /Olsson, 1998/ and /Lanaro, 2001/ for fracture cores in the Äspö HRL and /Staub et al., 2002/ re-evaluated their results. According to Staub the normal and shear stiffness for sub-vertical fractures (old joints) are:

Normal stiffness, K_n: 61.5 GPa/m

Shear stiffness, K_s: 35.5 GPa/m

Fracture stiffness, particularly the normal stiffness, is highly stress dependent. The higher the normal load on fractures, the higher is stiffness. The above reported stiffness values are defined at a normal stress of 23 MPa.

Fracture properties of newly created fractures

Fresh fractures generated from fracture initiation and propagation often have very different stiffness values from those of the old joints. There are very limited test data available for the newly created fresh fractures. To provide an estimation of the fracture stiffness for the APSE project, the following factors have been considered: Values have to be theoretically sound and realistic. They also have to be feasible to implement in FRACOD. Barton-Bandis model has been used to estimate the normal stiffness of the new fractures (see Part II, Appendix A). The shear stiffness obtained from the Barton-Bandis model was found to be too low for modelling random fracture initiation in FRACOD due to numerical reasons. Therefore the elastic shear deformation has been restricted and only fracture sliding causes shear deformation. Restricting shear and/or normal elastic deformation is common in solid mechanics when dealing interface or contact problem /Zang, 1990/.

The newly created fractures are also assumed to have the same friction angle and cohesion as the intact rock. Once sliding occurs, however, the cohesion will become zero. The dilation of the new fresh fracture is also estimated using the Barton-Bandis model (see Part II, Appendix A). It is found that the dilation has major effect on the failure process.

The fracture properties are estimated separately for tensile fracture and shear fractures. Due to the difference in surface roughness, tensile fractures and shear fractures have different stiffness and dilation values.

The estimated fracture properties for the APSE project are given below:

Table 3-2. Properties for newly created fractures --- Shear fractures

K_n	4643 (GPa/m)
Friction angle	49.0 (°)
Cohesion	31 (MPa)
Dilation angle	2.3 (°)

Table 3-3. Properties for newly created fractures --- Tensile fractures

K_n	320 (GPa/m)
Friction angle	49.0 (°)
Cohesion	31 (MPa)
Dilation angle	12.1 (°)

3.2 Stress conditions

The summarized in-situ stress measurement results have been presented in /Janson et al., 2003/. The most probable value of major stress in the experimental volume is estimated as:

σ_1: 30 MPa and an orientation of 310/30,

σ_2: 15 MPa and an orientation of 082/53,

σ_3: 10 MPa and an orientation of 210/20.

FRACOD is a two dimensional code. For the Far-field model, it is approximated that the major stress is perpendicular to the tunnel (σ_1=30 MPa) and the minor stress is parallel to the tunnel (σ_3 =10 MPa) Figure 3-1.

The stress condition in the Far-field model corresponds to the horizontal section at the bottom of the borehole, where the effect of the deposition tunnel is not essential.

The effects of induced thermal stresses and the 3D effects caused by the close deposition tunnel have been taken into account by the "Pillar model" (see Part III).

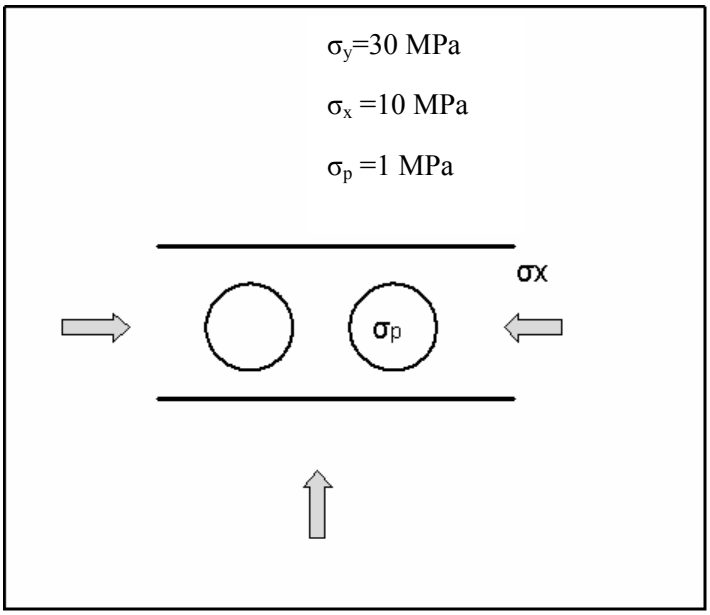

Figure 3-1. *Far-field borehole model (borehole radius=1.8 m, pillar width=1 m).*

4 FRACOD models

4.1 Boundary conditions

The “Far-field models” simulate the rock mass response in an infinite medium with the far-field stresses (σ_y and σ_x).

The thermal load or highly disturbed stresses in the pillar due to 3D excavation is not possible to consider accurately with homogeneous far-field stress field. The accurate pillar stresses during excavation and heating, have been modelled by EXAMINE3D and JobFem. Internal stresses from JobFem models were reconstructed using proper boundary stresses for the Pillar model in FRACOD. The data transfer process has been described in Part III.

In FRACOD four boundary conditions are available:

(1) Shear stress and normal stress boundary,

(2) Shear displacement and normal displacement boundary,

(3) Shear displacement and normal stress boundary,

(4) Shear stress and normal displacement boundary.

For the Pillar model displacement boundary conditions (2) have been applied on the top, bottom and side boundaries of the pillar model (see Figure 4-1).

Stress boundary conditions (1) have been applied to the borehole boundaries for all models. The backfill pressure in the borehole is modelled by applying 1 MPa normal stress and zero shear stress on the borehole boundary.

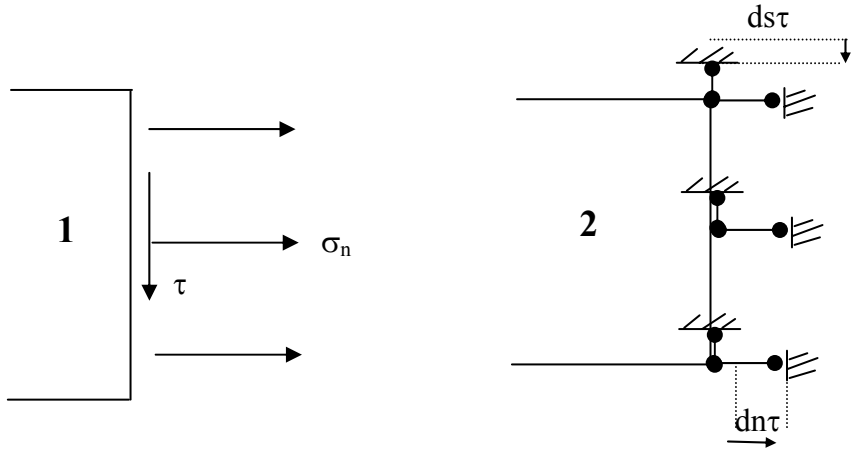

(a) ***(b)***

Figure 4-1. *Used boundary conditions for the FRACOD. (a) Stress boundary condition. (b) Displacement boundary condition.*

4.2 Far-field models

The modelling work with FRACOD was initiated by establishing models of two closely located boreholes in a uniform stress environment to consider various excavation cases. Far-field models also assist to study the fracture mechanism in simplified stress conditions, to estimate parameter sensitivity and to study the effect of pre-existing fractures. It should be mentioned that the Far-field models have low accuracy, and they do not correctly consider the 3D loading conditions in the APSE pillar.

The far-field stresses of:

σ_x =10 MPa (parallel to the tunnel)

σ_y=30 MPa (perpendicular to the tunnel)

have been applied to all models as explained in section 3.2.

4.2.1 One borehole model

The “One borehole model" predicts the rock mass response caused by excavation of the primary borehole.

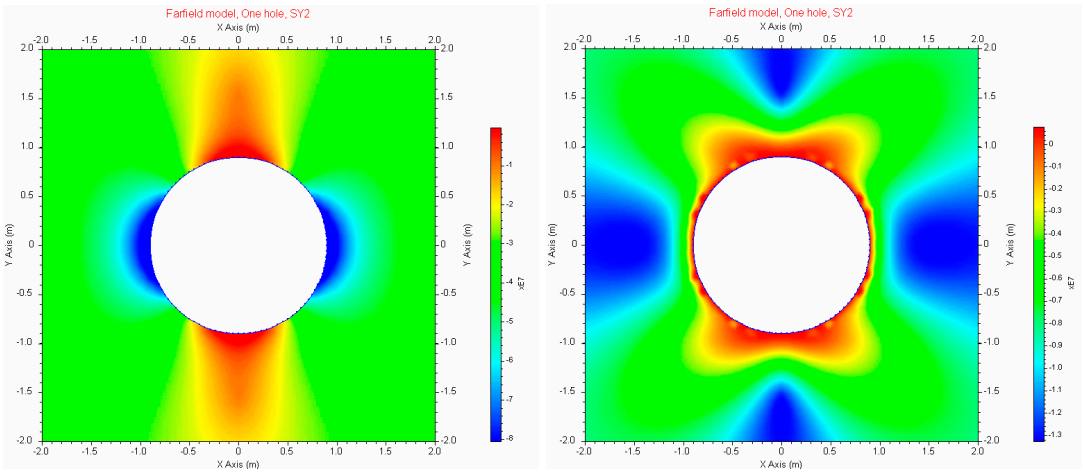

(a) ***(b)***

Figure 4-2. *Induced stresses from one borehole model after applying far-field stresses of σ_x/σ_y= 10 MPa/30 MPa. (a) Major principal stress (σ_1). (b) Minor principal stress (σ_3).*

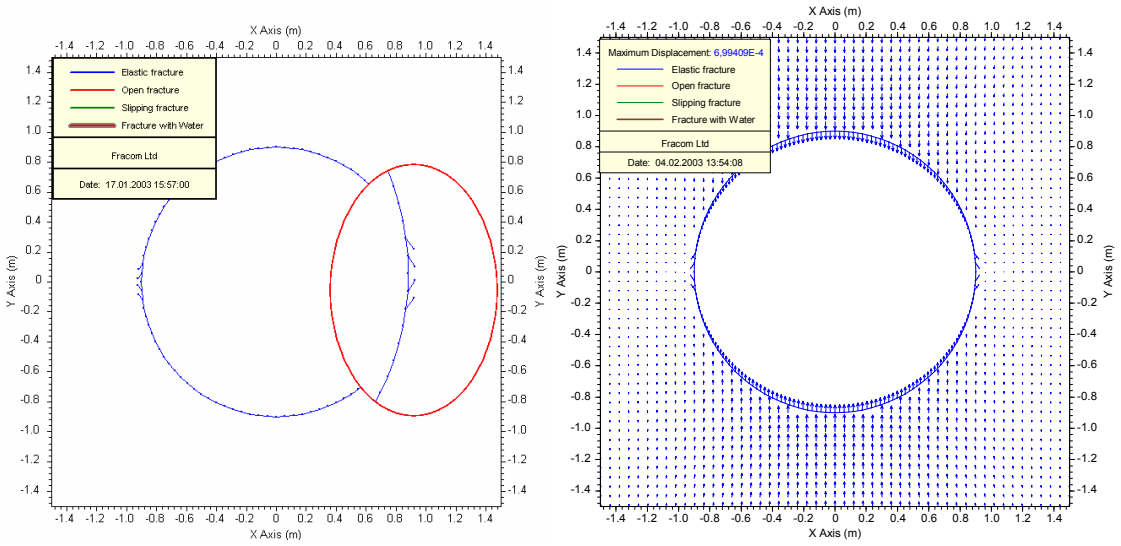

(a) ***(b)***

Figure 4-3. *(a) Fracture initiation at the borehole boundary after applying far-field stresses of σ_x/σ_y=10.5 MPa/31.5 MPa. (b) Displacement contour, maximum displacement is 0,7mm.*

The maximum induced compressive stress at the borehole boundary is approximately 80 MPa and there are no tensile stresses (Figure 4-2). The model does not suggest any fracture initiation at this level of applied far-field stresses. However, the external stresses have to be increased only by 5 % to initiate fractures at the borehole boundary though overall behaviour remains elastic (Figure 4-3).

4.2.2 Two borehole model

The "Two borehole model" aims to describe the general behaviour of a borehole/pillar system with increasing homogeneous far-field stress system. The following examples do not present any particular level of the borehole although they cover the predicted induced stress range in the pillar. One borehole (at right presented in all figures) is confined with 1 MPa internal pressure to simulate the effect of swelling pressure of bentonite.

In the first example the stress condition (σ_x/σ_y=10 MPa/30 MPa) corresponds to stresses at the bottom of the borehole after excavation. The maximum induced stress in the pillar at the borehole boundary is about 94 MPa (Figure 4-4). Calculations suggest minor fracture initiation to take place in the pillar and in the borehole boundary at the opposite sides of the pillar (see Figure 4-5a). The far-field stress is increased to correspond to heating induced stresses in the pillar. Increasing the far-field stresses to σ_x/σ_y=10 MPa/ 39 MPa causes slight tensile fracturing in the borehole boundary and the new initiated fractures propagate in the direction of major principal stress (see Figure 4-5b).

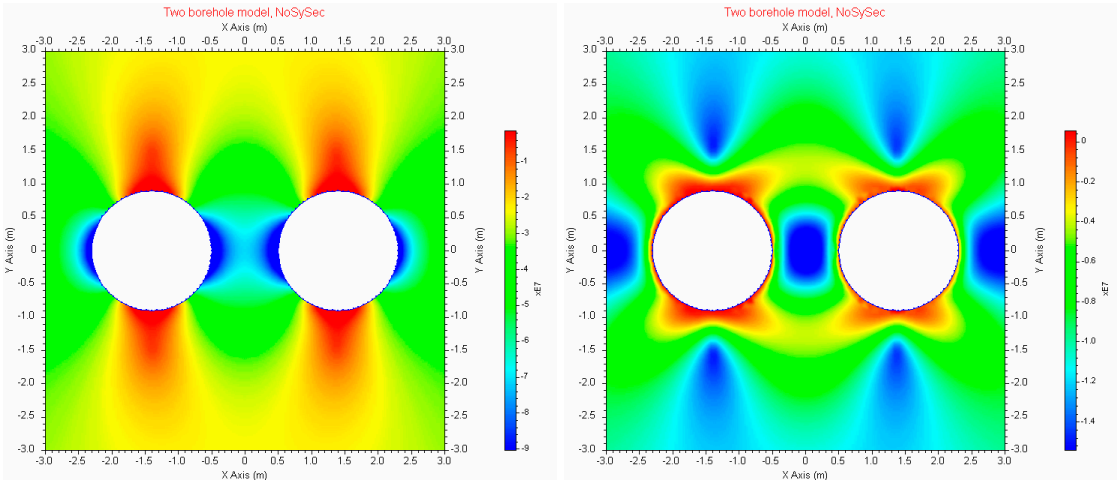

(a) ***(b)***

Figure 4-4. *Stress distribution around two boreholes after applying far-field stresses of σ_x/σ_y= 10 MPa/30 MPa. (a) Major principal stress (σ_1). (b) Minor principal stress (σ_3)*

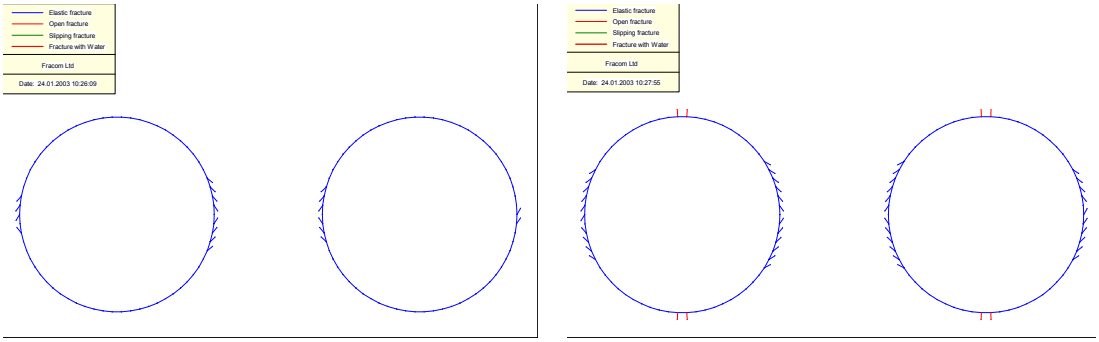

(a) ***(b)***

Figure 4-5. *Fracture initiation around the boreholes after applying far-field stresses (the borehole at right in both figures is confined with 1 MPa internal pressure). (a) 10 MPa/30 MPa. (b) 10 MPa/39 MPa.*

In the following cases the far-field stress of σ_x=10 MPa (parallel to the tunnel) was kept constant while σ_y (far-field stress perpendicular to the tunnel) was increased in 5 MPa steps. Fracture pattern after every 10 MPa step is presented (see Figure 4-6). The maximum induced compressive stresses presented here are taken from fractured models.

At σ_x/σ_y =10 MPa/40 MPa (Figure 4-6 (b)), the maximum induced compressive stress in the pillar is about 125 MPa. Some fractures start to propagate at the unconfined (left) borehole boundary. However, the fracturing is still very limited and most fractures remains in elastic state.

When the stress is increased to σ_x / σ_y=10 MPa/50 MPa (Figure 4-6 (c)), the resultant maximum stress at the borehole boundary is approximately 158 MPa. Most of the formerly initiated fractures start to propagate, coalesce and they can form small blocks. Fracture initiation in the intact rock also takes place. This stress level can be regarded as a critical condition for possible unstable spalling under homogeneous stress condition.

When the stress is increased to σ_x / σ_y= 10 MPa/60 MPa (Figure 4-6 (d)), the maximum stress at the borehole boundary is approximately 190 MPa in the elastic model (without fracturing) and in the fractured model about 180 MPa. This level can be regarded to be similar to stress in the upper part of the borehole (0.5 below the tunnel floor) after 120 days of heating. Fractures initiated in the rock mass start to propagate. Damage extends about 0.2 m into the pillar.

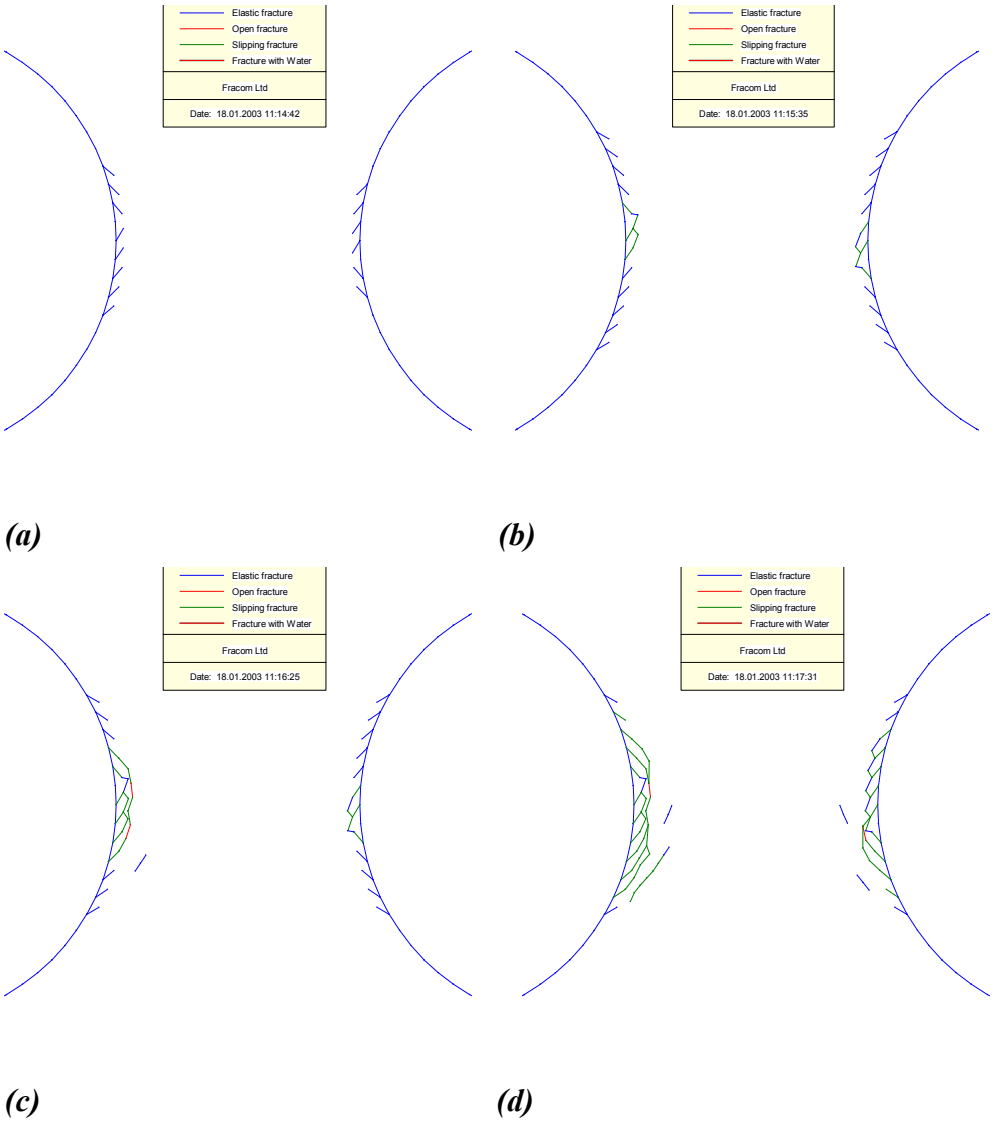

Figure 4-6. *Fracture initiation in the pillar after applying incremental far-field stresses. (a) 10 MPa/30 MPa. (b) 10 MPa/40 MPa. (c) 10 MPa/50 MPa. (d) 10 MPa/60 MPa. Blue line: fracture in elastic state, red line: open fracture, green line: slipping fracture, shear movement takes place along the fracture surface.*

According to simulations the model is still stable and the core of the pillar remains intact. With further increasing the stress to 70 MPa extensive fracturing and spalling will occur (see Figure 4-7).

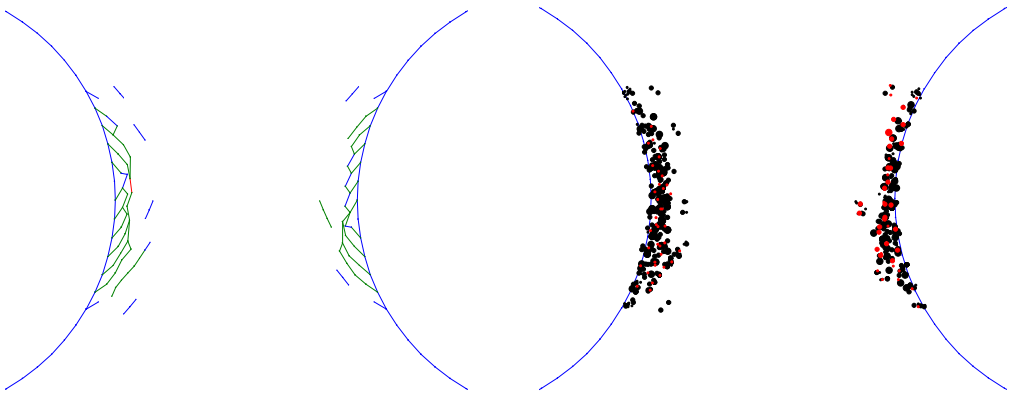

(a) ***(b)***

Figure 4-7. *The rock mass response in the pillar after applying far-field stresses of 10 MPa/70 MPa. (a) Fracture pattern. (b) AE events.*

4.2.1 Summary of the results

The planned borehole configuration is close to the limit of fracture initiation around the boreholes with given material properties and in-situ stress conditions. Slight fracture initiation and propagation may take place in the pillar and on the opposite sides of the pillar already before heating. However, such fracturing means slight damage of the boreholes, and overall pillar behaviour remains stable.

Loading configuration corresponding to the stress conditions in the upper part of the borehole after heating (0.5 m below the tunnel floor and 120 days of heating) will lead to extensive fracturing and spalling in the pillar region. Damage extends about 0.2 m in the pillar. However, the models are still stable and the core of the pillar remains intact.

The confining pressure of 1 MPa impacts clearly the borehole stability. Confinement in the right borehole stabilises the borehole wall during all stages of loading. It must be noted that in the Far-field model, excavation of the borehole and the confinement have been modelled to take place simultaneously. In the Pillar model the confinement is applied after excavation.

4.3 Pillar models

Pillar models have been established to study fracture initiation and propagation in the stress field elevated by thermal loading. The Pillar models aims to consider more correct and detailed stress field around pillar region compared to Far-field models.

Two sections have been modelled, those are 1.5 m and 0.5 m below the tunnel floor.

The influence on initial stresses caused by excavation of the tunnel and boreholes was modelled with EXAMINE3D by SKB. The induced stresses by heating were calculated with JobFem by Golders. The stress analysis has been described in /Andersson, 2003/ and /Fredriksson et al., 2003/.

The stresses in the Pillar model have been reconstructed from preliminary modelling data with EXAMINE3D and JobFem models with a method developed by Fracom Ltd. The code and the data transfer process, as well as the stress distribution in the pillar has been described in Part III.

Figure 4-2 and Figure 4-3 in Part III are used to simulate the 3D stresses in the pillar model. As it can be checked in the figures, good agreement is shown between original and reconstructed stress distribution. The stress data-set from other modelling calculations include the following phases:

- Stress state I: Stress conditions after excavation of both boreholes (EXAMINE3D).
- Stress state II: stresses after 30 days of heating (JobFem)
- Stress state III: stresses after 60 days of heating (JobFem)
- Stress state IV: stresses after 90 days of heating (JobFem)
- Stress state V: stresses after 120 days of heating (JobFem)

The effect of 1 MPa hydraulic pressure in one of the boreholes has been included in the stress data defining the thermally induced stresses by heating.

Due to 3D stress distribution, the stresses are unevenly distributed in the pillar and non-symmetric models were used (Figure 4-8).

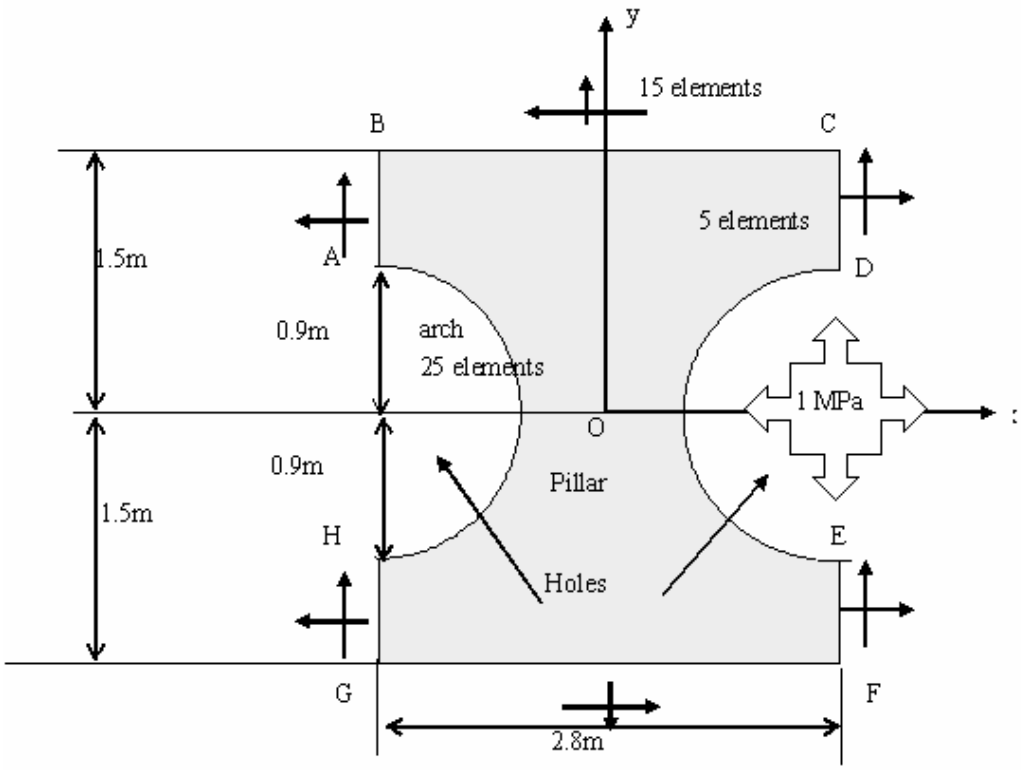

Figure 4-8. *FRACOD Pillar model.*

For the Pillar models in Figure 4-8, shear and normal displacement boundary conditions are used for top, bottom and sides of the model to reduce numerical instability. Both boreholes are modelled by stress boundary conditions. The backfill pressure in the borehole at right is modelled by applying 1 MPa normal stress on the borehole boundary.

4.3.1 Section 1.5 m below the tunnel floor

(1) Effect of excavation

Here the Pillar model represents the effect of excavation on pillar stability. The maximum compressive stress in the pillar boundary after excavation of both boreholes is about 122 MPa. This stress will cause some elastic fracture initiation at the borehole boundary (see Figure 4-9). After slight fracture initiation, the maximum stress will drop to 115 MPa. This kind of fracture initiation can be regarded as limited damage around the borehole wall. In practice, this slight fracturing is difficult to visually distinguish from the damage caused by mechanical borehole drilling.

After stresses (Figure 4-9 (b)) have been redistributed due to fracture initiation, higher stressed areas are formed in the vicinity of the central pillar wall. Displacement vectors (Figure 4-9 (c)) near central walls are very small compared to areas perpendicular to the tunnel line, and overall deformation remains elastic.

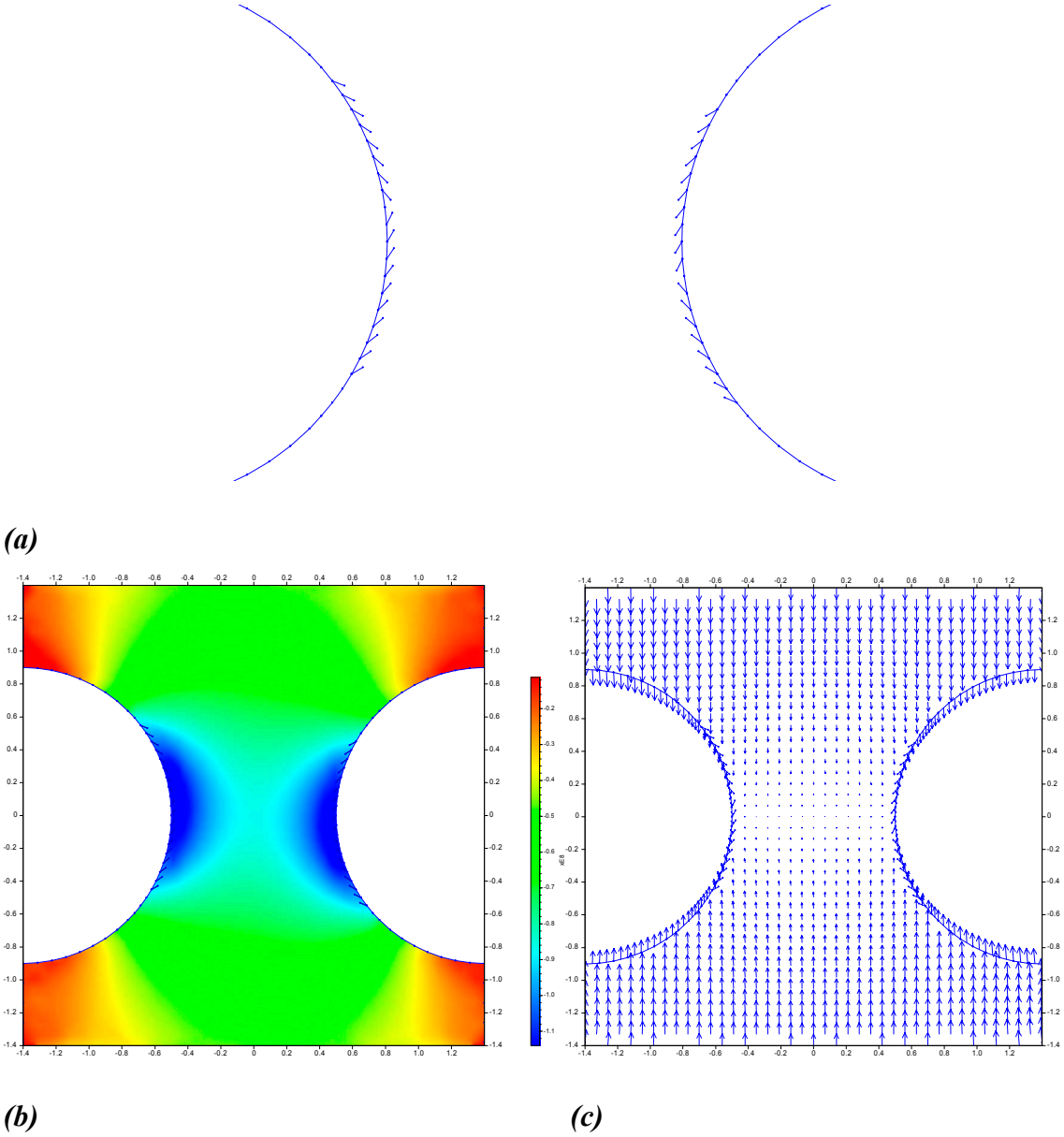

(a)

(b) ***(c)***

Figure 4-9. *Fracture initiation at the borehole boundary caused by stress concentration after excavation of the boreholes at 1.5 m below the tunnel floors. (a) Fracture pattern. (b) Stress contour. (c) Displacement vectors. See maximum displacements in Table 4-2.*

The confining stress of 1 MPa (in the borehole to the right, see Figure 4-9) was applied after excavation and after the preliminary fracture initiation was happen. Confinement seems not to induce additional fracture initiation or propagation.

(2) Effect of temperature increase

- **30 and 60 days of heating**

After applying the thermal stresses, the fracture initiation and propagation continues to develop as stresses increase (Figure 4-10) at the central pillar region. Calculations suggest that limited fracture propagation and coalescence might occur in the vicinity of the central borehole walls after 30 days of heating.

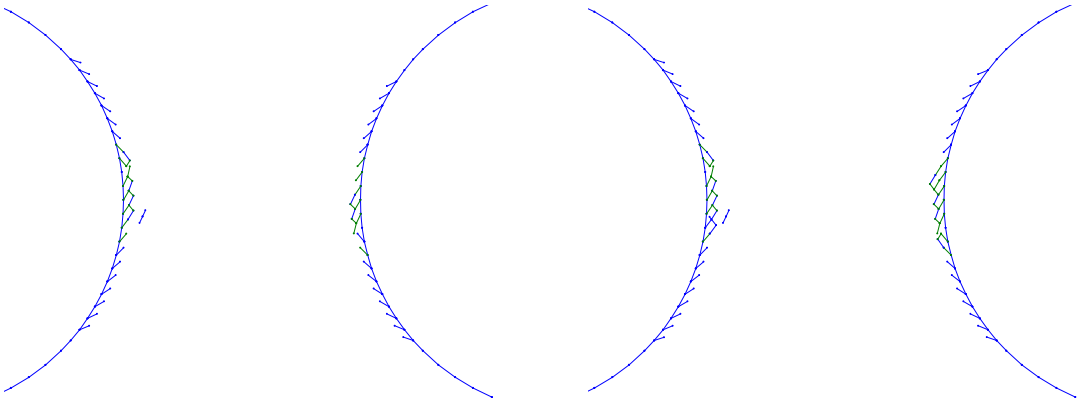

(a) ***(b)***

Figure 4-10*. Fracture initiation at the borehole boundary caused by thermal stresses at 1.5 m below the tunnel floor. (a) After 30 days of heating (b) After 60 days of heating.*

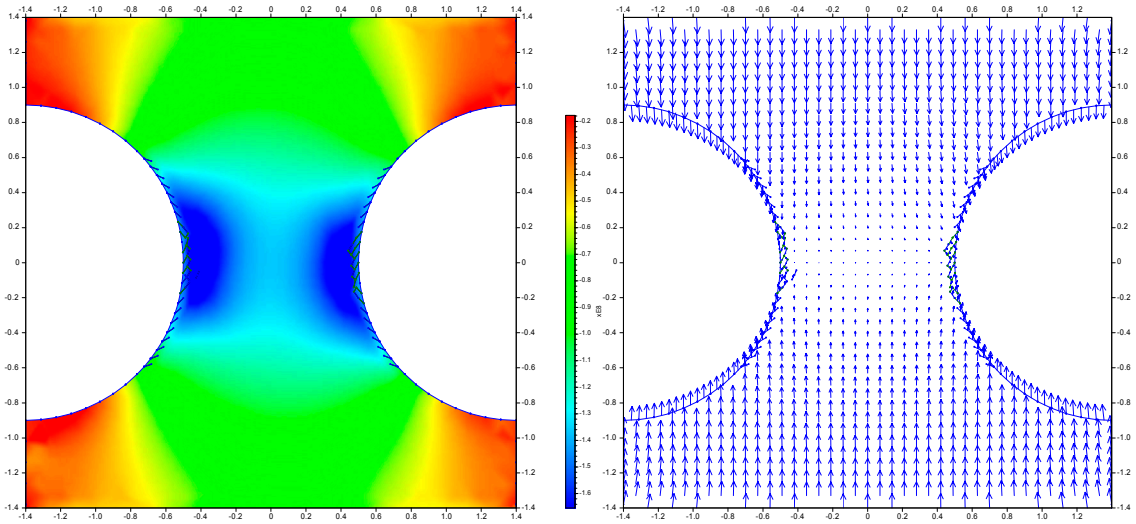

(a) ***(b)***

Figure 4-11. *Stress and displacement distribution after 60 days of heating. (a) Stress contour. (b) Displacement vectors.*

Fracture growth and several elastic fractures are initiated inside pillar region. Stress and displacement fields (Figure 4-11) are similar to those of excavation stage, though their values are slightly increased. Stress release due to fracturing has occurred along the pillar walls, and maximum stress is slightly shifted toward the mid pillar.

- **90 and 120 days of heating**

Fracture initiation and propagation continues with stress increase in a limited area in the pillar, but extent of fractured zone is enlarged along pillar walls from central part (Figure 4-12). Possible spalling is still restricted to a narrow area at the borehole boundary and the pillar core seems to remain intact on section at 1.5 m below the tunnel floor. Stress contour (Figure 4-12 (b)) shows some relaxation along borehole wall due to fracturing, but general trend is maintained from the previous loading step though the value has increased. Displacement vectors near the central wall remain small, which means stable fracture propagation.

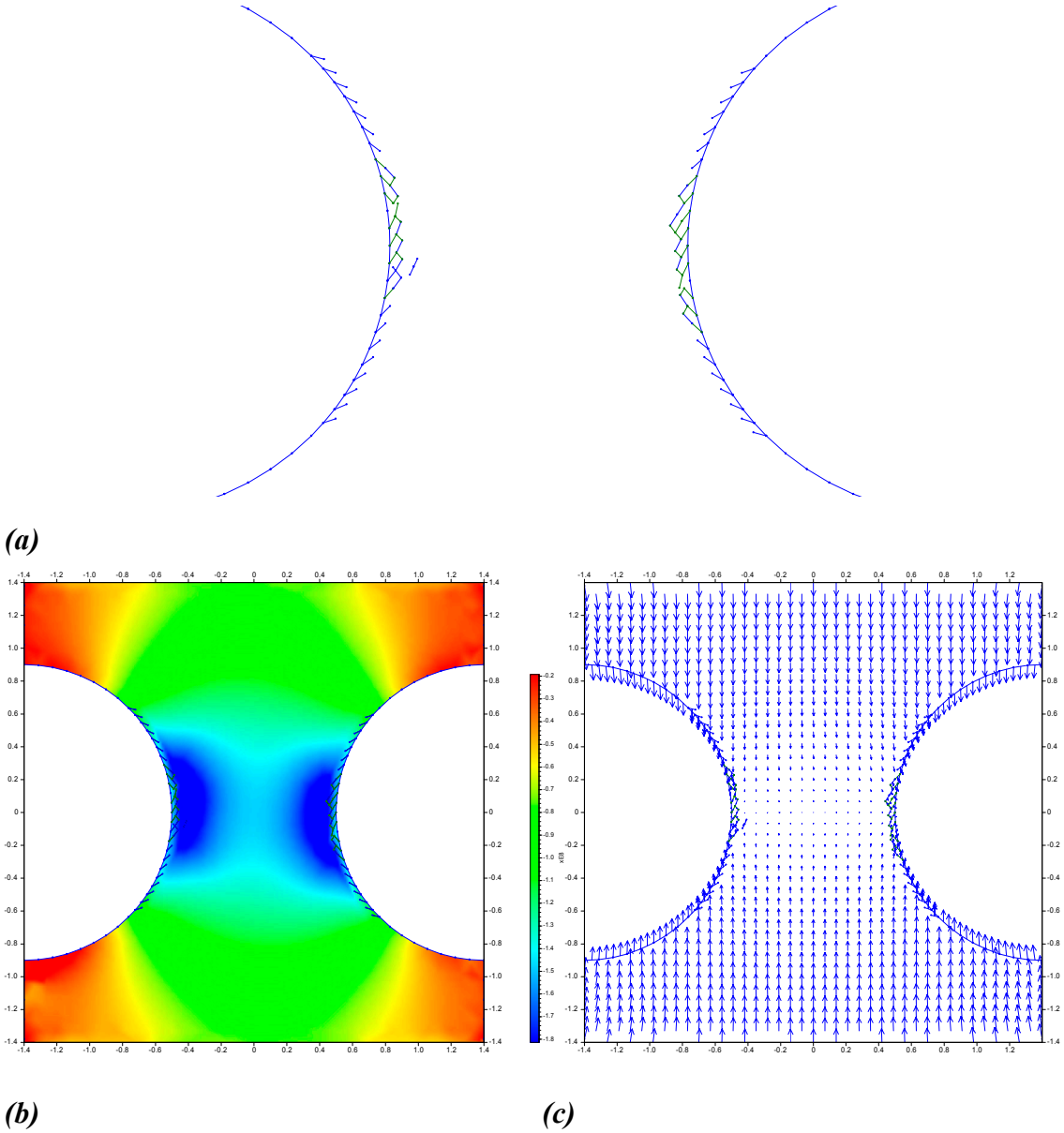

(a)

(b) ***(c)***

Figure 4-12*. Fracture initiation and propagation caused by thermal stresses after 120 days of heating. (a) Fracture pattern. (b) Stress contour. (c) Displacement vectors.*

4.3.2 Section 0.5 m below the tunnel floor

(1) Effect of excavation

The effect presented for the section 0.5 m below tunnel floor is similar to that presented for section 1.5, but some fractures have propagated (Figure 4-13). The maximum induced stress in the pillar boundary after excavation is about 137 MPa. This stress will cause some fracture initiation and propagation at the central part of the borehole boundaries (see Figure 4-13). The area of fracturing is increased in a horizontal plane compared with the 1.5 m section.

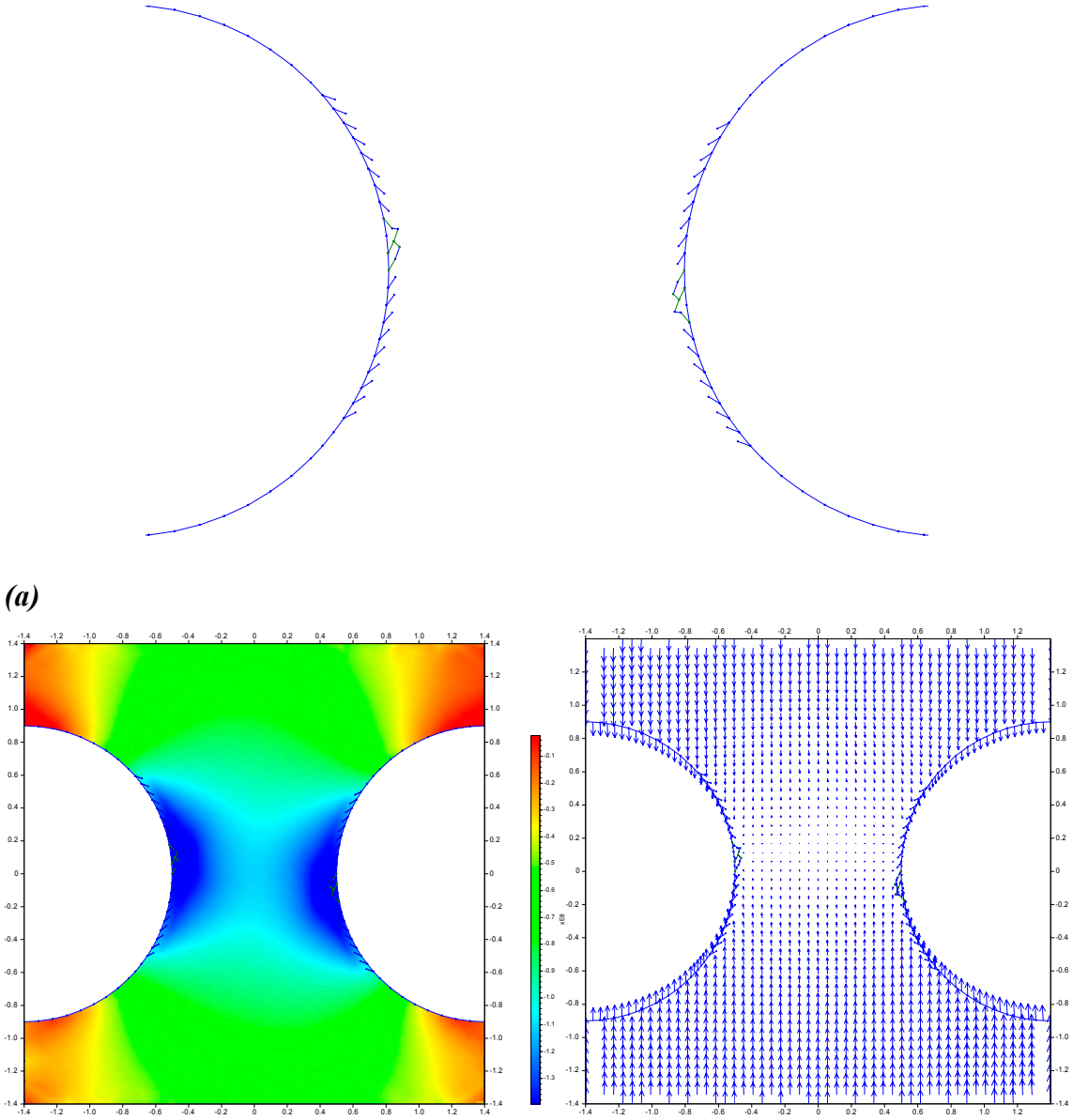

(a)

(b) ***(c)***

Figure 4-13. *Fracture evolution after borehole excavation at 0.5 m below the tunnel floor. (a) Fracture pattern. (b) Stress contour. (c) Displacement vectors.*

(2) Effect of temperature increase

- **30 and 60 days of heating**

Fracture initiation and propagation along central borehole walls occur continuously with stress increase (Figure 4-14 (a)). A major fracture is developed at the left side due to brittle fracturing, but the pillar region remains stable. The pattern of possible spalling from subsequent loading becomes more apparent though pillar remains stable at this stage.

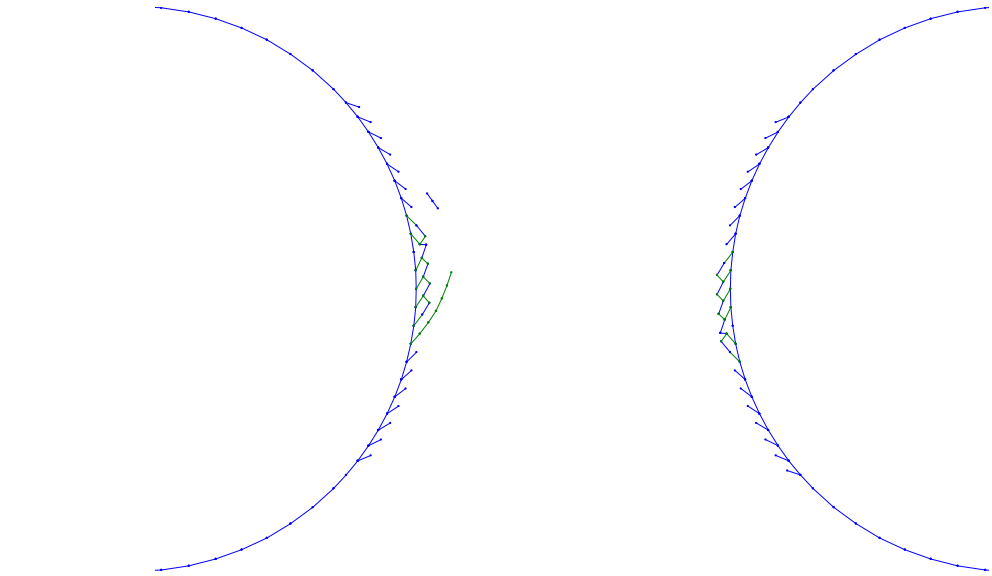

(a)

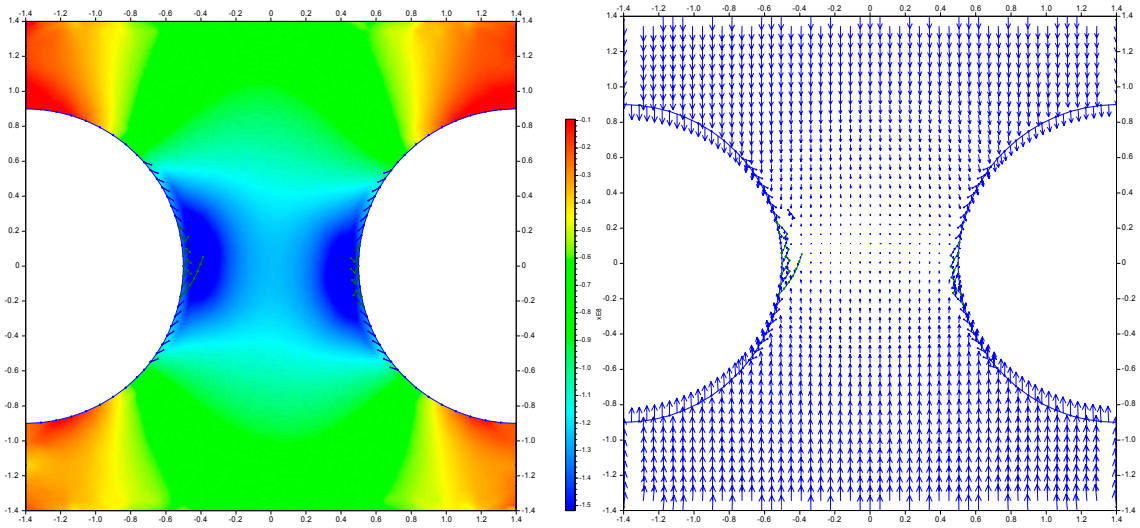

(b) ***(c)***

Figure 4-14*. The evolution of fracturing at the borehole boundary caused by thermal stresses at 1.5 m below the tunnel floor after 30 days of heating. (a) Fracture pattern. (b) Stress contour. (c) Displacement vectors.*

The effect of confining pressure at the right hole becomes apparent at this stress level as shown in Figure 4-14 (a). Compared to left side, fracture growth at the right pillar side seems to be limited. Stress contour (Figure 4-14 (b)) shows similar pattern with the case of 1.5 m section, and high stress concentration is anticipated in the vicinity of the pillar walls. There is no major difference in displacement vectors (Figure 4-14 (c)), suggesting that the pillar region is stable even though some fractures are formed. It is important to note that the amount of fracture displacement is dependent on deformational properties of fresh created fractures.

- **90 and 120 days of heating**

After 90 days of heating two major fractures are propagated deep into the pillar, and several fractures are initiated inside pillar region especially at the left side. The fractures together with major extended fractures can make possible V-shaped shear spalled zone if further loading is applied. The intact area of the pillar has slightly decreased compared to 1.5 m section due to increased fracture initiation inside pillar. Few fractures are propagated in both shear and tensile mode after 120 days of heating (Figure 4-15). In spite of the extensive fracturing at left side of the pillar, overall stability would be maintained after 120 days of heating as it can be expected from stress distribution (Figure 4-16)

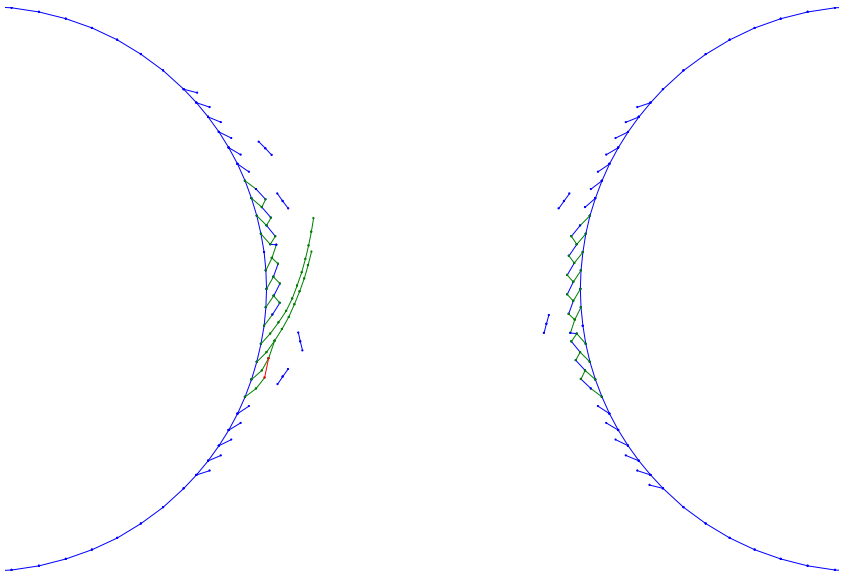

Figure 4-15. *Fractures in the mid pillar at 0.5 m below the tunnel floor after 120 days of heating.*

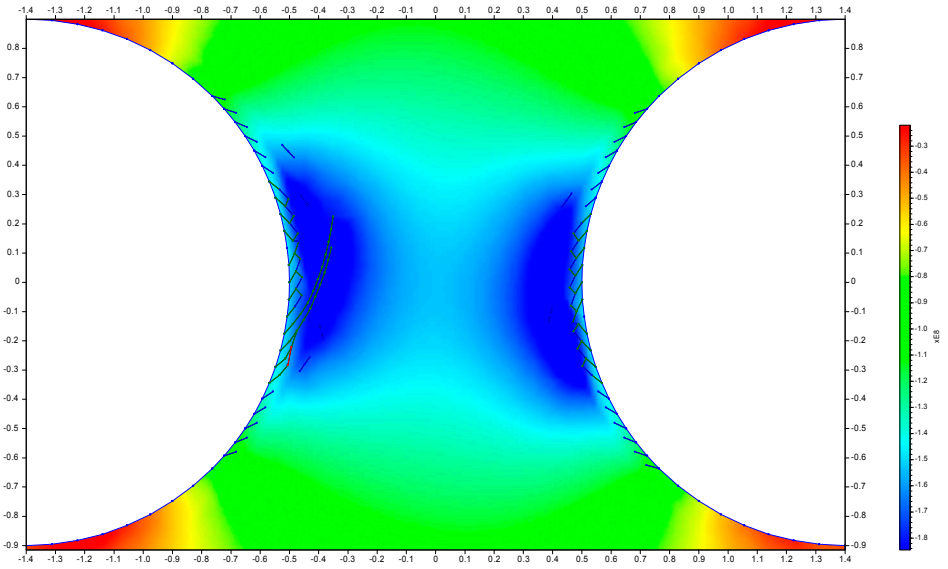

Figure 4-16. *Stress distribution including heating at 0.5 m below the tunnel floor after 120 days of heating.*

Based on the stress distribution (Figure 4-16) from subsequent thermal loading, overall stress level in pillar region is significantly increased compared to the stress state after excavation, and stresses at borehole wall are redistributed due to fracturing.

4.3.3 AE evolution

Figure 4-17 and Figure 4-18 represent the evolution of AE events during fracturing process with the Pillar model for each section, respectively. In the figures, red dots represent the current active AE events. AE events are stepwise modelled and the intensity of AE events is proportional to the degree of fracturing.

Accurate history for AE events is not possible to define here, since the Pillar models only consider thermal loading by discrete increments of equivalent boundary stresses. Here, four heat increments have been used. AE events are usually produced from fracturing after applying incremental loading and before stabilization, therefore only AE evolution during each heating step can be addressed in the Figures. Figure 4-17 (b) and Figure 4-18 (b) show AE evolution just after applying a half increment of 30 days of heating.

Most of the AE events occur in the vicinity of the central pillar walls for both sections. In the 0.5 m section, the propagation of major fractures creates intense AE events after heating.

In the 1.5 m section, AE events at the left borehole are occurred mostly before 30 days of heating, and then AE at the right one become intense after 60 days of heating. Since fracture process is limited in this section, further intense AE events are predicted to occur during 90-120 days of heating at both sides.In the case of 0.5 m section, very intense AE events occur at the central pillar wall after excavation due to fracture propagation. AE events are very active at the left side for all loading stages as inferred from fracturing pattern at this depth.

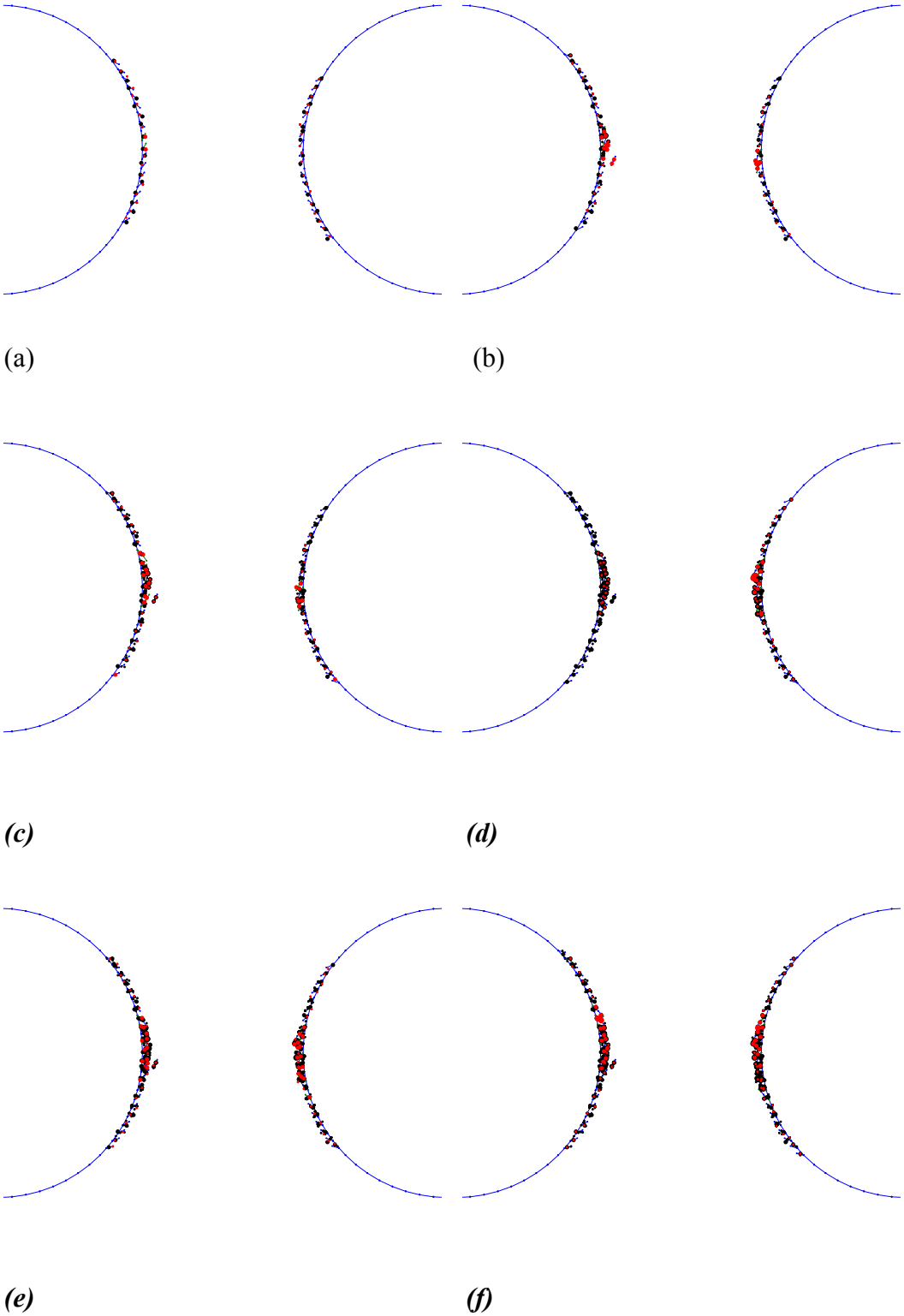

Figure 4-17. *AE evolution of the Pillar model for each loading stage at 1.5 m section below the tunnel floor. (a) After excavation. (b) After the start of heating. (c) After 30 days of heating. (d) During 60 days of heating. (e) During 90 days of heating. (f) During 120 days of heating.*

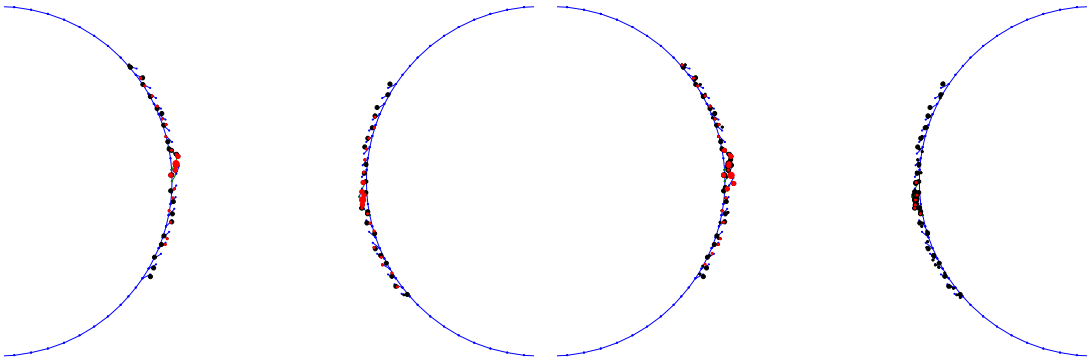

(a) ***(b)***

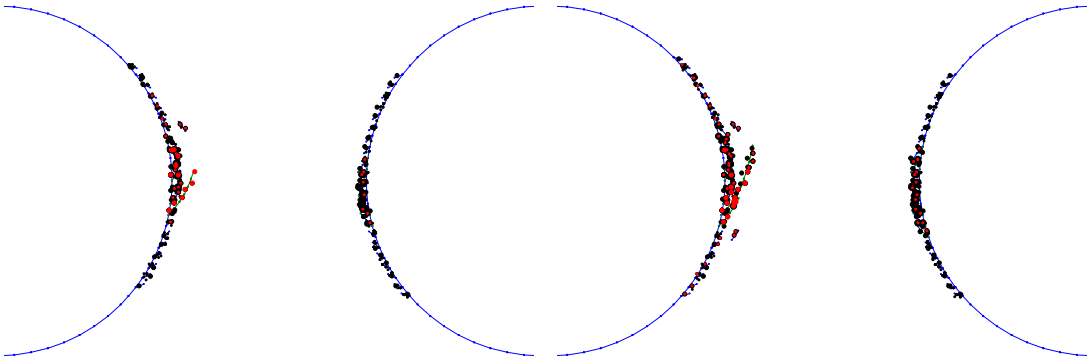

(c) ***(d)***

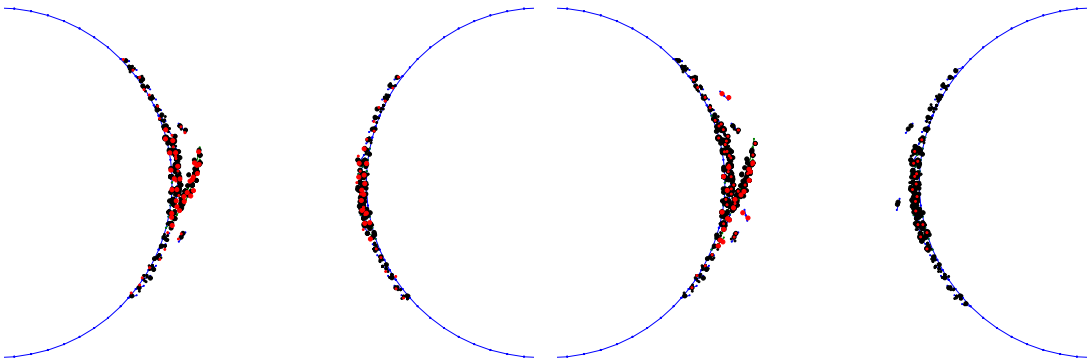

(e) ***(f)***

Figure 4-18. *AE evolution of the Pillar model for each loading stage at 0.5 m section below the tunnel floor. (a) After excavation. (b) After the start of heating. (c) After 30 days of heating. (d) During 60 days of heating. (e) During 90 days of heating. (f) During 120 days of heating.*

4.3.4 Deformation at the pillar boundaries

Displacement along boundaries can be an indicative of the pillar instabilities. Variations of boundary displacement are investigated from the Pillar models in this section. To avoid confusion, notation of angle along the pillars is presented in Figure 4-19. For the left borehole, 0°, 90° and 180° mean bottom, sidewall and top part of the pillar, respectively. For the right borehole, 0°, -90° and -180° are used for corresponding locations as shown in Figure 4-19.

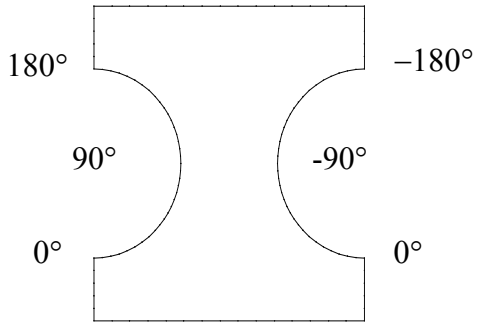

Figure 4-19*. Notation for the location of the pillar boundaries.*

Table 4-1. Total displacement along the pillar boundary for each loading step.

z=1.5m		**Total Displacement (m)**					
Angle(°)	**Location**	**Excavation**	**Hydraulic Pressure**	**30days**	**60days**	**90days**	**120days**
	Left Pillar Wall						
0	Bottom	1.28E-03	1.28E-03	1.50E-03	1.62E-03	1.72E-03	1.80E-03
90	Side	9.72E-05	1.10E-04	1.59E-04	1.90E-04	2.17E-04	2.29E-04
180	Top	1.55E-03	1.55E-03	1.77E-03	1.92E-03	2.03E-03	2.12E-03
	Right Pillar Wall						
0	Bottom	1.52E-03	1.52E-03	1.66E-03	1.84E-03	1.98E-03	2.08E-03
-90	Side	1.07E-04	8.81E-05	1.74E-04	1.20E-04	1.21E-04	1.29E-04
-180	Top	1.24E-03	1.24E-03	1.39E-03	1.57E-03	1.69E-03	1.80E-03
z=0.5m							
	Left Pillar Wall						
0	Bottom	1.53E-03	1.53E-03	1.75E-03	1.87E-03	1.97E-03	2.05E-03
90	Side	1.91E-04	1.98E-04	1.63E-04	1.81E-04	2.00E-04	1.95E-04
180	Top	1.59E-03	1.59E-03	1.81E-03	1.96E-03	2.07E-03	2.17E-03
	Right Pillar Wall						
0	Bottom	1.82E-03	1.82E-03	1.96E-03	2.14E-03	2.27E-03	2.38E-03
-90	Side	1.46E-04	1.32E-04	1.54E-04	1.59E-04	1.56E-04	1.70E-04
-180	Top	1.25E-03	1.25E-03	1.39E-03	1.57E-03	1.69E-03	1.80E-03

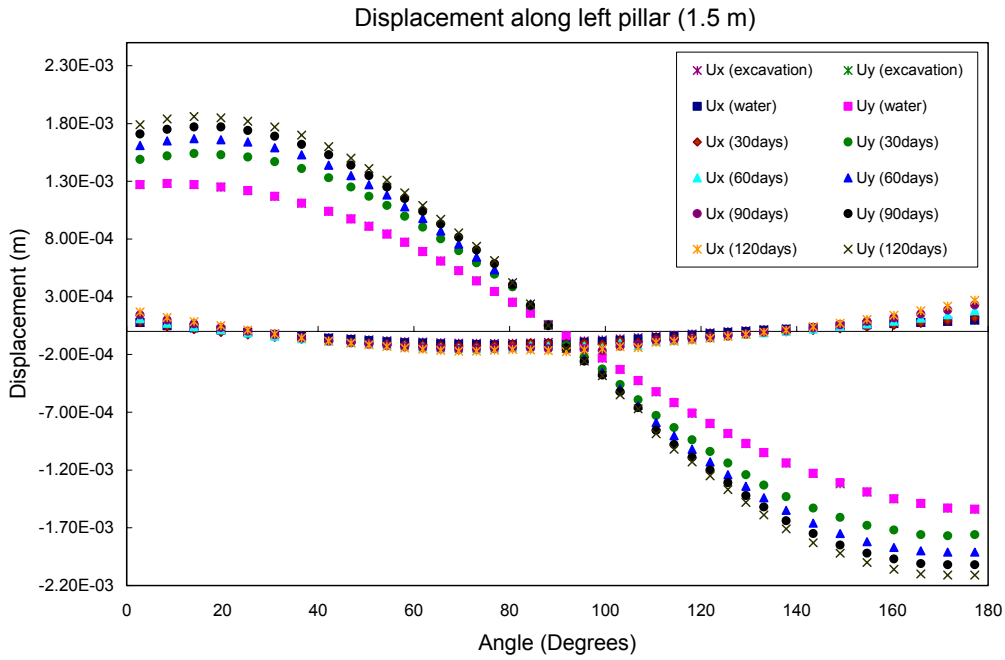

(a)

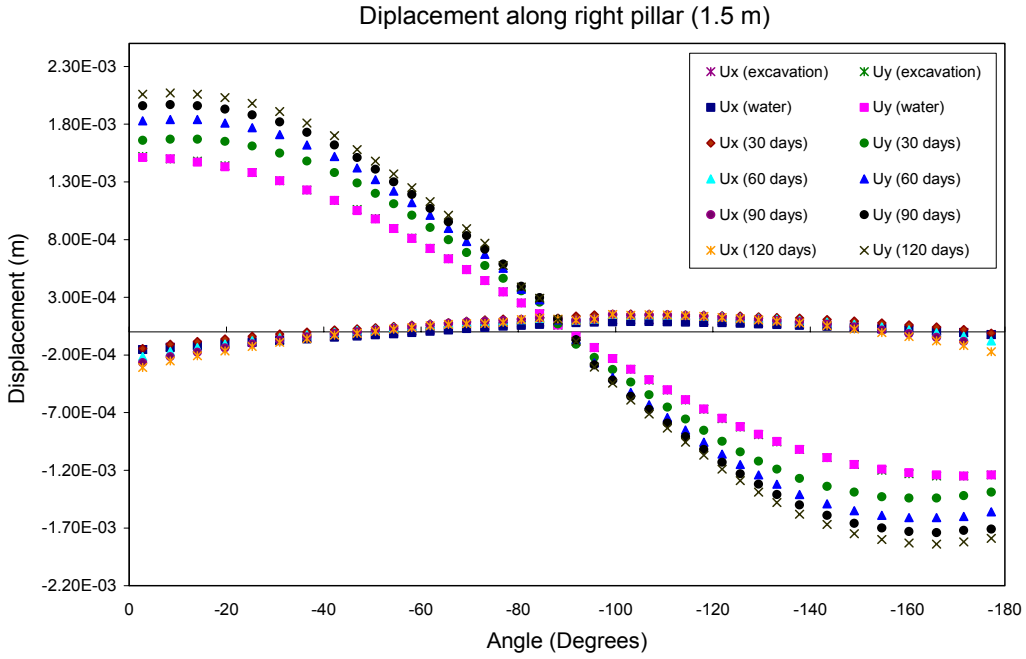

(b)

Figure 4-20. *Displacement along pillar boundaries at 1.5 m section below the tunnel (Ux: x- displacement, Uy: y- displacement). (a) Left borehole wall. (b) Right borehole wall. Ux and Uy for excavation and for confinement (water) overlap in the figures.*

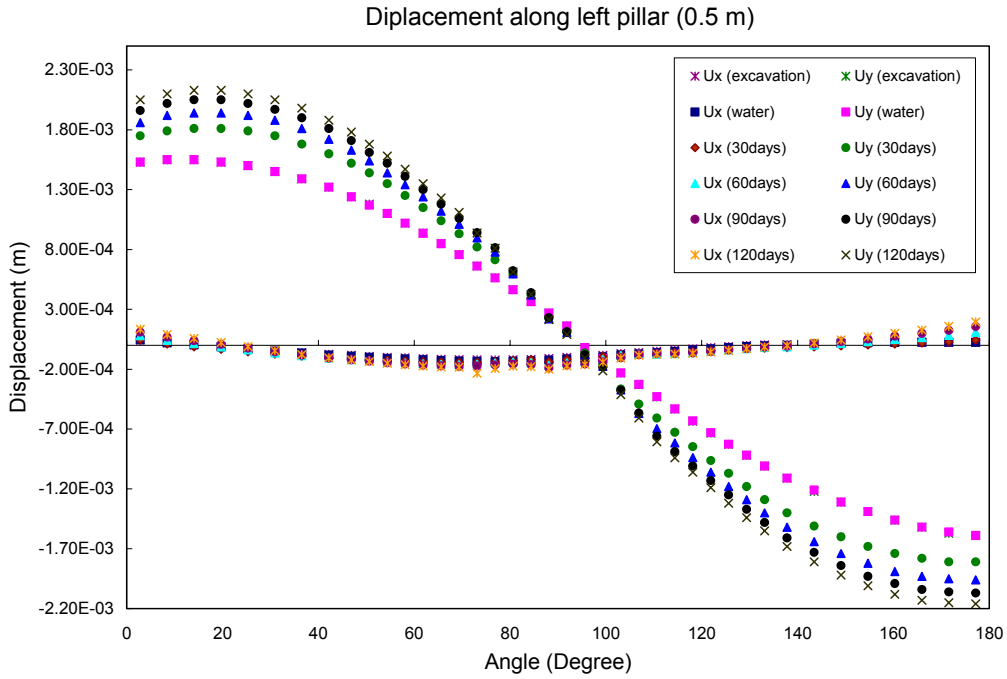

(a)

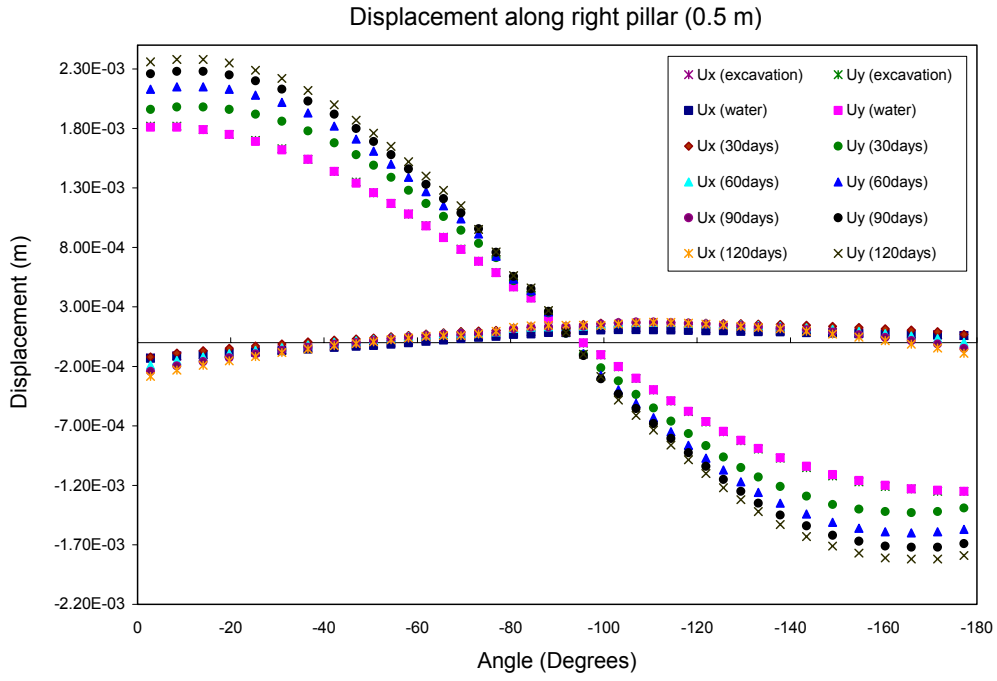

(b)

Figure 4-21*. Displacement along pillar boundaries at 1.5 m section below the tunnel (Ux: x- displacement, Uy: y- displacement). (a) Left borehole wall. (b) Right borehole wall. Ux and Uy for excavation and for confinement (water) overlap in the figures.*

Table 4-1 lists the total displacement at certain points along the pillar from each loading stage. Figure 4-20 and Figure 4-21 show the x- and y- directional displacements along the pillar. Displacements at bottom and top are large due to the major principal stress, and it become very small at the sidewall. Since in-situ stress is non-symmetric, displacements at bottom and top are slightly different. Deformations at all sides are gradually increased according to loading stage even though fracturing has occurred, so it is comparable to elastic deformation. This is mainly because fracture deformability has been restricted to avoid numerical instabilities in the FRACOD as explain in chapter 3.

1 MPa confinement mostly affects the deformation of Ux (not Uy). The effect of the confinement is small and in Figure 4-20 and Figure 4-21 they overlap each others.

Actually, it is difficult to predict how fracturing in the vicinity of the pillar boundaries can influence deformation. The displacement after fracturing is a complex process in real situation. A loose detached block may have 1 mm movement, or 100 mm movement, while the mechanical stability of the remaining part of the rock is not affected.

The current FRACOD cannot consider dynamic effects after failure, which causes difficulties in the accurate prediction of the boundary deformation. Therefore, deformation field cannot be used for a measure of unstable spalling with the current models. More sophisticated treatment with comprehensive constitutive model is required for the accurate prediction of deformation field after post-failure.

4.3.5 Summary of the results

Table 4-2 summarizes the result of Pillar models together with maximum stress and deformation values, and Table 4-3 lists maximum compressive stresses without fracturing by setting artificially high rock strength properties for comparison.

All models show stable behaviour in terms of both stress and deformation though extensive fracture initiation and propagation have occurred along central pillar walls at both depths. Maximum stress level shows comparable results with Golder's result /Fredriksson et al., 2003/. In all cases, stresses after fracturing are smaller than elastic ones due to stress relaxation. After applying hydraulic pressure, only slight maximum stress change is occurred. Critical condition for unstable spalling is not anticipated after 120 days of heating both 0.5 m and 1.5 m sections. According to the modelling results, the amount of loading should be increased to see unstable fracturing process in the whole pillar region.

Table 4-2. Summary of results from Pillar model for each loading step.

		1.5 m	Comments on fracturing	0.5 m	Comments on fracturing
Excavation	M.C* M.T** M.D***	115.9 3.84e-5 1.58	Elastic fracture initiation along pillar walls	141.3 5.27 1.86	Fracture initiation along pillar walls and minor propagation at central pillar
30 days	M.C M.T M.D	152.4 2.86 1.79	Fracture coalescence at central pillar wall	152.5 7.18 2.03	Fracture coalescence, propagation. A creation of major fracture
60 days	M.C M.T M.D	167.8 3.07 1.94	Enlargement of combined fractures at limited area	171.3 8.02 2.21	Enlargement and propagation of fractures
90 days	M.C M.T M.D	177.9 3.27 2.06	Few fracture initiation in the vicinity of the pillar wall	181.5 8.44 2.33	Enlargement and propagation to inside pillar region
120 days	M.C M.T M.D	181.8 3.30 2.16	Few fracture initiation in the vicinity of the pillar wall	185.7 9.80 2.43	Extended fracturing and propagation in the vicinity of the pillar wall

* M.C : Maximum compressive stress (MPa), **M.T: Maximum tensile stress (MPa)
***M.D: Maximum displacement ($\times$e-3m).

Table 4-3. Maximum elastic compressive stresses without fracturing for each loading step.

Section	Excavation	Hydraulic pressure	30 days	60 days	90 days	120 days
1.5 m	122.9	122.4	158.1	171.3	181.5	189.8
0.5 m	137	136.6	171.9	185.8	190.9	198.5

5 Effect of pre-existing fractures and fracture properties

Sensitivity analyses have been performed for both Far-field and Pillar models to investigate the effect of pre-existing fractures and fracture properties on borehole failure.

For the Far-field model, standard case is considered using the following far-field stresses: $\sigma_x = 10\,\text{MPa}$, $\sigma_y = 30\,\text{MPa}$. All other parameters for rock and fracture properties are set to standard parameters as defined in section 3.1.

After reaching a stable fracture model, the applied far-field stress of σ_y is increased to 50 MPa. This loading configuration gives similar maximum stress values at the pillar wall compared to 2D-coupled thermo-mechanical models after 120 days of heating.

5.1 Effect of the pre-existing fracture geometry

5.1.1 Crossing fractures with borehole

Figure 5-1 shows several results in cases of borehole crossing fractures. No fractures are set around right borehole to compare the effect. In all cases, final maximum stress and fracturing are decreased regardless of fracture orientation. Since pre-existing fractures allow additional deformation compared to intact rock, it reduces the stress concentration inside pillar region.

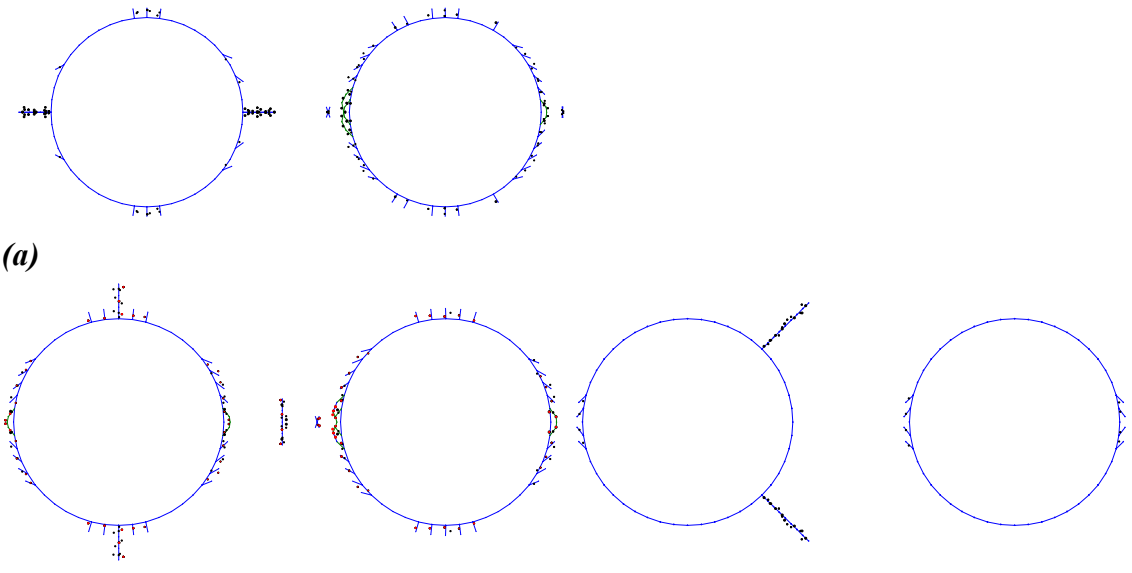

(a)

(b) ***(c)***

Figure 5-1. *Effect of existing fractures crossing the borehole under far-field stresses of σ_x/σ_y= 10 MPa/50 MPa. (a) Fractures perpendicular to major principal stress (b) Fractures parallel to major stress. (c) Inclined (45°) fractures.*

5.1.2 Non-crossing fractures with borehole

Figure 5-2 shows examples of the effect of non-crossing fractures. Because pre-existing fractures redistribute the stress concentration at the borehole wall, the fracturing is predicted to be less compared to the intact case. However, pre-existing fractures may also concentrate the stresses and cause local instability in form of extensive fracture initiation and propagation in the vicinity of fracture tips. The effect depends on the location and orientation of the pre-existing fracture.

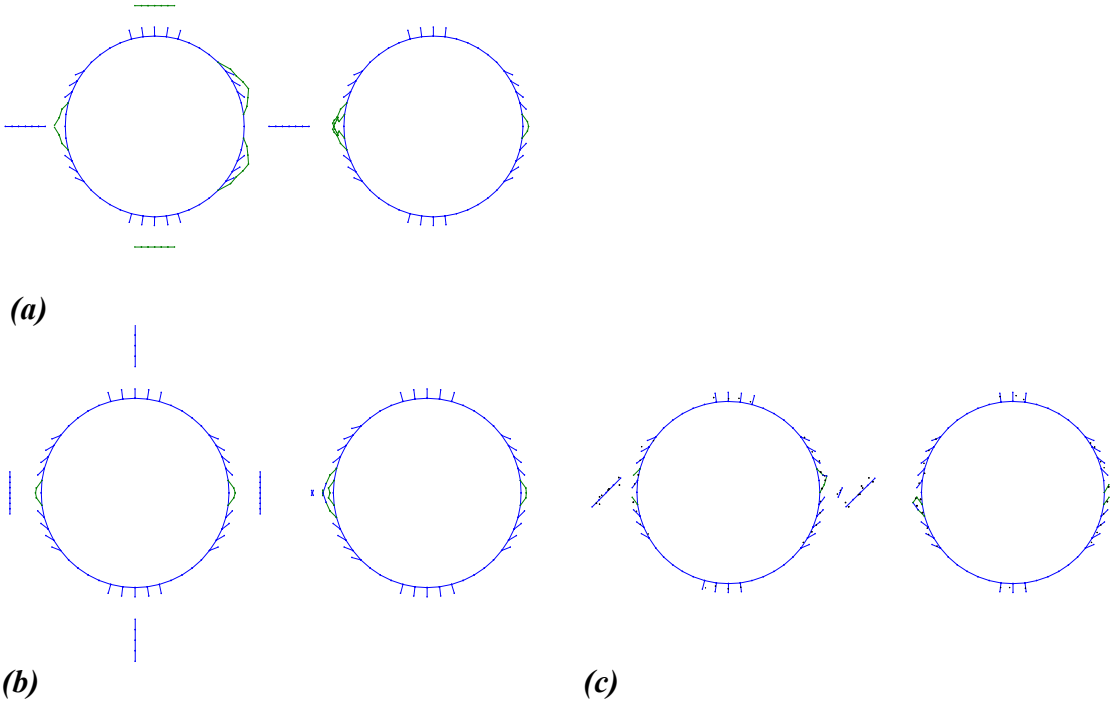

Figure 5-2. *Effect of non-crossing fractures under far-field stresses of σ_x/σ_y =10 MPa/50 MPa. (a) Fractures perpendicular to major principal stress. (b) Fractures parallel to major stress. (c) Inclined (45 °) fractures.*

5.1.3 Effect of large fractures

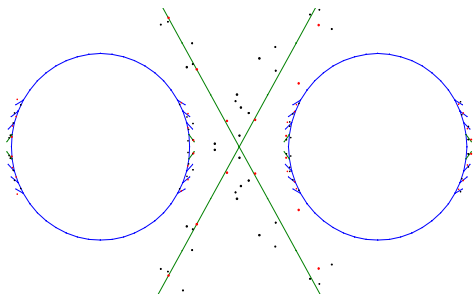

Figure 5-3. *Effect of large inclined fractures under far-field stresses of σ_x/σ_y=10 MPa/50 MPa.*

Several cases are modelled with different orientation of the large fractures. The presence of large fractures, like faults, can significantly reduce the degree of spalling as shown in Figure 5-3.

5.1.4 Pillar model

The excavation stage is considered using the Pillar model. Figure 5-4 shows an example with one inclined fracture in the pillar. Fracture initiation and propagation is more pronounced in the fractured model compared to intact Pillar model. It is noted from Figure 5-4 (b) that high stressed region is shifted toward the tips of the pre-existing fracture in the pillar. However, in many cases the presence of pre-existing fractures will reduce the degree of fracturing as shown in Figure 5-5.

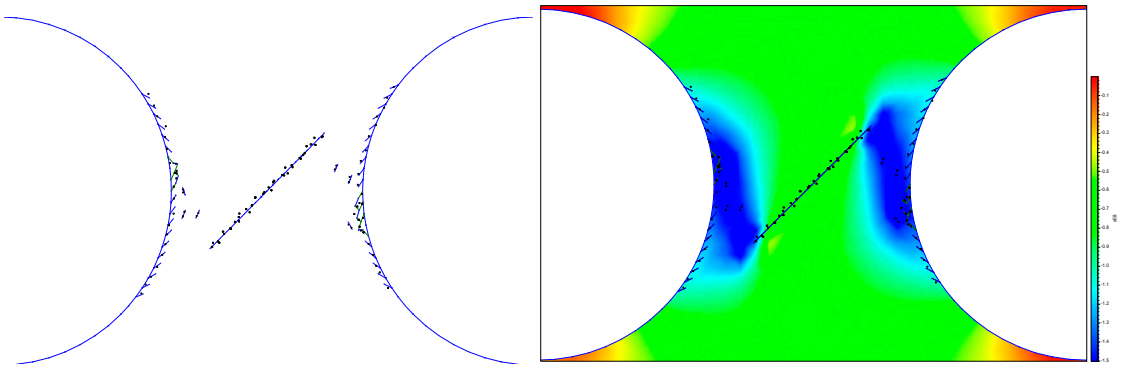

(a) *(b)*

Figure 5-4. *Effect of an inclined fracture from Pillar model at 0.5 m below the tunnel floor after excavation. (a) Fracture pattern. (b) Stress contour.*

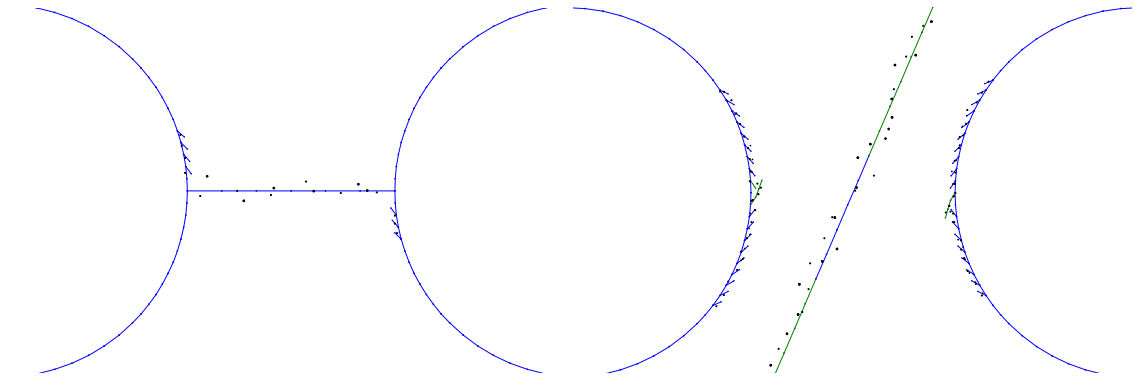

(a) *(b)*

Figure 5-5. *Examples of results from the pillar model at 0.5 m below the tunnel floor after excavation. (a) Effect of horizontal fracture crossing boreholes. (b) Effect of large fracture.*

5.1.5 Summary of the results

Pre-existing fractures can reduce the stress concentration in the critical pillar region because they allow larger deformation compared to intact rock. Fracturing is reduced compared to the intact case due to lower stress level at the borehole wall.

However, instability may occur from extensive fracture initiation and propagation when pre-existing fractures are located inside the pillar in a way that and they cause high stress concentration near their tips.

5.2 Fracture properties

5.2.1 Pre-existing fractures

A sensitivity analysis of fracture parameters have been carried out by FRACOD using simple loading configurations /Rinne, 1999; Rinne, 2000/. The results suggest that the most important factors that control the fracture propagation are:

• Stress ratio ($k=\sigma_3/\sigma_1$) less than 0.3 significantly enhances fracture propagation when the magnitude of the major principal stress is sufficient.

• Orientation of the fractures with respect to the direction of the major principal stress.

• Rock and fracture properties, especially fracture stiffness and fracture toughness.

The effect of fracture stiffness (both K_n and K_s) on fracture propagation depends on the orientation of the fracture. The effect is more pronounced, if the fracture is inclined more than 30° from the major stress. Fracture stiffness might even affect the mode of fracture propagation. The relation between the fracture stiffness and fracture stability was not fully declared in this study /Rinne, 1999/. Calculation seems to be more stable when the value of fracture stiffness is higher than 100 GPa/m.

Generally, increasing the value of fracture toughness (K_{IC} or K_{IIC}) increases the required load for fracture propagation. The effect of K_{IC} or K_{IIC} depends on the loading configuration. Increase of K_{IIC} in bi-axial loading conditions increase the threshold value of fracture propagation, while the effect of K_{IC} is less evident. The effect of K_{IC} is more pronounced in uniaxial loading conditions, when tensile failure will dominate.

With increasing the fracture friction angle the applied load needed for fracture propagation will be increased. The effect is more pronounced for confined loading conditions.

Fractures with high fracture cohesion calls for high far-field stresses to trigger the fracture propagation. The effect of fracture cohesion on the mode of fracture propagation (propagation in tensile or shear mode) seems no to be significant.The elastic properties of intact rock control the displacements and slightly affect the threshold value for fracture propagation. Stiffer material requires higher stress level to trigger fracture propagation.

5.2.2 Newly created fractures

The effect of properties of new created fractures has been preliminary studied. Table 5-1 lists the fracture properties for the sensitivity analysis. All other parameters for rock and fracture properties are set to standard parameters as defined in section 3.1.

Table 5-1. Fracture properties for sensitivity analysis.

Parameters	Standard case	Variable case
Cohesion of newly created fractures (MPa)	30	15, 45
Friction angle of newly created fractures (°)	50	40, 60
K_s / K_n newly created fractures (GPa/m)	320 / 4643	1, 10 and 100 times

The following figures show typical results from sensitivity analysis. All figures are taken from results under far-field stresses of σ_x/σ_y=10 MPa/50 MPa.

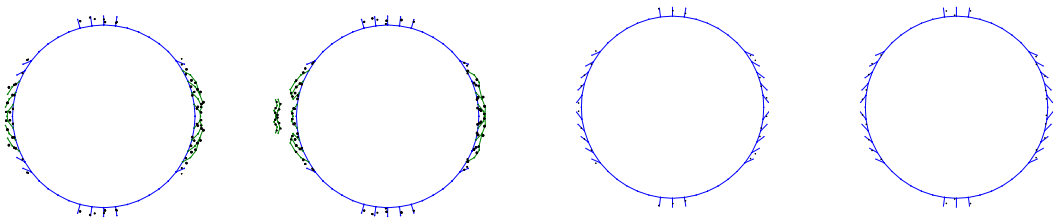

(a) ***(b)***

Figure 5-6. *Borehole behaviour with different cohesion (C) of newly created fractures. (a) C=15 MPa. (b) C=45 MPa.*

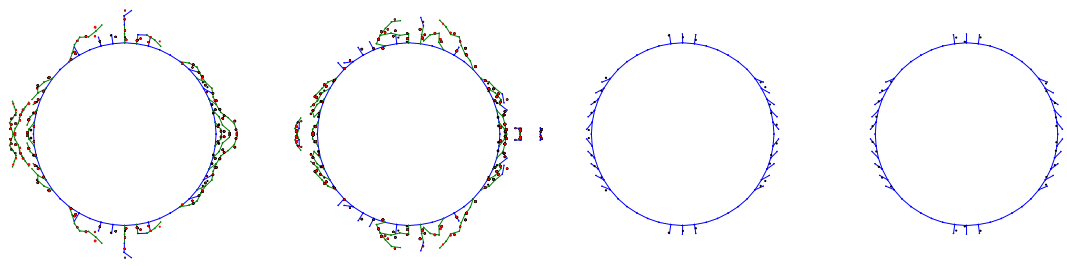

(a) ***(b)***

Figure 5-7. *Borehole behaviour with different friction angle of newly created fractures. (a)* $\phi = 40°$. *(b)* $\phi = 60°$.

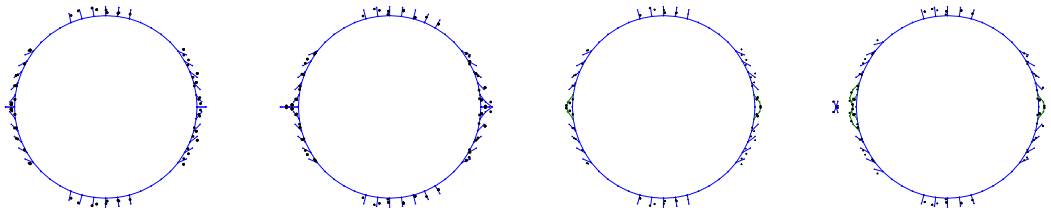

(a) ***(b)***

Figure 5-8. *Borehole behaviour with different K_n of newly created fractures. (a) K_n=65.5 GPa/m. (b) K_n=6550 GPa/m.*

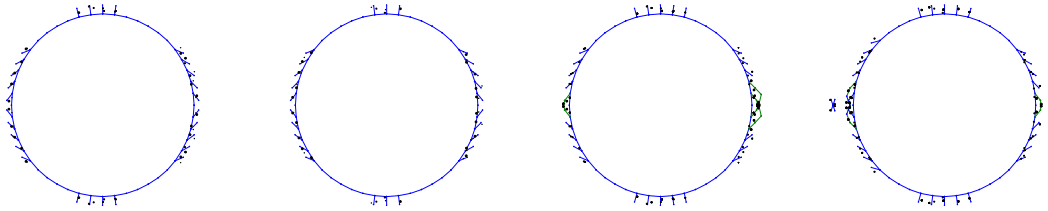

(a) ***(b)***

Figure 5-9. *Borehole behaviour with different K_s of newly created fractures. (a) K_s=35.5 GPa/m. (b) K_s=3550 GPa/m.*

As shown in figures, properties of newly created fractures may have a significant effect on spalling. Fracture cohesion and friction angle control the condition for further propagation of fractures, and totally different fracture pattern may be resulted, as shown in Figure 5-6 and Figure 5-7.

5.2.3 Summary of the results

All fracture parameters influence fracturing process and most of the parameters are sensitive to the given stress conditions. Therefore, general conclusions of fracture parameter sensitivity on rock fracturing cannot be given with a specific fracture model and loading configuration.

Fracture stiffness controls strongly the local stress redistribution in the vicinity of the fracture as well as deformation, especially at the fracture tip. A fracture with low stiffness gives large deformation and the fracture response like a hole.

There is only sparsely data available about newly created fracture properties. Table 5-2 summarizes the basic sensitivity with the choice of properties of freshly created fractures.

Table 5-2. Summary on the effect of properties of newly created fractures.

Properties	Low values	High values
Cohesion	High fracturing	Less fracturing
Friction angle	High fracturing	Less fracturing
K_n	Less fracturing	High fracturing
K_s	Less fracturing	High fracturing

6 Discussion on fracturing process

In this chapter, basic failure and spalling mechanism in brittle rock is briefly reviewed. With examples it is shown how FRACOD models the failure mechanism. Finally, the difficulties and uncertainties in prediction of the spalling process in rock are discussed.

6.1 Spalling and failure mechanism in boreholes

According to a number of previous work on borehole breakouts and pillar stability, failure of borehole wall is often of two different modes governed by either tensile or shear fracturing /Vardoulakis et al., 1988; Guenott, 1989; Martin, 2001/. Figure 6-1 shows typical examples of failure pattern by two different mechanisms in macro scale. Shear fractures can be induced in the direction of maximum shear stresses, and tensile fractures can arise in the direction of major stresses when tensile stress exceeds tensile strength. The spalling and failure of rock start from crack initiation and propagation process in micro-mechanical scale. Usually axial splitting is believed to be main failure mechanism in brittle intact rocks. The axial splitting can arise at micro-mechanical scale from existing micro fractures or flaws by wing crack propagation in the direction of major stresses (Figure 6-2). Microscale cracks coalescence with other cracks and create shear fractures in macroscale. The shear fractures are oriented in the maximum shear direction (Figure 6-2(c)).

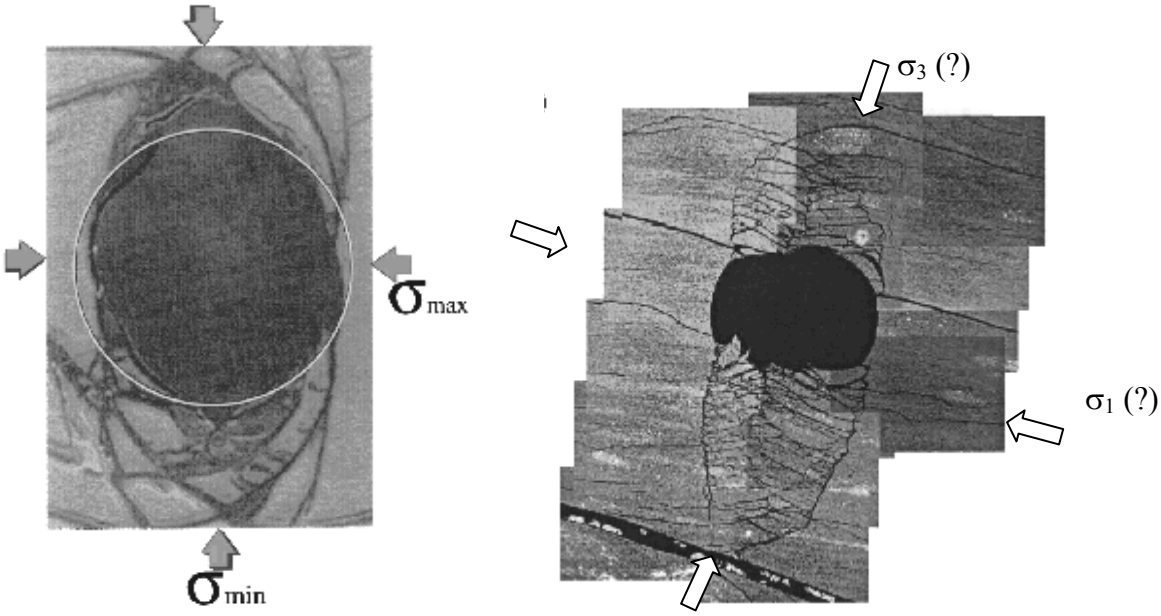

Figure 6-1. *Typical borehole breakouts by two main mechanisms. (a) By shear fracturing /After Syarifuddin and Busono, 1999/. (b) By tensile fracturing /After Germanovich and Dyskin, 2000/.*

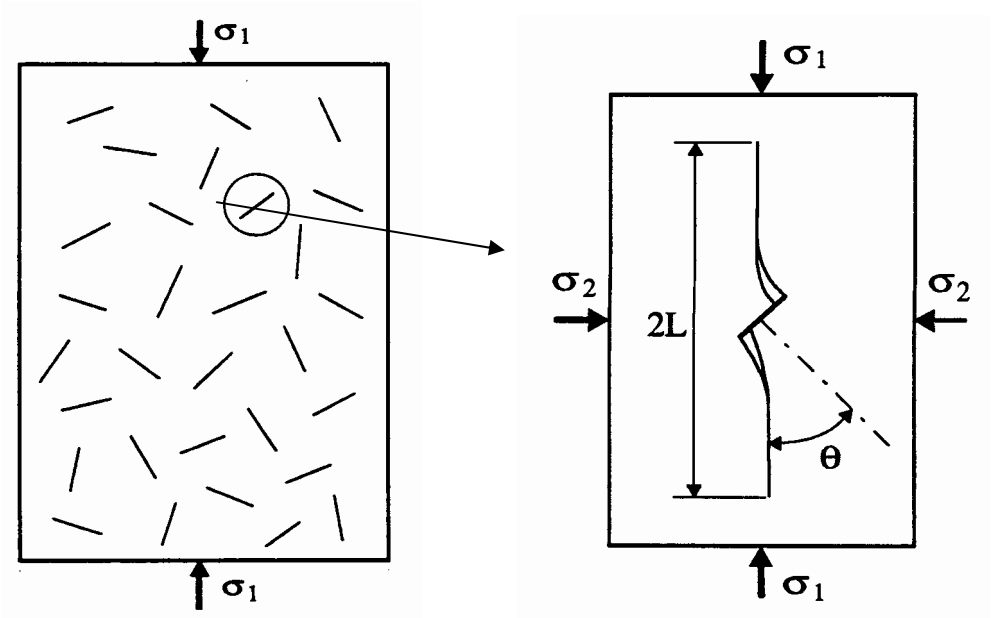

(a) *(b)*

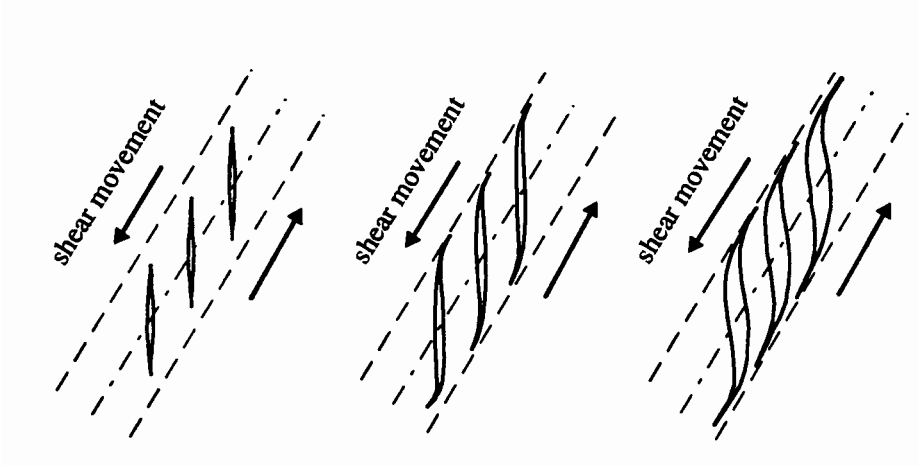

(c)

Figure 6-2. *Fracture mechanism at micro-mechanical scale. (a) Random fracture distribution. at specimen size (b) Wing crack model. (c) Development of shear band by extension of s-shaped fractures /After Li, 1993/.*

The shear fracturing can be dominated in most triaxial conditions even though they may be formed by axial splitting in micro scale. Tensile failure in macroscale can be developed in certain condition like extremely high stress ratio with interaction of pre-existing fractures at the region where tensile stress is dominated, but this mechanism acts in combined manner during complex fracturing process in most cases.

Spalling is a result of two modes of failure, especially in brittle rocks. Usually it can be identified by separation of individual blocks. Tensile fractures may form slabbed structures and shear fractures may create V-notched failure surfaces as shown in Figure 6-1.

6.2 Fracture mechanism in FRACOD

Fractured region stability of boreholes by shear and tensile fractures usually can be estimated by a conventional strength criteria /Martin and Maybee, 2000/, or continuum modelling with sophisticated non-linear constitutive law due to fracturing /Hajiabdolmajid et al., 2002/**.** These types of modelling would be adequate for general assessment of failure in the borehole, but they do not give on idea on detailed stepwise fracturing process by individual fractures.

The two modes of failure mechanisms can be combined in in-situ condition, and FRACOD can consider both shear and tensile fractures by mixed mode fracture criterion, called modified G criterion /Shen and Stephansson, 1993/. In FRACOD micro-mechanical fracturing process is incorporated to the macroscale fracturing based on fracture mechanism implemented with DDM (Displacement Discontinuity Method). More detailed description on implementation process is found in Part II and /Shen, 2002/.

Three examples are shown below to explain how FRACOD models the failure process.Figure 6-3shows the fracturing pattern from numerical tests with APSE parameters. Under uniaxial loading of 120 MPa, a number of open fractures due to tensile fracturing are induced (red line at the Figure 6-3 (a)) in the direction of major principal stresses. However fractures under triaxial loading with confining pressure of 10 MPa and 180 MPa of axial stress are caused by shear failure in the direction of maximum shear stress. It can be seen that fracturing patterns for different stress conditions are reasonably modelled with FRACOD.

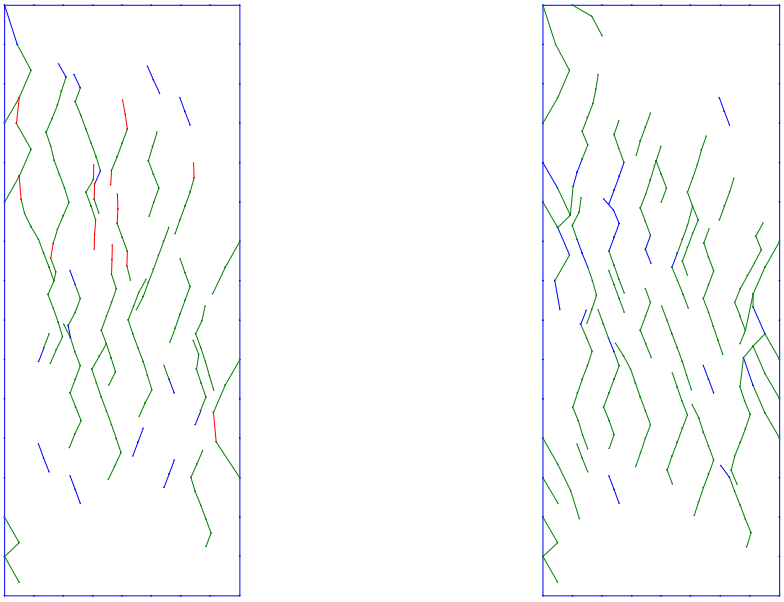

(a) ***(b)***

Figure 6-3. *Fracturing pattern from numerical simulation of laboratory tests with APSE parameters (blue line: fracture in elastic state, red line: open fracture, green line: slipping fracture). (a) Uniaxial tests with axial stress of 120 MPa. (b) Triaxial tests with 10 MPa of confining pressure and with 180 MPa of axial stress.*

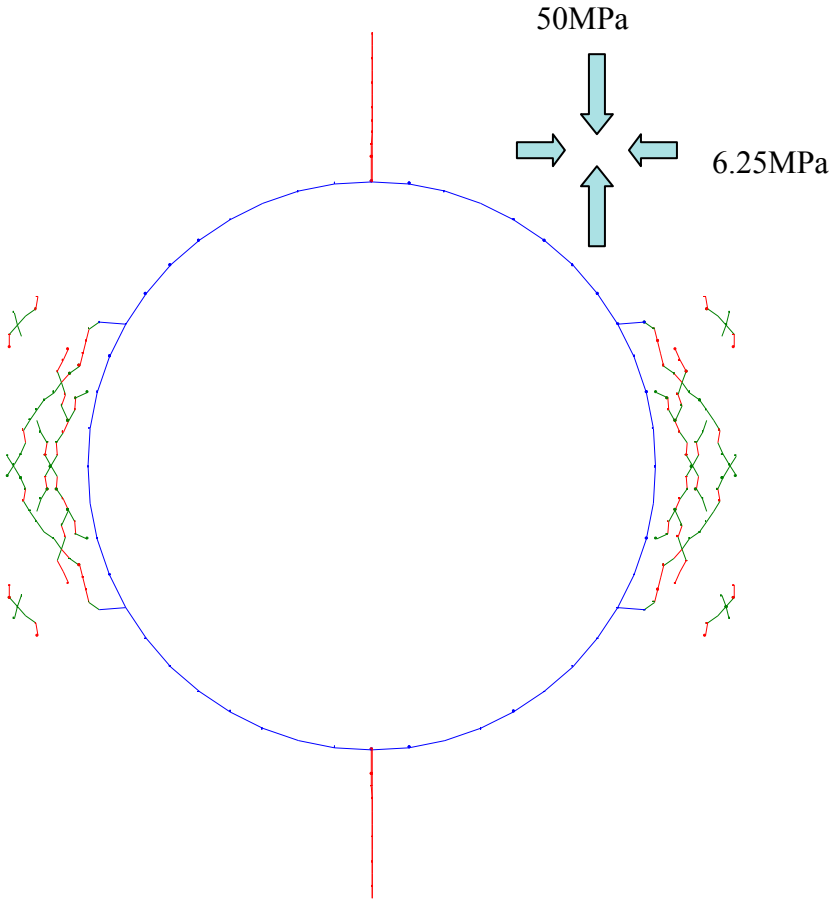

Figure 6-4. *Fracture pattern by two different mechanisms in a borehole model (blue line: fracture in elastic state, red line: open fracture, green line: slipping fracture).*

Figure 6-5 shows the fracture pattern from one borehole model under far-field stresses of σ_x=6.5 and σ_y=50 MPa. Major open fractures are created at the boundary areas which are perpendicular to the major far-field stress, due to tensile fracturing mechanism. Extensive fracturing at the sidewalls is a result of both tensile and shear fracturing. Since stress ratio (σ_x/σ_y) is very small, initiated fractures from shear mechanism turn their direction to major principal stress by tensile fracturing. This kind of fracturing is rare in real underground condition because of the extremely small stress ratio.

Figure 6-5 shows several typical fracturing patterns in the far-field two-borehole model for the APSE modelling. Extreme conditions for both solely tensile and shear fractures are set by changing properties of intact rock. In most cases, real fracturing process would be similar to the behaviour in Figure 6-5 (c). Along the sidewalls both pillar and boreholes, V-shaped notch type shear fractured zone can be developed and slabbing of the “roof” and “floor” can be anticipated for the extreme loading condition. However, in real APSE configuration, increment of loading will be achieved by heating in the vicinity of the pillar region, so fracturing will be limited in the pillar area unlike the results from far-field model.

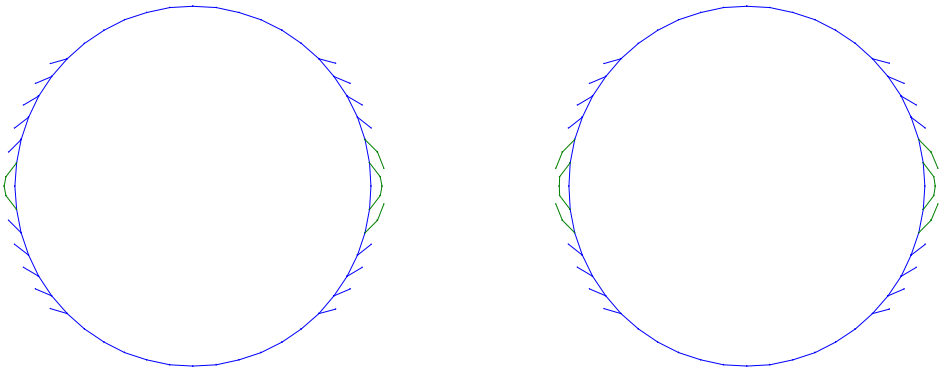

(a)

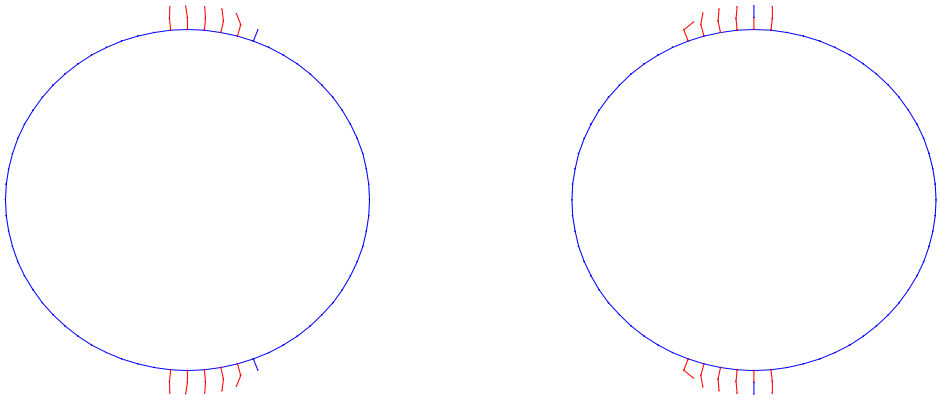

(b)

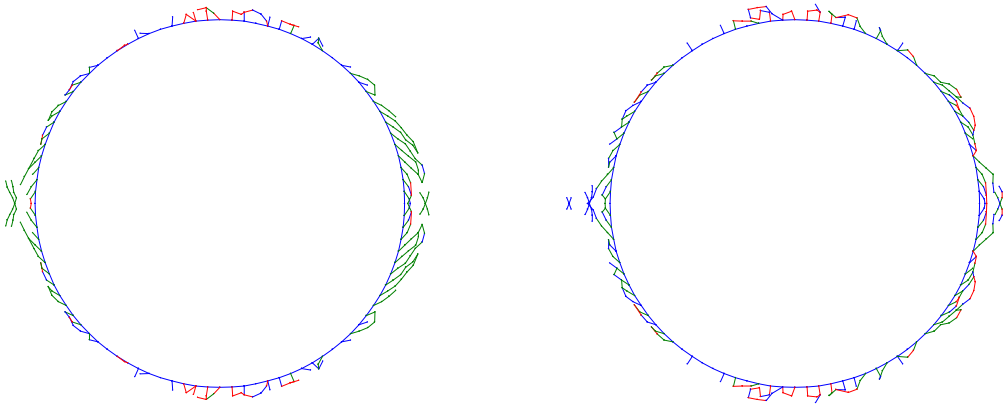

(c)

Figure 6-5. *Fracturing pattern by two different mechanisms in two borehole models. (a) Shear fractures under σ_x=15 and σ_y=45 MPa. (b) Tensile fractures under σ_x=0 and σ_y=30 MPa.. (c) Combined fractures under σ_x=20 and σ_y=60 MPa.*

6.3 Involved uncertainties for prediction

Most of rock mechanics predictions involve uncertainties and so is the case also with spalling. It is difficult to predict exactly when the spalling occurs and how far the spalling will extend in the rock mass. Following are listed some important uncertainties related to both modelled conditions and spalling phenomenon itself.

(1) Uncertainties related with modelled conditions:
- ✓ In-situ stress condition
- ✓ Isotropy and homogeneity of rocks
- ✓ Effect of pre-existing fractures
- ✓ Intact rock and fracture parameters
- ✓ Disturbance of stress field during the experiments due to instrumentation

(2) Uncertainties related with spalling phenomenon:
- ✓ Exact definition of spalling
- ✓ Post-failure behaviour after fracturing
- ✓ Amount of damage of intact rock

We have already shown from sensitivity analysis that properties of intact rock and fresh created fractures can affect dramatically the degree of spalling. Therefore, the degree of uncertainties should be properly considered when the modelling results are evaluated.

Difficulties may arise if spalling is defined only as visual failure or loosening of rock. If energy from fracturing is dissipated in stable manner, the pillar may remain stable, and no spalling would be observed at the wall surface.

FRACOD can simulate fracturing processes explicitly, but modelling of the post-failure behaviour is limited. Numerical instabilities occur when large displacement takes place, for example when a number of detached rock blocks are totally separated from the host. Some spalled regions in models, as shown in Figure6-6, do not demonstrate a total break up. However, in reality this region may loosen and drop.

It was found from several models that large fracture propagation of certain few fractures might occur as shown in Figure 6-7. A comprehensive explanation for this phenomenon was not found. It is noted that these large separate fractures were more pronounced in the Pillar models compared to the Far-field models. The slightly unsymmetrical stress distribution in the Pillar model might concentrate the stresses in such way that it favours certain fractures to grow. The model accuracy seems to have an effect on these individual fractures. The loading rate affects the fracture pattern and slow increase of stress seems to favour large separately propagating fractures. Even if the reason of these fractures remains unclear, the pattern reflects the real behaviour properly. The stresses might be assembled and lead to extensive propagation of one or few fractures instead of ending to a symmetrical fracture pattern.

Figure 6-6. *An example of spalled pattern from the FRACOD Pillar model.*

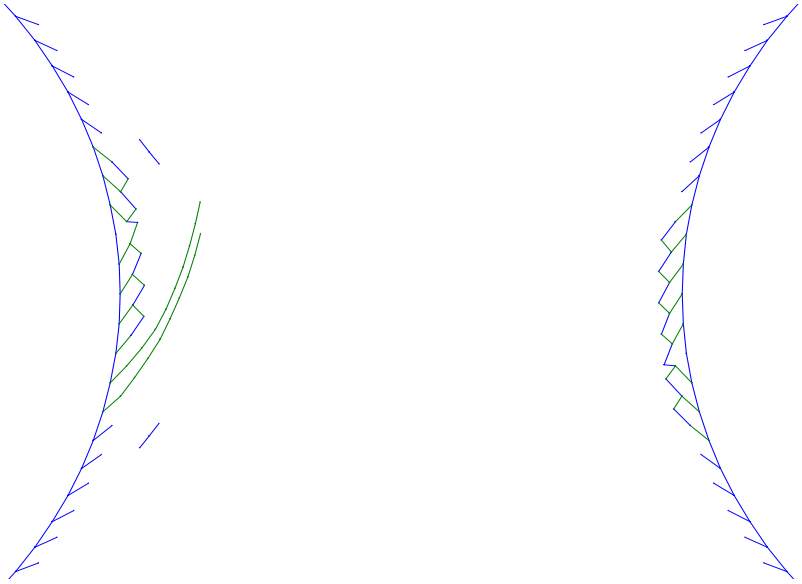

Figure 6-7. *An example of forming large major fractures (recapped from the Pillar model at 0.5 m below the tunnel floor).*

7 Concluding remarks

FRACOD has been updated and successfully used in modelling varying loading stages of the experiment. The following conclusions are based on preliminary field-data:

(1) Far-field model

- Calculations suggest that the planned loading geometry will induce stresses that are close to the limit for fracture initiation with given material properties. Minor fracture initiation may take place in the vicinity of the boreholes before heating.
- Stress conditions leading to spalling will be reached by heating the pillar according to the plan.
- The core of the pillar remains intact in stress conditions corresponding to 120 days of heating.

(2) Pillar model

- Excavation induced stresses will cause some fracture initiation and propagation in the pillar at the central borehole boundary.
- Heating induces minor spalling at central pillar wall for both 0.5 m and 1.5 m section below the tunnel floor, but the area of spalling seems to be limited.
- Calculations suggest that 120 days of heating may lead to extension of major fractures at 0.5 m section, but pillar will remain stable. 1.5 m section seems to be stable after 120 days of heating except minor spalling at central pillar wall.
- Small disturbances in the stress field, for example caused by unsymmetrical heat flow, might affect the fracture pattern and lead to instable fracture propagation. In some models individual fractures extend outside the area of spalling. However, these fractures were not found to propagate unlimited into the pillar.
- Confining pressure of 1 MPa at the right borehole slightly decrease the maximum stresses of the confined borehole wall, but the effect seems to be restricted. The stabilizing effect is more pronounced in the Pillar model at 0.5 m section, where to some extent higher stress level is expected.
- A number of uncertainties in the models exist as explained in chapter 6. There are also limitations in describing the deformation field by current FRACOD models. Further development would be needed for more accurate results.

(3) Pre-existing fractures

- The presence of pre-existing fractures may severely affect the pillar stability. Fractures crossing the boreholes will dissipate the stress concentration and consequently reduce the degree of spalling. Such behaviour is significant especially for large fractures like fault. Thus, any kind of large fractures near the test site should be avoided to assess spalling characteristics properly.
- Pre-existing fractures disturb the stress distribution and may locally cause extensive fracture initiation and propagation near the fracture tip. The effect depends on location, size, orientation and properties of the fracture.

(4) Fracture properties

- Fracture properties, of both pre-existing and new fractures, seem to have a strong effect on the fracturing process.
- Most of the fracture parameters are sensitive for the actual loading configuration. For example, the effect of K_{IC} is more pronounced in uniaxial loading than in confined loading, because tensile failure will dominate under uniaxial loading conditions. Therefore, conclusions of fracture parameter sensitivity on rock failure cannot be given without a site specific fracture pattern and loading configuration.
- Properties of newly created fractures are found to be very important parameters controlling the degree of spalling. Many uncertainties still exist on these properties. Additional study on fracture stiffness and the fracture dilation angle of new fractures is needed to set proper properties for the next phase of modelling.

8 References

Andersson C, 2003. Feasibility study. Äspö Pillar Stability Experiment. International Progress Report, IPR-03-01. Swedish Nuclear Fuel and Waste Management Company, Stockholm.

Bandis, SC, Lumsden, AC, Barton NR, 1983. Fundamentals of Rock Joint Deformation. Int. J. Rock Mech. Sci. & Geomech. Abstr. 20:249-268.

Barton, NR, 1986. Deformation Phenomena in Jointed Rock. Geotechnique. 36:147-167.

Barton, NR, 2002. Personal Communication.

Fredriksson A, Staub I, Janson T, 2003. Design of heaters and preliminary results from coupled 2D thermo-mechanical modelling. Äspö Pillar Stability Experiment. International Progress Report, IPR-03-03. Swedish Nuclear Fuel and Waste Management Company, Stockholm.

Germanovich, LN, Dyskin AV, 2000. Fracture mechanisms and instability of openings in compression. Int. J. Rock Mech. Min. Sci. 37:263-284.

Guenot, A, 1989. Borehole breakouts and stress fields, Int. J. Rock Mech. Min. Sci. & Geomech. Abstr. 26:185-195.

Hajiabdolmajid V, Kaiser PK, Martin CD, 2002. Modelling brittle failure of rock. Int. J. Rock Mech. Min. Sci. 39:731-741.

Staub I, Janson T, Fredriksson A, 2003. Geology and properties of the rock mass around the experiment volume. Äspö Pillar Stability Experiment. International Progress Report, IPR-03-02. Swedish Nuclear Fuel and Waste Management Company, Stockholm.

Klee G, Rummel F, Weber U, 2001. Rock Stress Measurements by means of hydraulic fracturing in borehole KOV01. SKB, Oskarshamn, Sweden.

Lanaro F, 2001. Geometry, mechanics and transmissivity of rock fractures. Doctoral thesis, Division of Engineering Geology, Department of Civil and Environmental Engineering, Royal Institute of Technology, Stockholm, Sweden.

Li C, 1993. Deformation and Failure of Brittle Rocks under Compression. Doctoral Thesis. Luleå University of Technology, Sweden. 1993:118D, ISSN 0348-8373.

Martin CD, 2001. Pillar design for a nuclear waste repository in hard rocks, Rock Mechanics –Challenge for Society, Särkkä & Eloranta (eds), proceeding of EUROCK 2001, AA Balkema, pp 763-768.

Martin CD, Maybee WG, 2000. The strength of hard rock pillars. Int. J. Rock. Mech. Min. Sci., 37(8):1239-1246.

Nordlund S, Li C, Carlsson B, 1999. Laboratory Tests for Determining the Mechanical Properties of the Diorite in Äspö HRL. Division of Rock Mechanics, Luleå University of Technology, Sweden.

Olsson R, 1998. Mechanical and Hydromechanical behaviour of hard rock joints. A laboratory study. Dr Thesis. Department of Geotechnical Engineering, Chalmers University of Technology, Sweden, Göteborg.

Rinne M, 1999. BEMF-Code Testing. Mixed mode fracture propagation in the vicinity of a circular opening in crystalline bedrock. Draft report 99-12-06. Swedish Nuclear Fuel and Waste Management Company, Stockholm.

Rinne M, 2000. Propagation of rock fractures in the vicinity of a canister hole for spent nuclear fuel. Licentiate Thesis. Royal Institute of Technology, Engineering Geology. Stockholm, Sweden.

Rao Q, 1999. Pure shear fracture of brittle rock. A theoretical and laboratory study. Luleå University of technology. Doctoral thesis. Sweden.

Shen B, 2002. FRACOD Version 1.1, User's manual. Fracom Ltd.

Shen B, Stephansson O, 1993. Modification of the G-criterion of crack propagation in compression. Int. J. of Engineering Fracture Mechanics. 47(2): 177-189.

Staub I, Fredriksson A, Outters N, 2002. Strategy for a Rock Mechanics Site Descriptive Model – Development and testing of the theoretical approach. SKB R-02-02. Swedish Nuclear Fuel and Waste Management Company, Stockholm.

Stille H, Olsson P, 1989. First evaluation of rock mechanics. Progress Report 25-89-07. Swedish Nuclear Fuel and Waste Management Company, Stockholm.

Syarifuddin N, Busono I, 1999. Regional stress alignments in the Kutai Basin, East Kalimantan, Indonesia: a contribution from a borehole breakout study. Journal of Asian Earth Sciences. 17:123-135.

Vardoulakis J, Sulem J, Guenot A., 1988. Borehole instabilities as bifurcation phenomena, Int. J. Rock Mech. Min. Sci. & Geomech. Abstr., 25:159-170.

Wanne T, Johansson E, 2003. Äspö Pillar Stability Experiment. Coupled 3D thermo-mechanical modelling, preliminary results. International Progress Report, IPR-03-04. Swedish Nuclear Fuel and Waste Management Company. Stockholm.

Zang W, 1990. Crack Kinks and Crack Closure Modelled by Integral Equation Methods. Doctoral thesis Royal Institute of Technology. Stockholm, Sweden.

Part II:
Modelling Fracture Initiation and Acoustic Emission (AE) Using FRACOD

Baotang Shen

Fracom Ltd.

January 2003

Contents of Part II

		Page
1	**Introduction**	**69**
2	**Theoretical Background of FRACOD**	**71**
2.1	Simulation of joints/fracture in FRACOD	71
2.2	Modelling Fracture propagation	73
2.3	Modelling Fracture Initiation	75
3	**Prediction of Acoustic Emission (AE)**	**81**
3.1	AE location	81
3.2	AE magnitude	83
4	**Application examples**	**85**
4.1	Failure of a shaft under biaxial loading	85
4.2	Failure of a rectangular opening under biaxial loading	87
5	**Conclusions**	**89**
6	**References**	**91**
Appendix A: Properties of newly created fresh fractures		**93**

1 Introduction

An in-situ experiment is planned at Äspö HRL to investigate the stability of pillars between deposition holes-the Äspö Pillar Stability Experiment (APSE). The major objectives of the APSE are:

- To demonstrate the capability to predict spalling in a fractured rock mass;
- To demonstrate the effect of the backfill on the rock mass response;
- To compare 2D and 3D mechanical and thermal predicting capabilities by numerical models.

To assist SKB in the APSE program, FRACOM has proposed to SKB to use FRACOD, a fracture propagation code developed by FRACOM, to model the pillar failure process under loading from excavation, swelling pressure and heating. Two key components of the proposed project are:

- To predict explicitly the fracturing process in the ASPE pillar during various loading process;
- To develop and demonstrate the capacity in FRACOD in predicting Acoustic Emission (AE) during the progressive fracturing process. Hence it will be made possible to directly compare the predicted AE with the AE measurement results to be conducted by Prof Young's group.

The proposed project was approved by SKB and the project is being undertaken. This document summarizes mainly the formulation of AE capacity in FRACOD. Several example results are given to demonstrate the AE function in FRACOD when applied to real problems.

2 Theoretical Background of FRACOD

Acoustic Emission (AE) is a seismic event caused by dynamic rock failure. Although the AE mechanism is still not fully understood, it is considered that in brittle rocks, seismic events are mainly caused by the following sources/processes:

- Rupture of existing fractures (sudden fracture movement);
- Extension of existing fractures (fracture propagation);
- Formation of new cracks/fractures in intact rock (fracture initiation).

To predict the AE events in a rock mass, all above processes have to be considered. FRACOD has the advantages to predict explicit fracturing process and hence the resultant AE. FRACOD is a two-dimensional computer code that was designed to simulate fracture initiation and propagation in elastic and isotropic rock mediums. The code employs the Displacement Discontinuity Method (DDM) principles. It predicts explicitly the fracturing process including fracture failure, fracture propagation, and fracture initiation in intact rock. A brief description of formulation of FRACOD in handling fracture sliding, propagation and initiation are given below. More details can be found in /Shen, 2002/. For those who are familiar with FRACOD, it is recommended to skip this section and go to Section 3.

2.1 Simulation of joints/fracture in FRACOD

FRACOD is based on Displacement Discontinuity Method (DDM). A rock discontinuity (crack, joint, fracture etc.) can be simulated by using DDM elements, which include the opposite surfaces of the discontinuity. For *n* elements for rock discontinuities, a total of *2n* governing equations can be established, where the displacement discontinuities of the crack elements are unknowns. The displacement discontinuities will be obtained by solving the system of governing equations.

For a rock discontinuity in an infinite elastic rock mass, the system of governing equations can be written as

$$\left.\begin{aligned} \overset{i}{\sigma}_s &= \sum_{j=1}^{N} \overset{ij}{A}_{ss}\, \overset{j}{D}_s + \sum_{j=1}^{N} \overset{ij}{A}_{sn}\, \overset{j}{D}_n - (\overset{i}{\sigma}_s)_0 \\ \overset{i}{\sigma}_n &= \sum_{j=1}^{N} \overset{ij}{A}_{ns}\, \overset{j}{D}_s + \sum_{j=1}^{N} \overset{ij}{A}_{nn}\, \overset{j}{D}_n - (\overset{i}{\sigma}_n)_0 \end{aligned}\right\} \quad i=1 \text{ to } N \tag{2-1}$$

where $\overset{i}{\sigma}_s$ and $\overset{i}{\sigma}_n$ represent the shear and normal stresses of the *i*th element respectively; $(\overset{i}{\sigma}_s)_0, (\overset{i}{\sigma}_n)_0$ are the far-field stresses transformed in the crack shear and normal directions. $\overset{ij}{A}_{ss}$, ... , $\overset{ij}{A}_{nn}$ are the influence coefficients, and $\overset{j}{D}_s, \overset{j}{D}_n$ represent displacement discontinuities of *j*th element which are unknowns in the system of equations.

A rock discontinuity has three states: open, in elastic contact or sliding. The system of governing equations (2-1), developed for an open crack, can be easily extended to the case for cracks in contact and sliding. For different crack states, their system of governing equations can be rewritten in the following ways, depending on the shear and normal stresses ($\overset{i}{\sigma}_s$ and $\overset{i}{\sigma}_n$) of the crack.

For an open crack $\overset{i}{\sigma}_s = \overset{i}{\sigma}_n = 0$, therefore the system of governing equations (2-1) can be rewritten as:

$$\left.\begin{aligned} \overset{i}{\sigma}_s = 0 &= \sum_{j=1}^{N} \overset{ij}{A}_{ss} \overset{j}{D}_s + \sum_{j=1}^{N} \overset{ij}{A}_{sn} \overset{j}{D}_n - (\overset{i}{\sigma}_s)_0 \\ \overset{i}{\sigma}_n = 0 &= \sum_{j=1}^{N} \overset{ij}{A}_{ns} \overset{j}{D}_s + \sum_{j=1}^{N} \overset{ij}{A}_{nn} \overset{j}{D}_n - (\overset{i}{\sigma}_n)_0 \end{aligned}\right\} \; i=1 \text{ to } N \tag{2-2}$$

When the two crack surfaces are in elastic contact, the magnitude of $\overset{i}{\sigma}_s$ and $\overset{i}{\sigma}_n$ will depend on the crack stiffness (K_s, K_n) and the displacement discontinuities ($\overset{j}{D}_s, \overset{j}{D}_n$)

$$\begin{aligned} \overset{i}{\sigma}_s &= K_s \overset{i}{D}_s \\ \overset{i}{\sigma}_n &= K_n \overset{i}{D}_n \end{aligned} \tag{2-3}$$

where K_s and K_n are the crack shear and normal stiffness, respectively. Substituting Equation (2-3) into Equation (2-1) and carrying out the simple mathematical manipulation, the system of governing equations then becomes:

$$\left.\begin{aligned} 0 &= \sum_{j=1}^{N} \overset{ij}{A}_{ss} \overset{j}{D}_s + \sum_{j=1}^{N} \overset{ij}{A}_{sn} \overset{j}{D}_n - (\overset{i}{\sigma}_s)_0 - K_s \overset{i}{D}_s \\ 0 &= \sum_{j=1}^{N} \overset{ij}{A}_{ns} \overset{j}{D}_s + \sum_{j=1}^{N} \overset{ij}{A}_{nn} \overset{j}{D}_n - (\overset{i}{\sigma}_n)_0 - K_n \overset{i}{D}_n \end{aligned}\right\} \; i=1 \text{ to } N \tag{2-4}$$

For a crack with its surfaces sliding

$$\begin{aligned} \overset{i}{\sigma}_n &= K_n \overset{i}{D}_n \\ \overset{i}{\sigma}_s &= \pm \overset{i}{\sigma}_n \tan\phi = \pm K_n \overset{i}{D}_n \tan\phi \end{aligned} \tag{2-5}$$

where ϕ is the friction angle of the crack surfaces. The sign of $\overset{i}{\sigma}_s$ depends on the sliding direction. Consequently, the system of equations (2-1) can be presented as:

$$\left.\begin{aligned} 0 &= \sum_{j=1}^{N} \overset{ij}{A}_{ss} \overset{j}{D}_s + \sum_{j=1}^{N} \overset{ij}{A}_{sn} \overset{j}{D}_n - (\overset{i}{\sigma}_s)_0 \pm K_n \overset{i}{D}_n \tan\phi \\ 0 &= \sum_{j=1}^{N} \overset{ij}{A}_{ns} \overset{j}{D}_s + \sum_{j=1}^{N} \overset{ij}{A}_{nn} \overset{j}{D}_n - (\overset{i}{\sigma}_n)_0 - K_n \overset{i}{D}_n \end{aligned}\right\} \; i=1 \text{ to } N \tag{2-6}$$

The displacement discontinuities ($\overset{j}{D}_s, \overset{j}{D}_n$) of the crack are obtained by solving the system of governing equations using conventional numerical techniques, e.g. Gauss elimination method. If the crack is open the stresses ($\overset{i}{\sigma}_s, \overset{i}{\sigma}_n$) on the crack surfaces are zero, otherwise if the crack is in contact or sliding, they can be calculated by Equations (2-3) or (2-5).

The state of each crack (joint) element can be determined using the Mohr-Coulomb failure criterion:

(1) Open joint: $\sigma_n > 0$

(2) Elastic joint: $\sigma_n < 0, |\sigma_s| < c + |\sigma_n|\tan\phi$

(3) Sliding joint: $\sigma_n < 0, |\sigma_s| \geq c + |\sigma_n|\tan\phi$

where a compressive stress is taken to be negative and c is cohesion. If the joint has experienced sliding, $c = 0$.

2.2 Modelling Fracture propagation

Both tensile and shear failure are common in rock masses. Therefore, to effectively predict rock fracture propagation, a fracture criterion for both mode I and mode II fracture propagation is needed. The existing fracture criteria in the macro-scale approaches can be classified into two groups: the principal stress (strain)-based criteria and the energy-based criteria. The first group consists of the Maximum Principal Stress Criterion and the Maximum Principal Strain Criterion; the second group includes the Maximum Strain Energy Release Rate Criterion (G-criterion) and the Minimum Strain Energy Density Criterion (S-criterion). The principal stress (strain)-based criteria are only applicable to the mode I fracture propagation and they relies on the principal tensile stress (strain). To be applied for the mode II propagation, a fracture criterion has to consider not only the principal stress (strain) but also the shear stress (strain). From this point of view, the energy based criteria seem to be applicable for both mode I and II propagation because the strain energy in the vicinity of a fracture tip is related to all the components of stress and strain.

Both the G-criterion and the S-criterion have been examined for application to the mode I and mode II propagation /Shen and Stephansson, 1993/, and neither of them is directly suitable. In a study by /Shen and Stephansson, 1993/ the original G-criterion has been improved and extended. The original G-criterion states that when the strain energy release rate in the direction of the maximum G-value reaches the critical value G_c, the fracture tip will propagate in that direction. It does not distinguish between mode I and mode II fracture toughness of energy (G_{Ic} and G_{IIc}). In fact, for most of the engineering materials, the mode II fracture toughness is much higher than the mode I toughness due to the differences in the failure mechanism. In rocks, for instance, G_{IIc} is found in laboratory scale to be at least two orders of magnitude higher than G_{Ic} /Li, 1991/. Applied to the mixed mode I and mode II fracture propagation, the G-criterion is difficult to use since the critical value G_c must be carefully chosen between G_{Ic} and G_{IIc}.

A modified G-criterion, namely the F-criterion, was proposed /Shen and Stephansson, 1993/. Using the F-criterion the resultant strain energy release rate (G) at a fracture tip is divided into two parts, one due to mode I deformation (G_I) and one due to mode II

deformation (G_{II}). The sum of their normalized values is used to determine the failure load and its direction. G_I and G_{II} can be expressed as follows (Figure 2-1): if a fracture grows an unit length in an arbitrary direction and the new fracture opens without any surface shear dislocation, the strain energy loss in the surrounding body due to the fracture growth is G_I. Similarly, if the new fracture has only a surface shear dislocation, the strain energy loss is G_{II}. The principles of the F-criterion can be stated as follows:

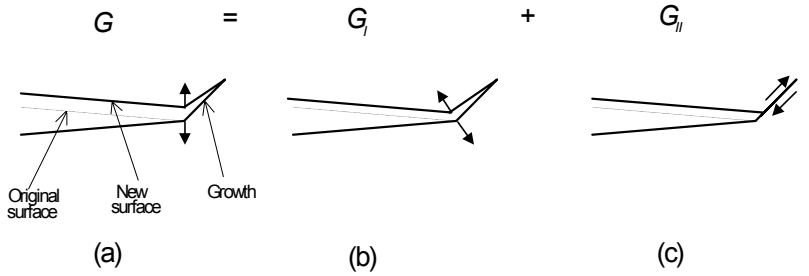

Figure 2-1. *Definition of G_I and G_{II} for fracture growth. (a) G, the growth has both open and shear displacement; (b) G_I, the growth has only open displacement; (c) G_{II}, the growth has only shear displacement.*

(1). In an arbitrary direction *(θ)* at a fracture tip there exists a F-value, which is calculated by

$$F(\theta) = \frac{G_I(\theta)}{G_{Ic}} + \frac{G_{II}(\theta)}{G_{IIc}} \tag{2-7}$$

(2). The possible direction of propagation of the fracture tip is the direction ($\theta=\theta_0$) at which the F-value reaches its maximum value.

$$F(\theta)\Big|_{\theta=\theta_0} = \max. \tag{2-8}$$

(3). When the maximum F-value reaches 1.0, the fracture tip will propagate, i.e.

$$F(\theta)\Big|_{\theta=\theta_0} = 1.0 \tag{2-9}$$

The F-criterion is actually a more general form of the G-criterion and it allows us to consider mode I and mode II propagation simultaneously. In most cases, the F-value reaches its peak either in the direction of maximum tension (G_{Ic} = maximum while G_{IIc}=0) or in the direction of maximum shearing (G_{IIc} = maximum while G_{Ic}=0). This means that a fracture propagation of a finite length (the length of an element, for instance) is either pure mode I or pure mode II. However, the fracture growth may socialite between mode I and mode II during an ongoing process of propagation, and hence form a path which exhibits the mixed mode failure in general.

The F-criterion has been implemented using the DDM method in FRACOD. With the new criterion, FRACOD can predict fracture propagation in both tension (mode I) and shear (mode II).

2.3 Modelling Fracture Initiation

In addition to the propagation of existing fractures, new fractures (cracks) may initiate at the boundaries or in the intact rock. This section describes the criteria used to detect fracture initiation. We also discuss a probabilistic approach to model fracture initiation.

Fracture initiation in intact rock

Fracture initiation often starts from microcrack formation at a stress level of 0.3 - 0.6 of the rock strength /Falls and Young, 1996/. The microcracks coalesce and finally form macro-fractures. Because the FRACOD code is designed to simulate the fracturing process in macro-scale only, we will not be able to consider each individual microcrack in the rock. To effectively consider the early fracture initiation before any final microscale failure, we assume that when the stress reaches 50% of the rock strength at a given location, a macrocrack may form. The crack surface however is assigned the intact rock strength. The crack may propagate only when the strength of the crack surface is exceeded during the subsequent increase in stress. Using this treatment in FRACOD, we will be able to predict that the fracture initiation starts when stress=0.5×strength but the failure occurs when stress=1.0×strength.

Currently in FRACOD the Mohr-Coulomb criterion is used to estimate the strength of intact rock. Other criteria widely used in rock mechanics and rock engineering can also be used, such as Hoek-Brown criterion etc.

Fracture initiation may be caused by tension or shear. For tensile fracture initiation, the tensile criterion is used in FRACOD, i.e. when the tensile stress at a given point of the intact rock exceeds 50% of the tensile strength of the intact rock, a new rock fracture will be generated in the direction perpendicular to the tensile stress (Figure 2-2)

Critical stress of fracture initiation in tension:

$$\sigma_{tensile} \geq 0.5\sigma_t \tag{2-10}$$

Direction of fracture initiation in tension:

$$\theta_{it} = \theta(\sigma_{tensile})+\pi/2 \tag{2-11}$$

where $\sigma_{tensile}$ is the principal tensile stress at a given point, σ_t is the tensile strength of the intact rock, θ_{it} is the direction of the fracture initiation in tension, and $\theta(\sigma_{tensile})$ is the direction of the tensile stress.

The length of the newly generated fracture is determined by the size of the boundary elements in the model. It is currently set to be equal to the length of the smallest element.

When checking for fracture initiation, a large number of grid points with regular spacing are defined in the intact rock. The stresses at each grid point are calculated and examined against the failure criteria. If a fracture initiation is found, new fracture elements are created at the grid point (Figure 2-2).

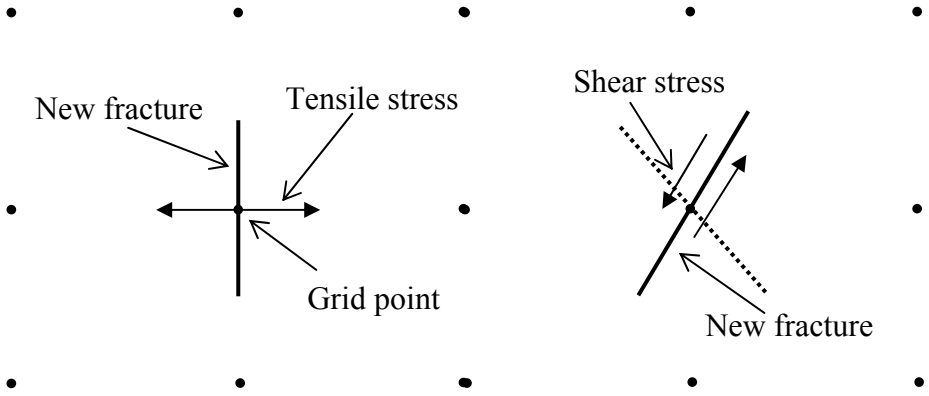

***Figure 2-2**. Fracture initiation in tension or shear in intact rock.*

For a shear fracture initiation, the Mohr-Coulomb failure criterion is used in FRACOD, i.e. when the shear stress at a given point of the intact rock exceeds 50% of the shear strength of the intact rock, a new rock fracture will be generated (Figure 2-2).

Critical stress of fracture initiation in shear:

$$\sigma_{shear} \geq 0.5(\sigma_n \tan(\phi)+c) \tag{2-12}$$

Direction of fracture initiation in shear:

$$\theta_{is} = \phi/2+\pi/4 \tag{2-13}$$

where σ_{shear} is the shear stress in the direction of θ_{is}, σ_n is the normal stress on the shear failure plane, ϕ is the internal friction angle of intact rock, c is the cohesion, and θ_{is} is the direction of potential shear failure, which is measured from the direction of the minimum principal stress.

Because there are always two symmetric shear failure planes at any given point, two fractures are initially added in the model whenever a shear failure is detected. In practice, however, often only one fracture will appear during a shear failure. For this reason, we optimise the two fracture directions and only keep the one that causes the maximum energy release. The optimisation process applied at FRACOD is found to be effective and it leads to a significant reduction of the number of new fractures created during fracture initiation.

The length of the shear fracture initiation depends upon the spacing of the element size, as discussed above for the tensile fracture initiation.

Fracture initiation at boundaries

Fracture initiation at a boundary is not a straightforward task. Fracture initiation at the boundary requires the accurate knowledge of stresses (tangential, normal and shear) of the boundary elements. The DDM method however does not calculate the tangential stress of the boundary elements in its solutions. To obtain the tangential stress for fracture initiation, we need to use the displacements of the adjacent elements.

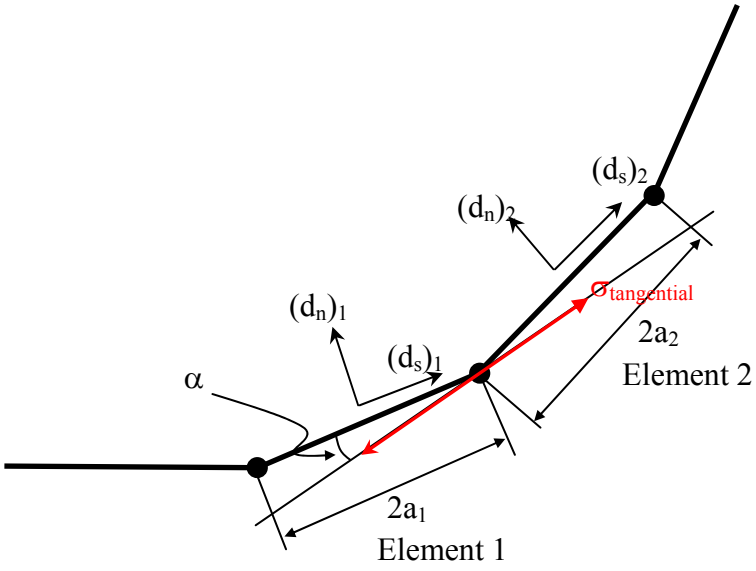

Figure 2-3. *Tangential stress at the connection point of two adjacent elements.*

For the two adjacent elements shown in Figure 2-3, the tangential stress $\sigma_{tangential}$ at the connection point can be calculated by using the displacements at the mid-point of the two elements.

$$\sigma_{\tan gential} = \frac{E}{1-\nu^2} \frac{\left[(d_s)_2 \cos\alpha - (d_n)_2 \sin\alpha\right] - \left[(d_s)_1 \cos\alpha + (d_n)_1 \sin\alpha\right]}{(a_1 + a_2)\cos\alpha} \tag{2-14}$$

where $(d_s)_1$, $(d_n)_1$, $(d_s)_2$, $(d_n)_2$ are the shear and normal displacement of the mid-point of the two adjacent elements. a_1 and a_2 are the half length of the two elements. α is the angle between the tangential line and each element. E is the Young's modulus and ν is the Poisson's ratio.

The normal and shear stresses at the connection point is taken as the average of the normal and shear stresses of the two elements, i.e.

$$\sigma_s = \frac{(\sigma_s)_1 + (\sigma_s)_2}{2} \tag{2-15}$$

$$\sigma_n = \frac{(\sigma_n)_1 + (\sigma_n)_2}{2} \tag{2-16}$$

Both the normal and shear stresses of the boundary elements are known from the DDM solutions.

After obtaining the tangential, normal and shear stresses at the connection point, it is then a straightforward task to determine the possibility of fracture initiation. As discussed before the fracture initiation in the intact rock, the fracture initiation at the boundary is predicted to occur when the stress is 50% of the strength.

Once the fracture initiation is predicted at the boundary point, an element will be added in the most likely failure direction (Figure 2-4). The length of the new element is 3/4 of the size of the shorter element. The new fracture has the same cohesion, friction angle and tensile strength as the intact rock, and it is likely to fail and propagate when the stress reaches 100% of the rock strength.

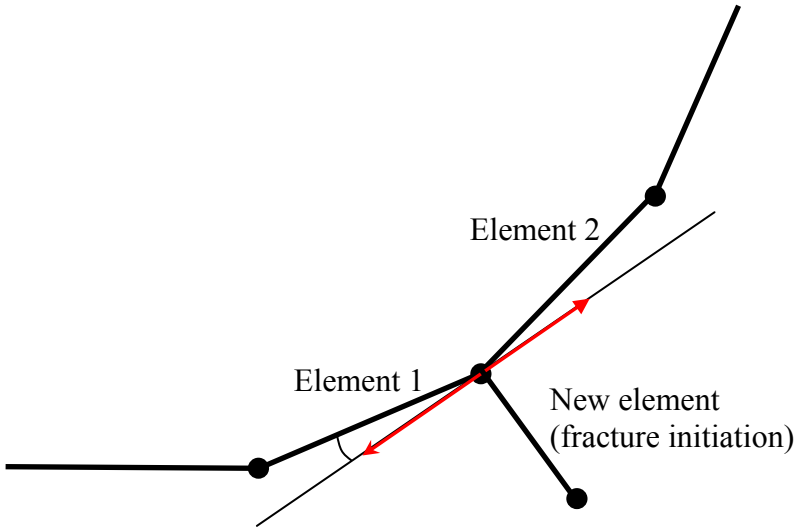

Figure 2-4. *Modelling of a fracture initiation from boundary.*

A boundary may be a straight boundary, a curved boundary, or a boundary with sharp corners. Significantly stress concentration or stress singularity may occur at the boundary. Recent study by /Shen and Rinne, 2001/ has highlighted the complexity of the fracture initiation at boundaries. The initiation procedure outlined above applies only to the straight or curved boundaries. Where stress singularity occurs (e.g. at a sharp corner), intact rock failure criteria are no longer applicable. /Shen and Rinne, 2001/ suggested a hybrid criterion using both the intact rock strength and the fracture tip strength. The hybrid criterion may be suitable for the cases studied but not universally for all cases. There are no simple and yet theoretically sound methods for the prediction of fracture initiation from boundaries with stress singularity.

In FRACOD the sharp corners is ignored for fracture initiation detection. However, it is found that fracture initiation in the intact rock may lead to the final failure linking to the corner. Failure at shape corners is therefore indirectly modelled by the fracture initiation and propagation of the intact rock.

Random fracture initiation

Based on the laboratory test results and AE interpretation /e.g. Li, 1993/, damage (fracture initiation) may starts at a low stress level and increases with increasing stress. Due to rock anisotropy, the chance of failure at a given location increases with increasing stress until the strength is reached.

To consider this fact, we provide an option in FRACOD using the probabilistic approach to simulate fracture initiation. We assume that, at a candidate location, the probability of a fracture initiation depends upon the stress/strength ratio ($\sigma/\sigma_{strength}$):

$$p = 0; \qquad if\,(\sigma / \sigma_{strength} \le 0.5)$$

$$p = 4 \cdot (\sigma / \sigma_{strength} - 0.5)^2; \qquad if\,(0.5 < \sigma / \sigma_{strength} \le 1.0)$$

$$p = 1.0; \qquad if\,(\sigma / \sigma_{strength} > 1.0)$$

where p is the probability of fracture initiation; $\sigma/\sigma_{strength}$ is the ratio of the stress to strength. Note that here we refer both the tensile and compressive stress and strength.

The probability of fracture propagation is plotted in Figure 2-5. The probability curve has a shape similar to that of a typical AE account curve obtained during uniaxial compression tests of rock samples from Aspö /Li, 1993/.

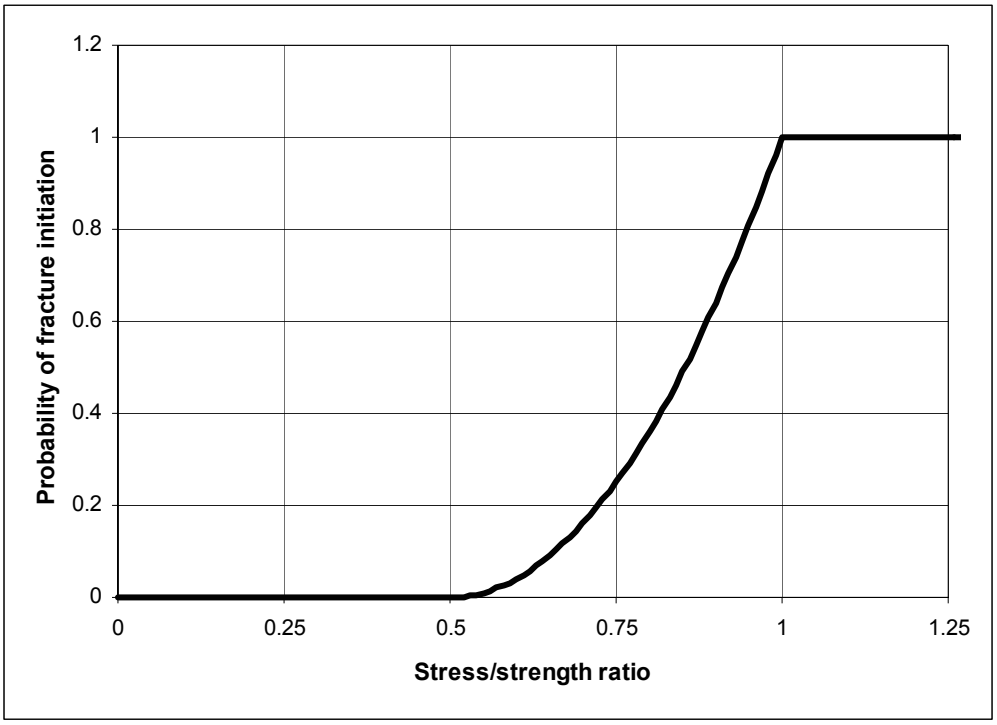

Figure 2-5. *Probability of fracture initiation as a function of the stress/strength ratio.*

The probabilistic approach is recommended when the stress in the region of interests is nearly even, such as for uniaxial compression test of rock sample. Otherwise without the probability approach, most of the fracture initiations in this region will occur at a stress/strength ratio of 0.5.

In regions where high stress concentration exists, however, the probabilistic approach may not be needed because the stress gradient can itself generate progressive propagation of the fracture initiation from high stress region to low stress region.

The probabilistic approach also requires sufficiently large number of elements and/or grid points in the model in order to simulate sufficiently the statistical pattern of fracture initiation.

3 Prediction of Acoustic Emission (AE)

Acoustic Emission (AE) is a low energy seismic event. A seismic event can be considered as sudden inelastic deformation within a given volume of rock that radiates detectable seismic waves. A seismic event is often described by:

- **Location**
- **Magnitude**

3.1 AE location

In brittle rocks, the location of a seismic event is often the location of a rock failure (rock fracture). As discussed before, the likely sources of a seismic event in brittle rocks include sudden fracture movement, fracture propagation and fracture initiation. Since FRACOD models explicitly all the three processes by using DDM elements, it is a straightforward task to predict the location of a seismic event.

(1) Sudden fracture movement

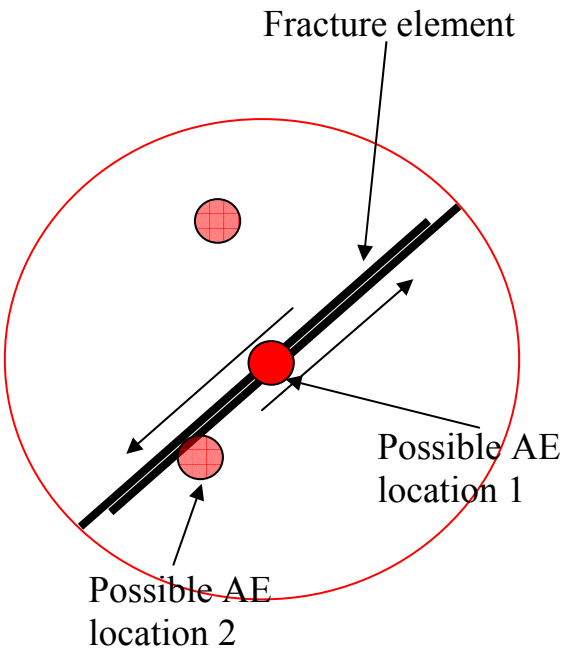

Figure 3-1. *AE events caused by the sudden movement of an existing fracture.*

In FRACOD an existing fracture is divided into a number of elements. Each element is calculated in every step of the calculation to determine the fracture surface movement (including elastic, sliding or opening movement). If the element is found to undergo a movement in any step, an AE event is predicted to occur in the vicinity of this element. Strictly speaking, the location (epicentre) of this AE event should locate at the centre of the element. To avoid overlapping for many AE events from the same element in the process of failure, we assume each individual AE event occurs randomly in a circular region as shown in Figure 3-1.

(2) Fracture propagation

When a fracture propagates, an originally intact rock at the crack tip breaks up and forms an extension of the existing fracture (Figure 3-2). The process of intact rock breakage will cause AE events. The new fracture is simulated by a DDM element. Therefore, one AE event is simulated to occur near the new element. Again the AE event is assumed to locate randomly in a circular region around the new crack element as shown in Figure 3-2.

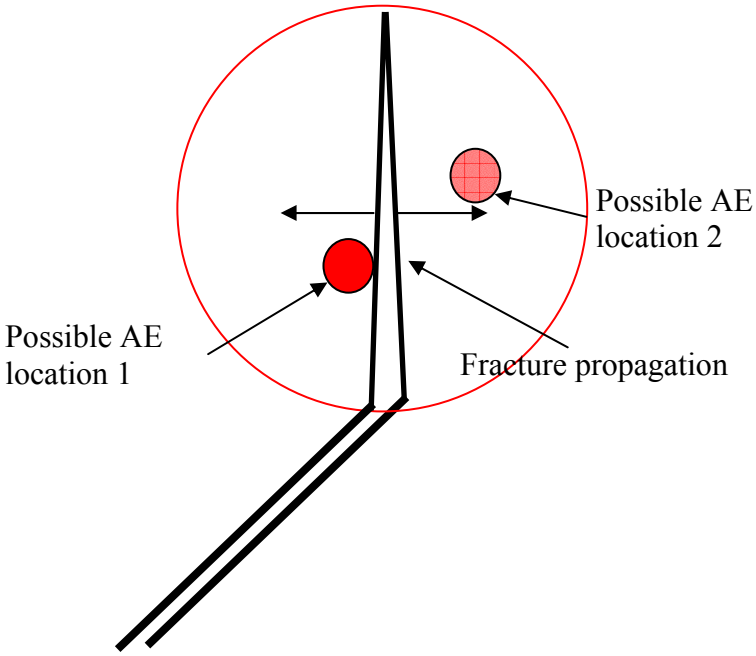

Figure 3-2. *AE events caused by fracture propagation.*

(3) Fracture initiation

Fracturing may occur in an intact rock without the involvement of pre-existing fractures, i.e. fracture initiation. Fracture initiation may occur in tension or shear as shown in Figure 3-3. During this process, new fractures are created and the sudden formation of the new fractures causes dynamic energy release and hence AE events. Similar to the modelling of fracture propagation, FRACOD simulates the fracture initiation by adding a new DDM element. An AE event is therefore predicted in the vicinity of the new element.

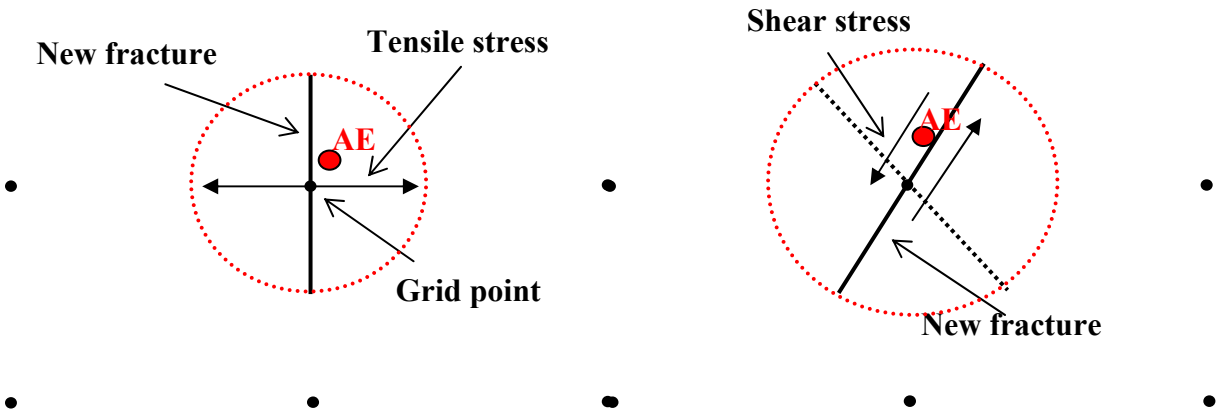

Figure 3-3. *AE events caused by fracture initiation.*

3.2 AE magnitude

The most general description of the strength of a seismic event is the seismic moment /Mendecki, 1997/.

The change of seismic moment in a unit volume can be given by:

$$\Delta\sigma_{ij} = c_{ijkl}\Delta\varepsilon_{kl} \tag{2-17}$$

where c_{ijkl} are elastic constants, $\Delta\varepsilon_{kl}$ is a change in strain, and $\Delta\sigma_{kl}$ is called the seismic moment density tensor or inelastic stress.

The total moment integrated over the source volume V is the seismic moment tensor expressed below:

$$M_{ij} = \int_V c_{ijkl}\Delta\varepsilon_{kl}dV = \int_V \Delta\sigma_{ij}dV \tag{2-18}$$

The moment sensor measures the inelastic deformation at the source during the seismic event and its value measures the permanent inelastic strain produced by the event.

For an idealised plane sliding source, the seismic moment is usually defined as:

$$M = G \cdot \Delta D_s \cdot A \tag{2-19}$$

where ΔD_s is the change of displacement discontinuity (slip) over the source area A. G is the shear modulus.

In case that only tensile failure occurs, the seismic moment can be described as:

$$M = E \cdot \Delta D_n \cdot A \tag{2-20}$$

where ΔD_n is the change of displacement discontinuity (open) over the source area A. E is the Young's modulus.

In FRACOD, the shear and normal displacement discontinuities of both the pre-existing fractures and the new fractures are directly calculated for all fracture elements in every step of fracture propagation. Since the modelling is not conducted in a real dynamic process, it is assumed that each step of fracture propagation (often a fracture growth of one element size) creates a sudden movement. The seismicity caused by this sudden movement is then determined by the incremental deformation of fractures occurred in this step, i.e. ΔD_n and ΔD_s for pre-existing fractures. For new fractures in the first step after fracture propagation or fracture initiation, however, the incremental deformation will be equal to the total fracture deformation (D_n and D_s) because the initial deformation was zero before the formation of the new fractures. In the subsequent steps when the initial deformation is no longer zero the incremental deformation applies.

The area of seismicity A is difficult to assess since the modelling is not conducted in a real dynamic process. For simplicity, we assume the area of seismicity (or AE) is the area of each element.

The seismic moment can be converted to the local seismic magnitude (m_L) using the following relations /Hazzard et al, 2002/:

$$m_L = \frac{2}{3}\log M - 6 \tag{2-21}$$

Obviously the seismic magnitude is sensitive to the size of the elements. Therefore, it is not practical to compare the predicted AE magnitude with the measured magnitude unless the element size is comparable to the rock grain size.

The usefulness of the predicted AE magnitude by FRACOD is the comparison of the different AE events predicted by FRACOD. Since the element size (or the assumed seismicity area) is usually the same for all fracture elements, the predicted AE magnitude is proportional to the movement of each fracture element. The AE magnitude therefore provides an indication of the relative strength of all different AE events.

4 Application examples

Two examples are given below to demonstrate the newly implemented AE function in FRACOD for modelling the stability of rock excavations.

4.1 Failure of a shaft under biaxial loading

The shaft geometry and rock properties are:

- Shaft shape = circular, Shaft diameter = 7.3m
- Intact rock properties: E=40GPa, ν=0.25
- Critical strain energy release rate (fracture toughness): G_{Ic}=200J/m^2, G_{IIc}=2000J/m^2
- Fracture properties: K_n=500GPa/m; K_s=100GPa/m, ϕ_r=0°; cohesion=0
- Rock strength: ϕ_r=40°, c_r=4MPa, σ_t=2MPa;
- Insitu stresses: σ_1=8MPa; σ_3= 4MPa

The shaft is predicted to fail under the given stresses. The final fracture pattern in the shaft wall is shown in Figure 4-1. The predicted AE events during the process of failure are shown in Figure 4-2.

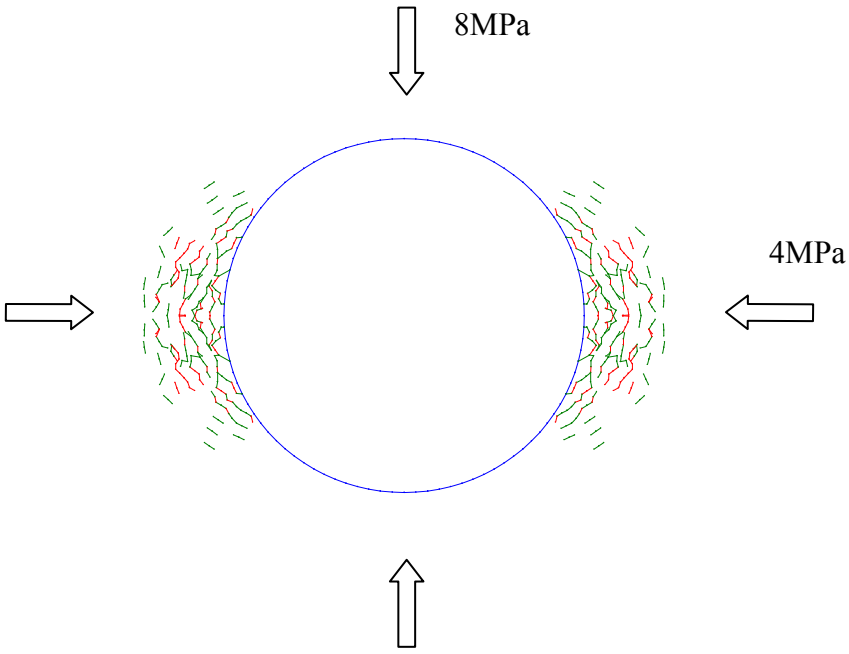

Figure 4-1. *Fracturing pattern in the shaft wall due to biaxial load.*

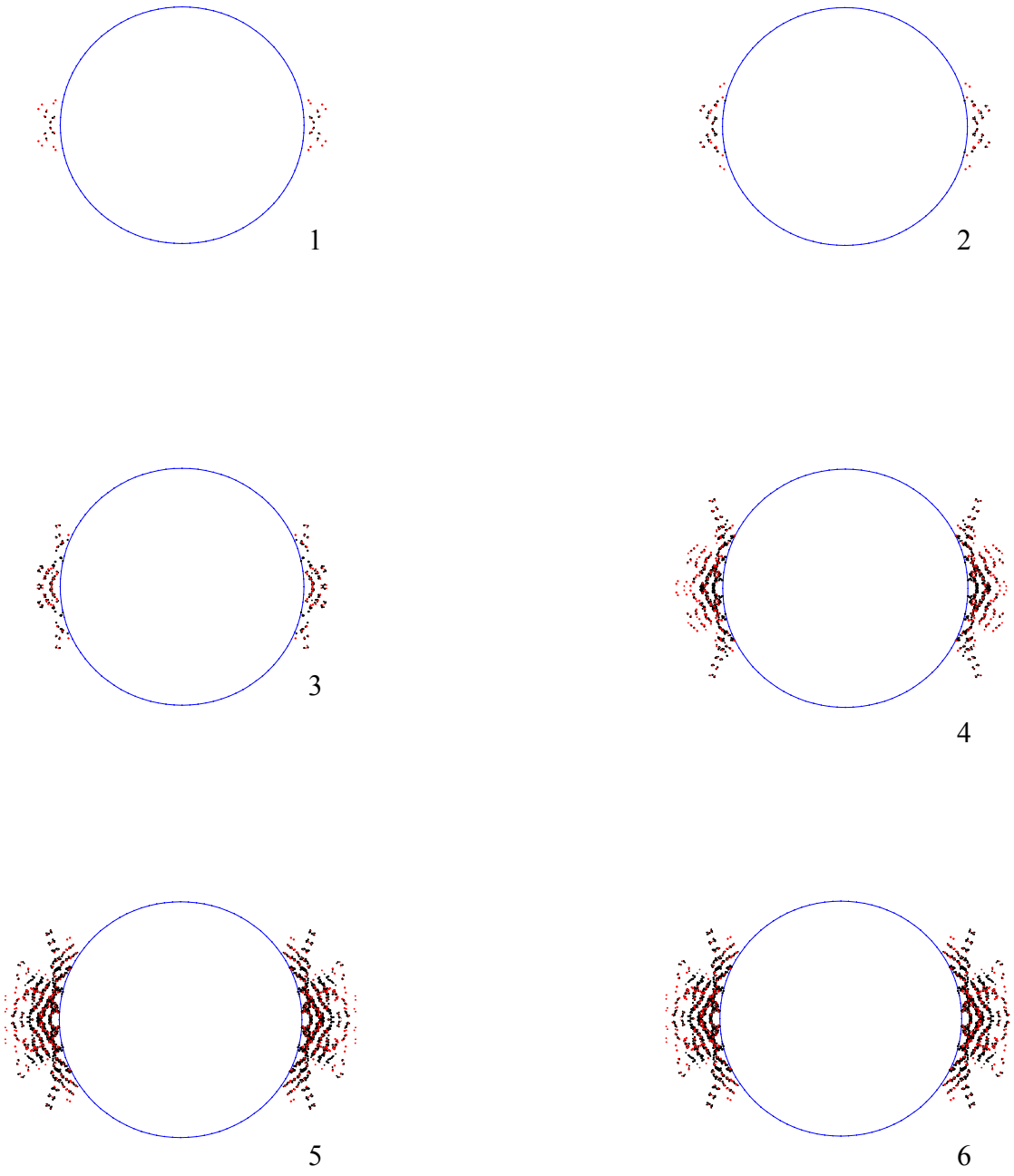

Figure 4-2. *Predicted AE events in the shaft wall during the process of failure.*

4.2 Failure of a rectangular opening under biaxial loading

The excavation geometry and rock properties are given below.

- Opening shape = rectangular
- Opening dimension = 2m×2m
- Intact rock properties: E=40GPa, ν=0.25
- Critical strain energy release rate (fracture toughness): G_{Ic}=50J/m^2, G_{IIc}=500J/m^2
- Fracture properties: K_n=1000GPa/m; K_s=10GPa/m, ϕ_r=30°; cohesion=0
- Rock strength: ϕ_r=30°, c_r=30MPa, σ_t=10MPa
- Insitu stresses: σ_1=50MPa; σ_3= 22.5MPa

The opening is predicted to fail under the given stresses. The final fracture pattern in the opening is shown in Figure 4-3. The predicted AE events during the process of failure are shown in Figure 4-4.

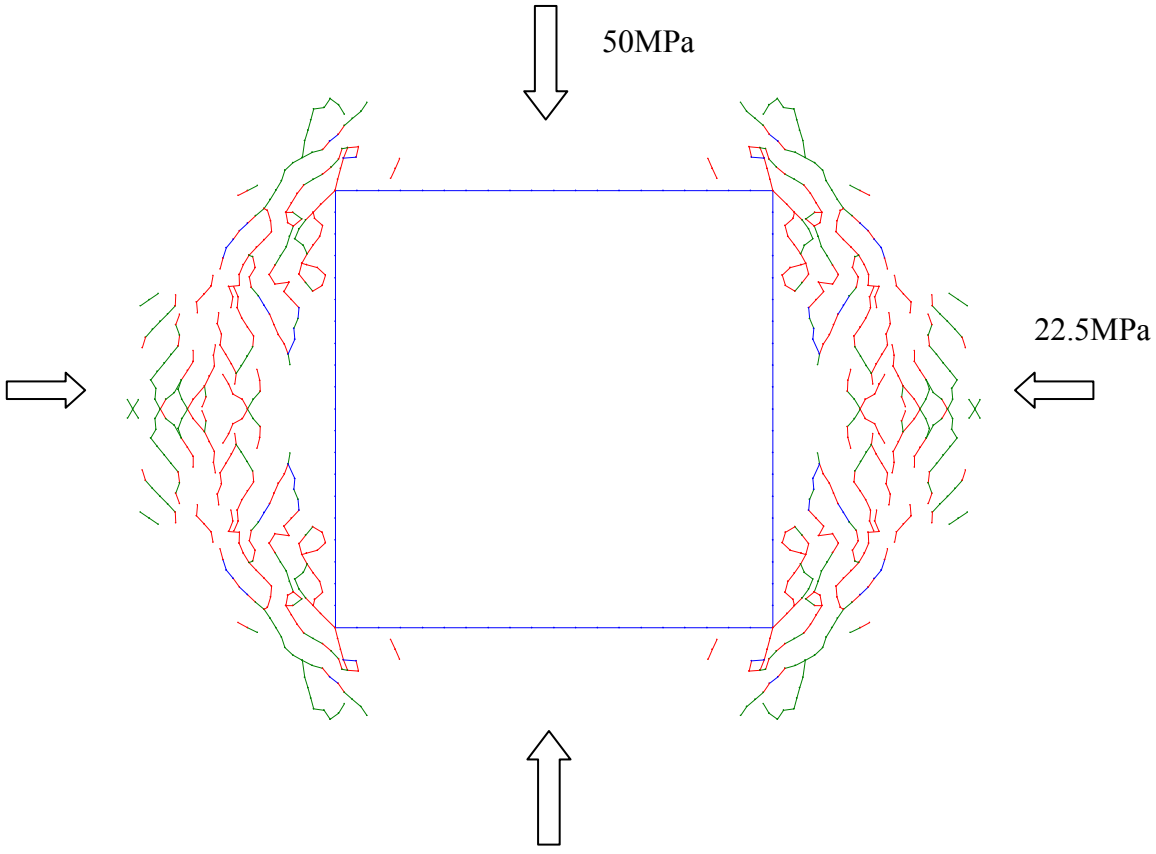

Figure 4-3. *Fracturing pattern in the shaft wall due to biaxial load.*

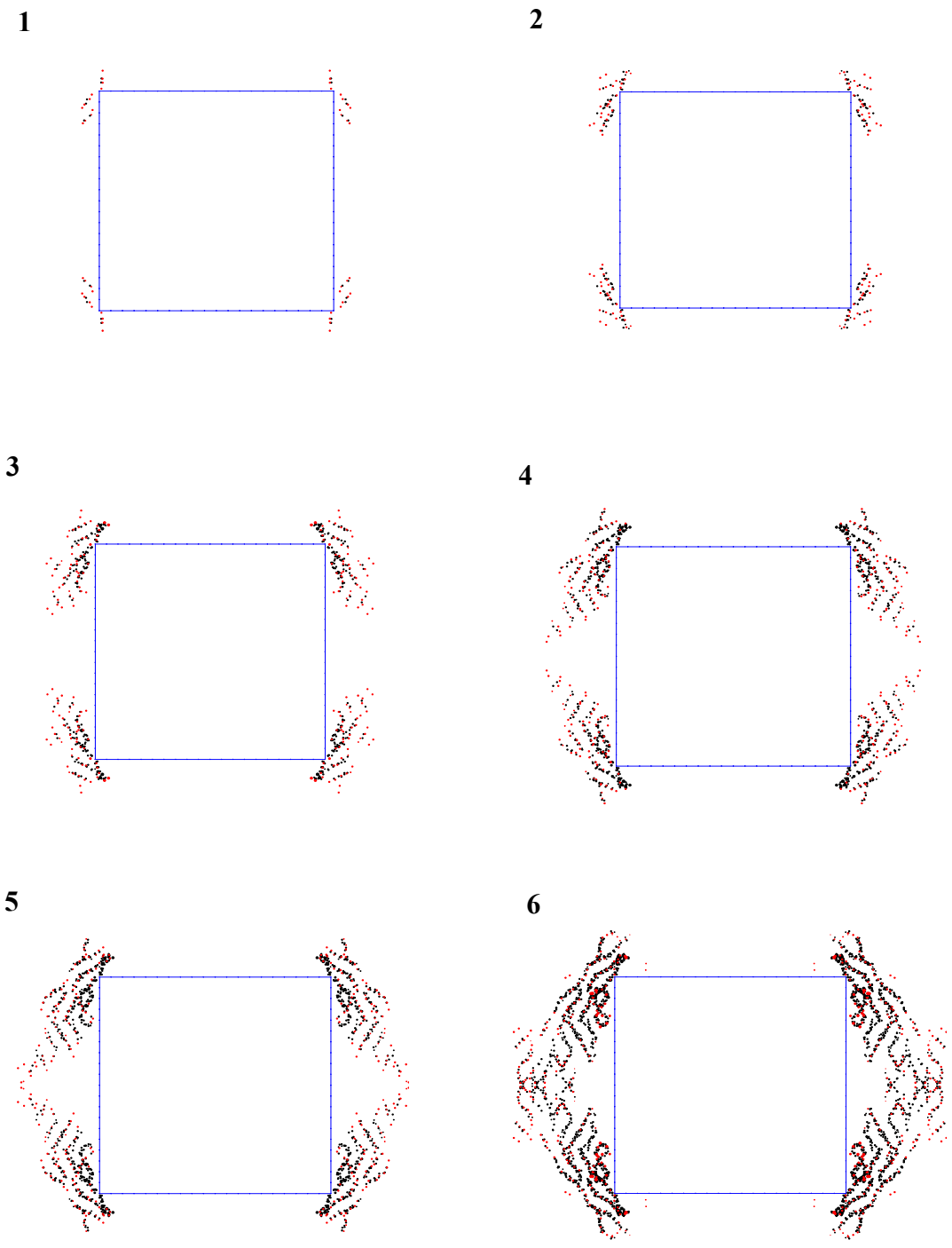

Figure 4-4. *Predicted AE events in the wall of a rectangular opening during failure.*

5 Conclusions

The current version of FRACOD uses a simple fracture initiation criterion. The code predicts the formation of new fractures at the boundaries or in intact rocks. In FRACOD, fracture initiation is assumed to start when the stress reaches 50% of the strength. Final failure however will occur only when 100% of the rock strength is reached.

FRACOD has provided a probabilistic option for fracture initiation. The probability of the fracture initiation is a function of the stress/strength ratio. This option is particularly useful when simulating problem with no or slight stress gradients.

The AE function implemented in FRACOD is for the idealised planar sources only, i.e. fracture sudden movement or fracture initiation. It is demonstrated that FRACOD predicts well the locations of AE events through the fracturing process. FRACOD also predicts relative magnitude of the AE events for comparison between different events. It is, however, not recommended to rely too much on the absolute value of the predicted AE magnitude because it is sensitive to the element size.

6 References

Falls DS, Young RP, 1998. Acoustic emission and ultrasonic-velocity methods used to characterise the excavation disturbance associated with deep tunnels in hard rock. Tectonophysics. Vol 289, pp. 1-15.

Hazzard JF, Collins DS, Pettitt WS, Young RP, 2002. Simulation of unstable fault slip in Granite using a bonded-particle model. Pure and Applied Geophysics. 159:221-245.

Li C, 1993. Deformation and Failure of Brittle Rocks under Compression. Doctoral Thesis. Lulea University of Technology, Sweden. 1993:118D, ISSN 0348-8373.

Li VC, 1991. Mechanics of shear rupture applied to earthquake zones. In: Fracture mechanics of rock, Atkinson K.B. (ed). Academic Press, London, pp. 351-428.

Mendecki AJ, 1997. Seismic Monitoring in Mines. Chapman & Hall (publisher).

Shen B, Stephansson O, 1993. Modification of the G-criterion of crack propagation in compression. Int. J. of Engineering Fracture Mechanics. 47(2):177-189.

Shen B, Rinne M, 2001. Generalised criteria for fracture initiation at boundaries or crack tips. Report prepared for SKB.

Shen B, 2002. FRACOD Version 1.1, User's manual. Fracom Ltd.

Appendix A: Properties of newly created fresh fractures

Normal stiffness:

Bandis et al. (1983) provided the following equations to estimate the fracture normal stiffness for joints:

$$K_n = K_{ni}\left[1 - \frac{\sigma_n}{V_m K_{ni} + \sigma_n}\right] \qquad \text{(A-1)}$$

where K_n is joint normal stiffness in MPa/mm, K_{ni} – joint initial normal stiffness at zero normal stress in MPa/mm, σ_n – joint normal stress in MPa and V_m is maximum joint closure in mm.

V_m can be estimated by using the equation below:

$$V_m = C\left[\frac{JCS}{a_j}\right]^D \qquad \text{(A-2)}$$

where JCS – joint compressive strength in MPa, a_j is joint initial aperture in mm unit, C and D are empirical coefficients (C = 8.57 and D = -0.68 for the 1st shear cycle).

Joint initial aperture a_j can be calculated using Equation (3):

$$a_j = \frac{JRC}{5}\left(0.2\frac{\sigma_c}{JCS} - 0.1\right) \qquad \text{(A-3)}$$

where JRC – joint roughness coefficient, σ_c – rock uniaxial compression strength in MPa.

Implementation in FRACOD for new fresh fractures can be summarized as follows.

The following assumptions/treatments are used:

- JCS = σ_c

- JRC = 20 for tensile fracture and JRC = 5 for shear fracture (Barton 2002, personal communication)

FRACOD can only use constant K_n once it is determined using the initial JRC values

σ_n is the normal stress on the shear failure surface when the rock fails under uniaxial compressive stress σ_c. σ_n is halved if the new fracture is formed in tension to consider future compressive surface contact.

Dilation angle

Barton (1986) suggested using Equation (4) to estimate the fracture dilation angle.

$$\phi_d = \frac{1}{2} JRC \log_{10}\left(\frac{JCS}{\sigma_n}\right) \qquad \text{(A-4)}$$

where ϕ_d – fracture dilation angle in degrees

Implementation in FRACOD for new fresh fractures: ϕ_d is calculated using Equation (4) and ϕ_d is modelled to be constant.

Friction angle and cohesion

The new fractures are often curved or kinked. It is unlikely to experience large shear displacement during fracture propagation in a limited region. Therefore, it is considered that the peak fracture strength (rather than the residual strength) applies to these fractures.

Accordingly, it is assumed in FRACOD that the newly created fractures have the same friction angle and cohesion as the intact rock. Once sliding, the fracture will lose its cohesion but the friction angle keeps the same.

Examples

Using the data provided by SKB for the APSE project, the following fracture properties are obtained. In the calculation it is assumed that the length of fracture initiation is about 90mm (it is taken as the smallest boundary element size of the FRACOD model).

New fresh fracture properties --- Shear fractures

K_n	4643 (GPa/m)
Friction angle	49.0 (°)
Cohesion	31 (MPa)
Dilation angle	2.3 (°)

New fresh fracture properties --- Tensile fractures

K_n	320 (GPa/m)
Friction angle	49.0 (°)
Cohesion	31 (MPa)
Dilation angle	12.1 (°)

Part III:

Reconstruction of Stress Field Using an Inverse Technique for the APSE Pillar Model

Hee-Suk Lee and Lanru Jing

Fracom Ltd.

January 2003

Contents of Part III

		Page
1	**Introduction**	**99**
2	**Method of solution**	**101**
2.1	Basic concept of inverse problem	101
2.2	Inverse boundary element formulation	102
2.3	Solution technique	104
3	**Code development and data transfer to FRACOD**	**107**
3.1	Description of the developed code	107
3.2	Note on data transfer	108
4	**Reconstruction of the pillar model**	**111**
4.1	Model specification	111
4.2	Reconstructed of stress field after excavation	113
4.3	Reconstruction of stress field after heating	119
5	**Conclusions**	**125**
6	**References**	**127**

1 Introduction

Äspö Pillar Stability Experiment (APSE) has been planned to assess the possibility of spalling and rock failure around pillars between deposition holes for high-level nuclear waste repository.

In this experiment, thermal loading and water pressure will be applied to simulate possible heating and swelling effect from deposited nuclear fuel and buffer material, respectively. To predict the accurate fracturing process from the experimental configuration, these loading effects should be considered properly during the modelling work.

FRACOD has been used to model the fracture initiation and propagation around the tunnels and boreholes for underground nuclear waste repository. The code has been updated in many respects, including AE monitoring, more accurate prediction of fracturing process etc. for APSE project. However, FRACOD still cannot simulate the effect of thermal loading, which would be one of the essential sources of loading at the repository.

The direct consideration of coupled thermo-mechanical effect would be best solution for this purpose. However, the formulation is very difficult and time-consuming to implement directly in the FRACOD. Therefore, an alternative way to simulate the APSE model with thermal loading has been sought, and an inverse Boundary Element technique to reconstruct stress field from APSE model configuration was adopted for the solution.

This report summarizes the modelling efforts to reconstruct the stress field from APSE model accurately. The reconstructed stress field has being used for the simulation of the pillar model with FRACOD.

2 Method of solution

2.1 Basic concept of inverse problem

Recently, inverse problems have received much attention from the various field of engineering for example, in the source identification in solid mechanics and heat conduction, geophysics and seismology, image processing and biomedical engineering /Zhang et al., 1995/. In the field of rock mechanics, the term 'back analysis' /Sakurai, 1997/ has been broadly used to denote all inverse techniques for minimizing the gaps between field measurements and numerical models.

Strictly speaking, there are two kinds of inverse problems in the solid mechanics, that is, one is source reconstruction problem and the other is parameter identification problem /Bezerra and Saigal, 1995/. In the source reconstruction, usually unknown boundary conditions are determined using observed field quantities inside domain or over-prescribed boundary conditions. Parameter identification is the matter of characterisation of unknown material parameters such as elastic modulus, Poisson's ratio, cohesion etc. with the knowledge of field quantities along the boundaries or inside domains. Here, we will focus only on source reconstruction problem for our application.

To illustrate the basic concept schematically, consider homogeneous, isotropic, linear elastic two-dimensional continuum Ω, surrounded by its boundary Γ, as shown in Figure 2-1(a). In usual boundary value problem, the basic solution is to determine the unknown quantities inside boundary such as stresses, strains and displacements after solving unknown boundary quantities (t_1, u_2) if appropriate boundary conditions are specified either displacements ($u_1 = \overline{u}$) or tractions ($t_2 = \overline{t}$) along all boundaries. In the figure, subscript 1 denotes specified displacements boundaries, while subscript 2 denotes specified traction boundaries.

On the other hand, some portion of the boundaries is also both unknown displacements and tractions (u_3, t_3) in inverse problems, thus it cannot be solved directly in boundary value senses because number of unknowns is always larger than number of equations. However, if some quantities, say stresses for our problem, are known at some points inside the domain, number of the equations can be increased to get a solution. Usually the solution of an inverse problem does not always satisfy stability and uniqueness in itself, so it is generally called ill-posed problem/Turco, 2001/. Either iterative or non-iterative, some special techniques should be applied to get a meaningful solution/Hansen, 1992/.

Based on this concept, any stress distribution from results from other numerical modelling can be reconstructed after solving unknown tractions and distribution with known stress distribution at some points inside the model. The reconstructed tractions along unknown boundaries can be used again to calculate all other stresses inside domain. FRACOD uses boundary element method to calculate the stress inside domain, thus if we use boundary element method and same discretization for a model, calculated tractions can be directly input to FRACOD model.

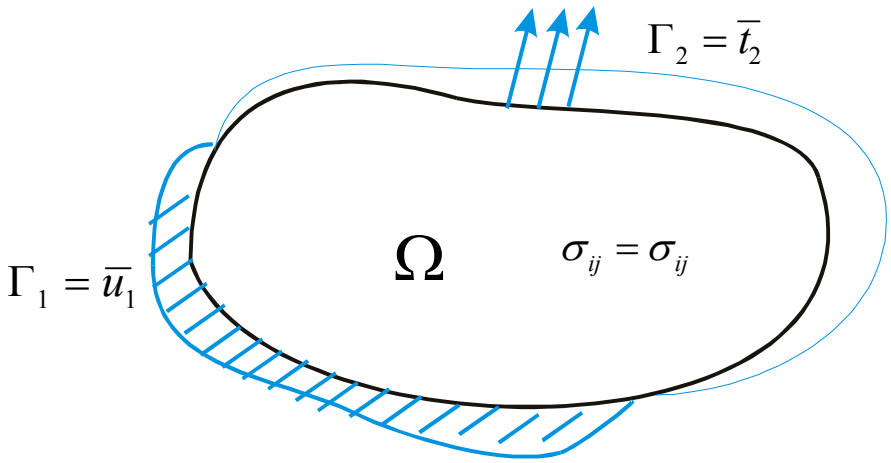

(a)

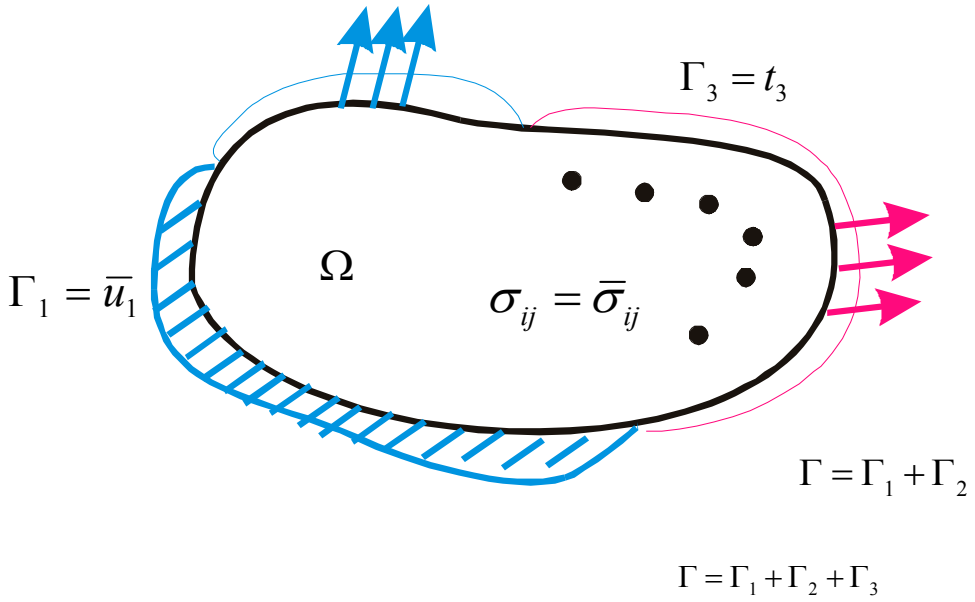

(b)

Figure 2-1. *Basic concept of inverse problem. (a) Forward problem. (b) Inverse problem.*

2.2 Inverse boundary element formulation

BEM is a numerical method for solving PDE, characterized by choosing an appropriate fundamental solution as a weighting function and by using the generalized Green's theorem /Gao and Davis, 2002/It is based on piecewise discretization (collocation) of the problem boundary in terms of sub-boundaries, known as boundary elements (here only consider constant elements) as shown in Figure 2-2.

The direct boundary element formulation is used here together with the Kelvin's fundamental solution on the equilibrium equation. After developing the Somigliana identity and evaluating it with Cauchy singular integral along the boundary, the final displacement boundary integral equation (BIE) for isotropic elastic solid can be written as follows /Gao and Davis, 2002/

$$c_{ij}u_j(P) = \int_\Gamma U_{ij}(Q,P)t_j(Q)d\Gamma(Q) - \int\!\!\!\!\!\!-_\Gamma T_{ij}(Q,P)u_j(Q)d\Gamma(Q) \qquad (2\text{-}1)$$

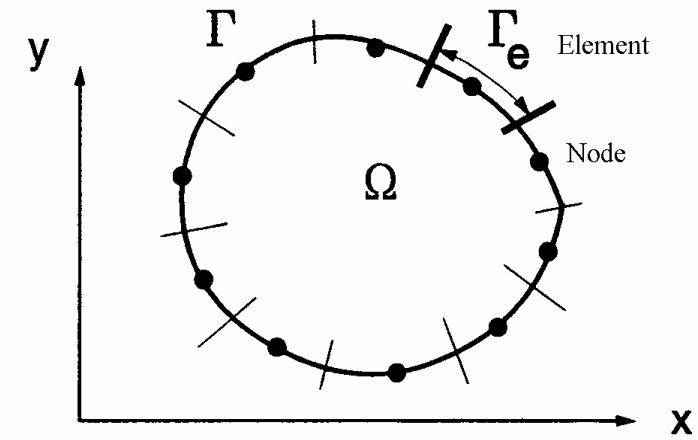

Figure 2-2. *Discretization in boundary element method.*

where the U_{ij} and T_{ij} represent the Kelvin's fundamental solutions for the displacement and tractions, respectively, and also constant

$$c_{ij} = \delta_{ij} + \beta_{ij}(P) \tag{2-2}$$

For a smooth (constant) boundary β_{ij} become $-\delta_{ij}/2$.. Here P and Q denote the source points and field points along the boundary, respectively.

U_{ij} and T_{ij} are usually called kernels, and they can be evaluated analytically or numerically with Gauss integration. The equation (2-1) involves N equations with 2N of unknowns, but after applying the boundary condition, number of unknowns can be reduced to N in the case of forward problem. Thus, the final system of equation can be solved with equation (2-1) alone.

However, the number of unknowns will be increased to N+2n in the case of inverse problems. Here, n denotes the number of points in boundary element which boundary conditions are unknown. So, we need more equations to solve the given problems. As explained above, if we already know stress distribution, we can use following stress boundary integral equations to increase the number of equations

$$\sigma_{ij}(p) = \int_{\Gamma} U_{ijk}(Q,p)t_k(Q)d\Gamma(Q) - \int_{\Gamma} T_{ijk}(Q,p)u_k(Q)d\Gamma(Q) \tag{2-3}$$

where

$$U_{ijk} = \frac{1}{8\pi(1-\nu)}\frac{1}{r^2}\left(C(\delta_{ki}r_{,j} + \delta_{kj}r_{,i} - \delta_{ij}r_{,k}) + 3r_{,i}r_{,j}r_{,k}\right) \tag{2-4}$$

$$\begin{aligned} T_{ijk} = {} & \frac{G}{4\pi(1-\nu)}\frac{1}{r^3}\Big\{3r_{,m}n_m\left[C\delta_{ij}r_{,k} + \nu(\delta_{ik}r_{,j} + \delta_{jk}r_{,i}) - 5r_{,i}r_{,j}r_{,k}\right] \\ & +3\nu(n_i r_{,j}r_{,k} + n_j r_{,i}r_{,k}) + C(3n_k r_{,i}r_{,j} + n_j\delta_{ik} + n_i\delta_{jk}) - Dn_k\delta_{ij}\Big\} \end{aligned} \tag{2-5}$$

where r represents the distance between field and source points, n is outward normal, G is shear modulus and ν is Poisson's ratio. Constants C and D are

$$C = 1 - 2\nu$$
$$D = 1 - 4\nu \tag{2-6}$$

Small *p* in the (2-3) denotes source points inside the domain.

Equation (2-1) and (2-3) constitute the basic formulation for inverse stress reconstruction. After discretizing the model with boundary elements, final equation can be written in matrix form as follows in the case of displacement BIE

$$[H]\{u\} = [G]\{t\} \tag{2-7}$$

and for stress BIE

$$\{\sigma^I\} = [H^I]\{u\} + [G^I]\{t\} \tag{2-8}$$

After application of boundary conditions, the final system of equation can be constructed as

$$[A]\{x\} = \{y\} \tag{2-9}$$

If we use sufficient stress BIE in some points, system of equation is consisted of M×N coefficient matrix, N unknown and M known vectors. Special solution technique should be adopted to solve this problem.

2.3 Solution technique

Final system of equations expressed as (2-9) is partitioned in a blocked matrix form as /Lu and Rizzo, 1999/

$$\begin{bmatrix} [A_{11}] & [A_{12}] \\ [A_{21}] & [A_{22}] \end{bmatrix} \begin{Bmatrix} \{x_1\} \\ \{x_2\} \end{Bmatrix} = \begin{Bmatrix} \{y_1\} \\ \{y_2\} \end{Bmatrix} \tag{2-10}$$

where the subscripts 1, 2 here means not vector or tensor components but rather are related to the boundary subdivisions Γ_1, with known boundary condition and Γ_2 with unknown boundary condition, respectively.

Because main unknowns are x_2, if the block matrix $[A_{11}]$ is invertible, (2-10) can be split into the following two systems of equations:

$$\{x_1\} = [A_{11}]^{-1}\{y_1\} - [A_{11}]^{-1}[A_{12}]\{x_2\} \tag{2-11}$$

$$\left([A_{22}] - [A_{21}][A_{11}]^{-1}[A_{12}]\right)\{x_2\} = \{y_2\} - [A_{21}][A_{11}]^{-1}\{y_1\} \tag{2-12}$$

Vector $\{x_2\}$ contains main unknown tractions along unspecified boundaries. If least square approach with some regularization technique is applied to (2-12), we can get $\{x_2\}$. After obtaining the $\{x_2\}$, unknowns from $\{x_1\}$ can be easily calculated using stored block matrices components. This solution strategy can make the resulting system of equations compact, and also saves the considerable memory.

To solve equations (2-11) and (2-12), inverse matrix of $[A_{11}]$ should be obtained. Since this matrix will be singular, which cannot be solved with usual matrix inversion technique, special generalized inverse (or pseudo inverse) is used with Singular Value Decomposition (SVD).

SVD is a very powerful technique for dealing with matrices that are either singular or else numerically very close to singular /William et al., 1996/. Any M×N matrix A whose number of rows M is greater than or equal to its number of columns N, can be written as the product of 3 components as follows

$$A = U\Sigma V^T = \sum_{i=1}^{n} \mathbf{u}_i \sigma_i \mathbf{v}_i^T \tag{2-13}$$

where $U = (\mathbf{u}_1, ..., \mathbf{u}_n)$ and $V = (\mathbf{v}_1, ..., \mathbf{v}_n)$ are matrices with orthonormal columns $U^T U = V^T V = I_n$, and where

$$\Sigma = \text{diag}(\sigma_1, ..., \sigma_n) \tag{2-14}$$

has non-negative diagonal elements appearing in non-increasing order such that

$$\sigma_1 \geq ... \geq \sigma_n \geq 0 \tag{2-15}$$

The numbers σ_i are the singular values of A while the vectors $\mathbf{u}_i$ and $\mathbf{v}_i$ are the left and right singular vectors of A, respectively.

Generalized inverse can be obtained using above identities as follows

$$A^{-1} = V \cdot [\text{diag}(1/\sigma_i)] \cdot U^T \tag{2-16}$$

It is very interesting that the solution of linear least-square problem can be obtained without any iteration directly when SVD components is used.

Therefore, the solution of (2-12) can be written as /Golub and Loan, 1996/

$$\mathbf{x}_{LSQ} = \sum_{i=1}^{n} \frac{\mathbf{u}_i^T \mathbf{y}}{\sigma_i} \mathbf{v}_i \tag{2-17}$$

In this work, Truncated Singular Value Decomposition (TSVD) is used for solution of (2-17). TSVD is one of the standard regularization methods to discard smaller singular value. When (2-17) is evaluated, p ($\leq n$) is used instead of n for the solution /Martin and Lesnic, 2002/.

After obtaining unknown tractions along unspecified boundaries, we can get all required quantities from regular forward BE analysis with obtained tractions.

3 Code development and data transfer to FRACOD

3.1 Description of the developed code

Based on the formulation explained in chapter 2, an inverse boundary element code (INVBEM) was developed for the stress reconstruction in the FRACOD. This code is written with Fortran 90 and compiled with MS visual Fortran 6.0 compiler, and many subroutines were utilized from BEMECH /Gao and Davis, 2002/.

Figure 3-1 shows basic structure of the INVBEM and Table 3-1 lists the usage of subroutines. After solving inverse problem, the calculated unknown tractions are directly input to FORWARD to get the stress and displacement distribution of the model.

All calculation procedure is performed under DOS environment without any graphic interfaces. To get SVD and pseudo inverse, IMSL Math library LSGRR, LSVRR routines were utilized from the SVD_SOLVE subroutine. Once inverse coefficient matrices are formed, TSVD inverse solutions and corresponding forward solutions are calculated until truncated value has reached to preset number. The developed code has been successfully validated for a simple structure like circular hole.

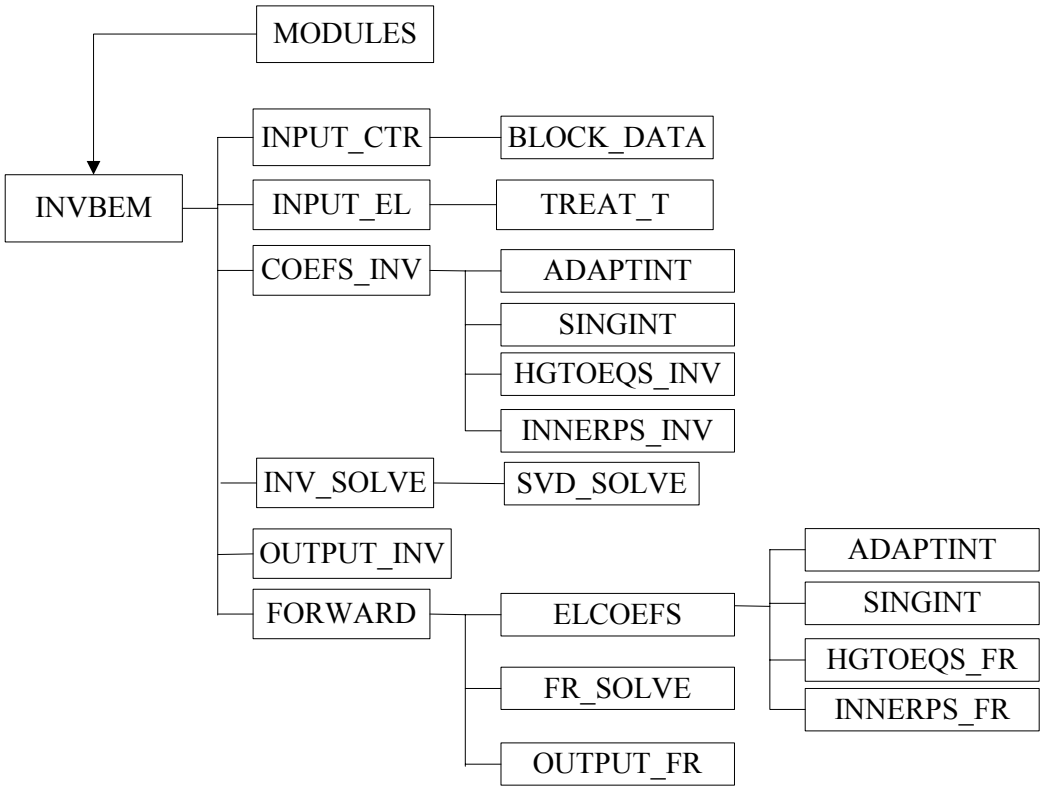

Figure 3-1. *Structure of the INVBEM.*

Table 3-1. List of INVBEM subroutines

Name	Description
INVBEM	Main program
BLOCK_DATA	Initializes variables defined in module FIXED_VALUES
MODULES	Define global control and main variables
TREAT_T	Allocates group tractions to elements
COEF_INV	Forming coefficients for inverse problem
ADAPTINT	Nonsingular integral for Coefficient matrix
SINGINT	Singular integral for Coefficient matrix
HGTOEQS_INV (FR)	Assemble inverse (forward) global coefficient matrix for displacement BIE
INNERPS_INV (FR)	Assemble inverse (forward) global coefficient matrix for stress BIE
INV_SOLVE	Forming block partitioned system of equation and solve inverse problem
SVD_SOLVE	SVD decomposition and TSVD routine
OUTPUT_INV (FR)	Output required quantities from inverse (forward) problem
INPUT_CTR	Reads execution control data
INPUT_EL	Reads input data
FORWARD	Forward analysis routine
ELCOEFS	Forming coefficients for forward problem

3.2 Note on data transfer

INVBEM uses conventional Cartesian coordinate system. Input boundary conditions are defined with x and y directions. However, FRACOD adopt local coordinate system, so proper transformation is needed to transfer boundary conditions from INVBEM to FRACOD.

In addition, FRACOD uses Pa unit instead MPa, it also has to be considered.

Figure 3-2 and Table 3-2 explain the different sign conventions between two codes and possible transformation in the case of rectangular region

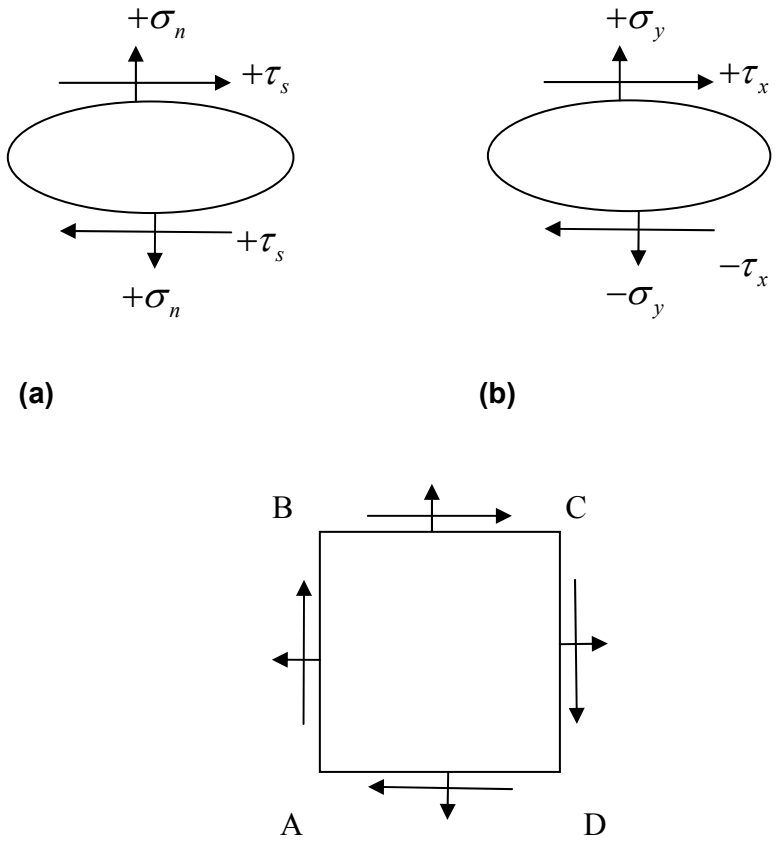

Figure 3-2. *Sign convention for the codes. (a) FRACOD. (b) INVBEM. (c) Transformation for rectangular region.*

Table 3-2. Transformation of the tractions along rectangular region from INVBEM to FRACOD

Section	+ X-traction	+ Y-traction
AB	-ns	ss
BC	ss	ns
CD	ns	-ss
DA	-ss	-ns

c.f. ns: normal stress, ss: shear stress.

4 Reconstruction of the pillar model

4.1 Model specification

To reconstruct the stress field around pillar region, only pillar region is considered to avoid the thermal sources inside domain. Figure 4-1 shows the original configuration

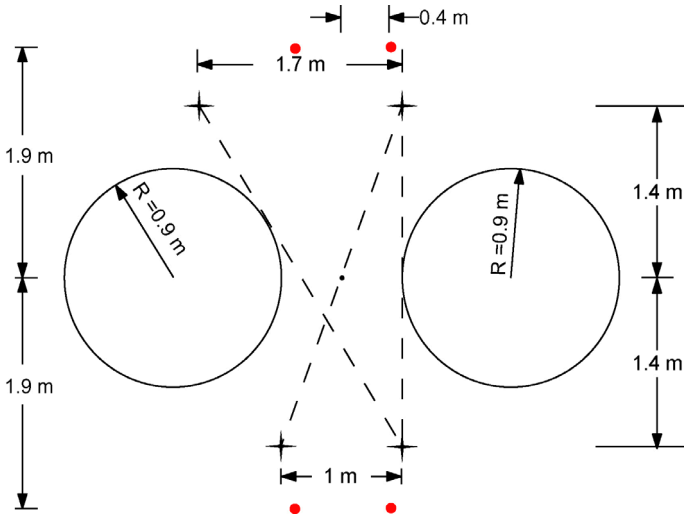

(a)

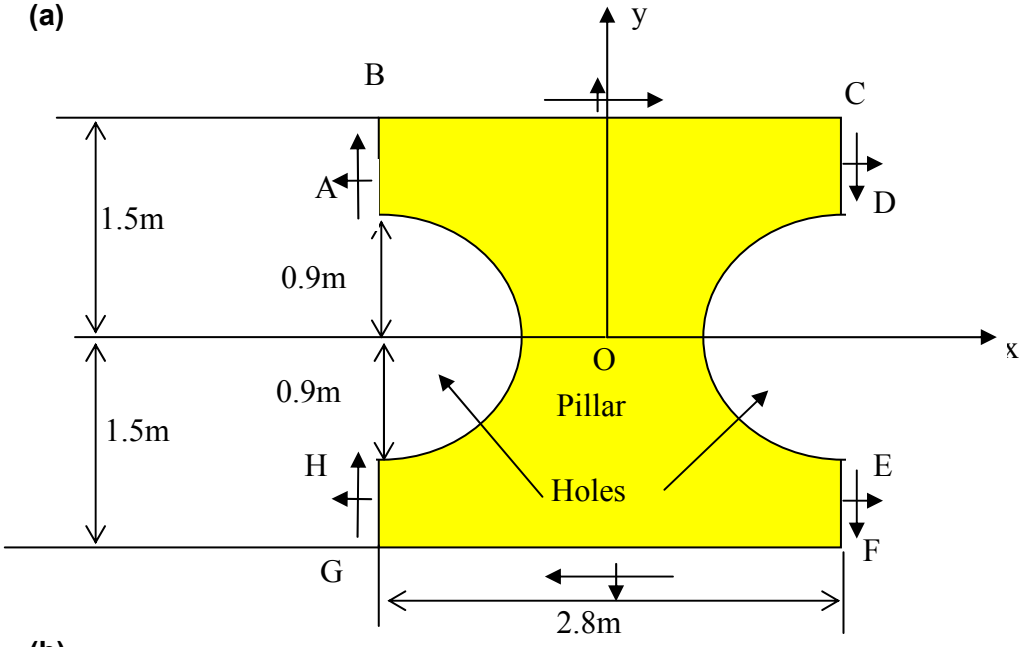

(b)

Figure 4-1. *Specification for the Pillar model. (a) Original configuration (from Golder). (b) ThePillar model.*

for boreholes and the suggested pillar model for stability analysis. The pillar model cannot be symmetric because the original stress distribution will not be symmetric to the any plane due to 3D inclined nature.

In the following, the basic specification and features for the pillar model are listed.

100 constant BE elements (25 for two arches, 15 for upper and lower edges and 5 for 4 side edges) were used for the pillar model.

479 internal points for known stress distribution were selected as input using preliminary modelling results from Examine 3D by SKB (excavation) /Andersson, 2003/ and from JobFem (thermal stress) by Golder /Fredrikkson et al., 2003; Janson et al., 2003/.

Boundary conditions

Excavation stage: zero traction around both arches

Heating stage: normal traction

1 MPa around the right arch to consider backfill (swelling) effects

To ensure equilibrium into the model, some points should be fixed as zero displacement, but very careful choice of the prescribed points is needed because it affects much the accuracy of the model. We used various combinations of fixed displacements, and concluded zero shear (x-) displacement at the middle of upper and lower edges (0,1.5 and 0,-1.5) with zero shear (-y) displacement at a mid point one of the arches (-0.5, 0 or 0.5, 0) produced best results.

Main unknown tractions to be solved by inverse analysis was 50 elements along AB-BC-CD and EF-FG-GH sections

Using each set of stress data, stress field was reconstructed using forward analysis with the obtained unknown tractions.

Input properties were same as Standard APSE parameters for intact rock (E=68GPa and ν=0.24). All other properties such as thermal properties will not be needed for the inverse analysis because all thermal effects are preserved in the stress distribution. The effect of 3D inclined far-field stress is also included in the stress distribution.

Two cases (without slots and with slots) of stress distribution after excavation of boreholes are reconstructed at both 1.5 m and 0.5 m depth below the tunnel floor, respectively. Four stages of thermal stress distribution are reconstructed from after 30 days, 60 days, 90 days and 120 days of heating, respectively.

4.2 Reconstructed of stress field after excavation

Figure 4-2 shows the comparison between original and the reproduced stress field for excavation without slots at 1.5 m below the tunnel floor. As it can be seen in the figures, the reproduced stress shows nearly same distribution for both major and minor principal stresses.

Some differences near middle of holes were detected in the case of minor principal stresses from the preliminary results. This might be the effect of coarser discretization of the model geometry. This problem could be solved using more refined boundary element as shown in Figure 4-2. All the reconstructed values were quite similar for both major and minor principal stresses. Small differences less than one percent will not affect the overall accuracy of the FRACOD model.

Refined model can apparently improve the accuracy of the model especially near mid-pillar region. For all truncated numbers, the reproduced results show similar accuracy in the case of 1.5m below tunnel floor. It is because the singularity of the inverse problem could be diminished by using lots of input stress points.

Figure 4-3 shows the comparison between original and the reproduced stress field for without slots excavation at 0.5 m below the tunnel floor. Even though overall reproduced stress distribution is quite similar with the original one, accuracy of this depth was quite lower than stress of 1.5 m below the tunnel floor. In this depth, distance from tunnel floor is just 0.5 m, so the original stress distribution must have affected by full 3-dimensional effects. It causes more numerical singularity to the models, so the results were much affected by choice of truncation number.

More research will be needed to consider properly the effect of 3 dimensional stress distributions in the future. Nevertheless, this reproduced stress can also be used for the FRACOD simulation because overall trend and maximum stress values of the reproduced one were very similar to those of the original one.

Figure 4-4 and Figure 4-5 represent the comparison of stress distribution for excavation stress with slots at 1.5 m and 0.5 m below the tunnel floor, respectively. Basically, accuracy was quite similar to that without slots.

To compare more detailed distribution near pillar region, stress values along horizontal and vertical sections were extracted from excavation stresses with slots at 1.5 m below the tunnel floor and are shown in Figure 4-6.

As it is expected excellent agreement was obtained between the original and the reproduced values for both major and minor principal stresses. It is expected that reconstructed stress field can be used for the simulation of excavation effect with enough accuracy according to the comparison.

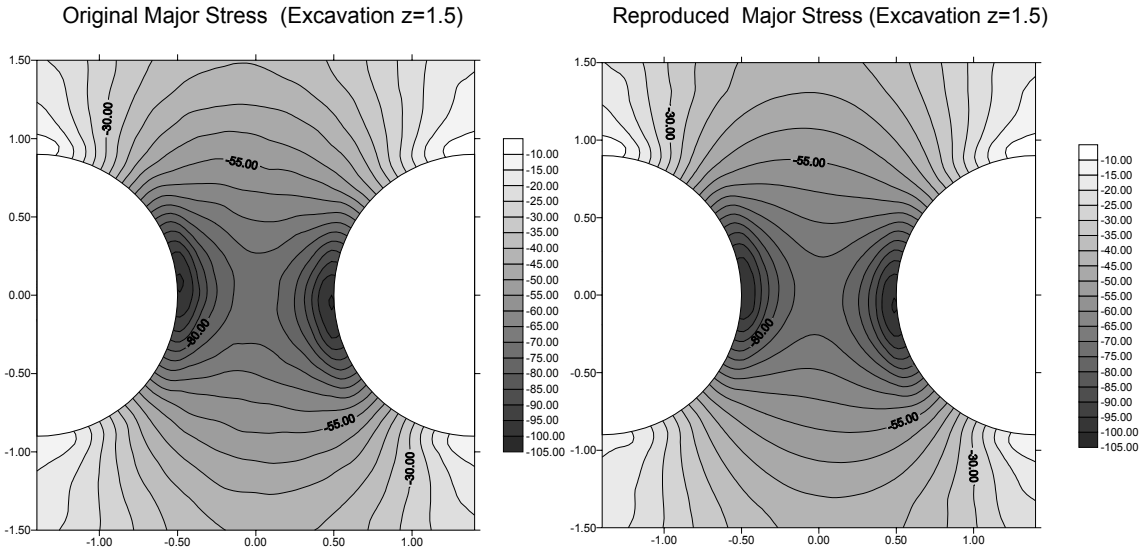

(a)

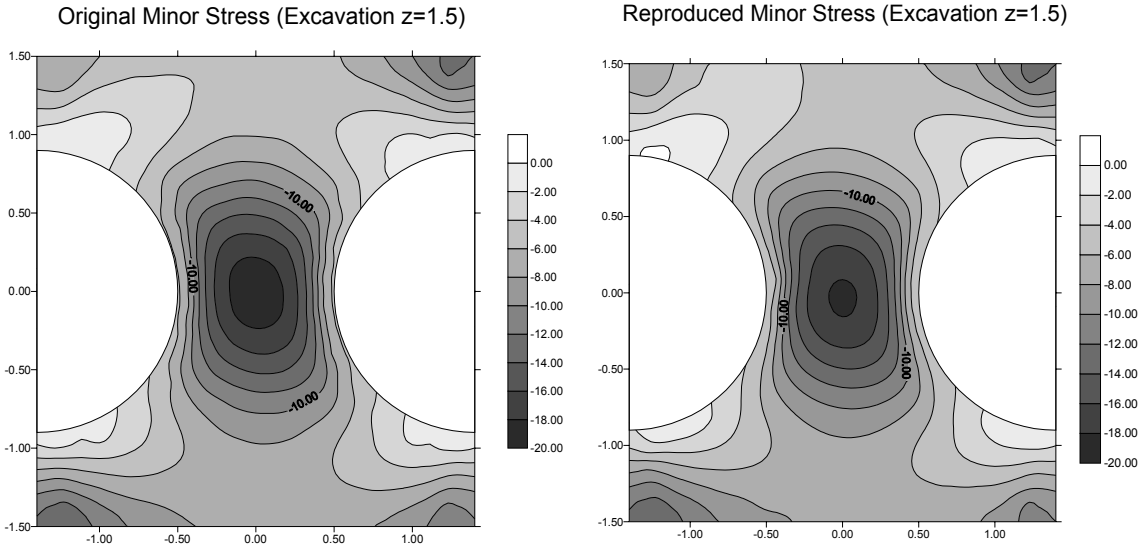

(b)

Figure 4-2. *Comparison between the original and the reproduced stress distribution for excavation without slots at 1.5 m below the tunnel floor (left: original stress, right: reconstructed stress). (a) Major principal stress (σ_1). (b) Minor principal stress (σ_3).*

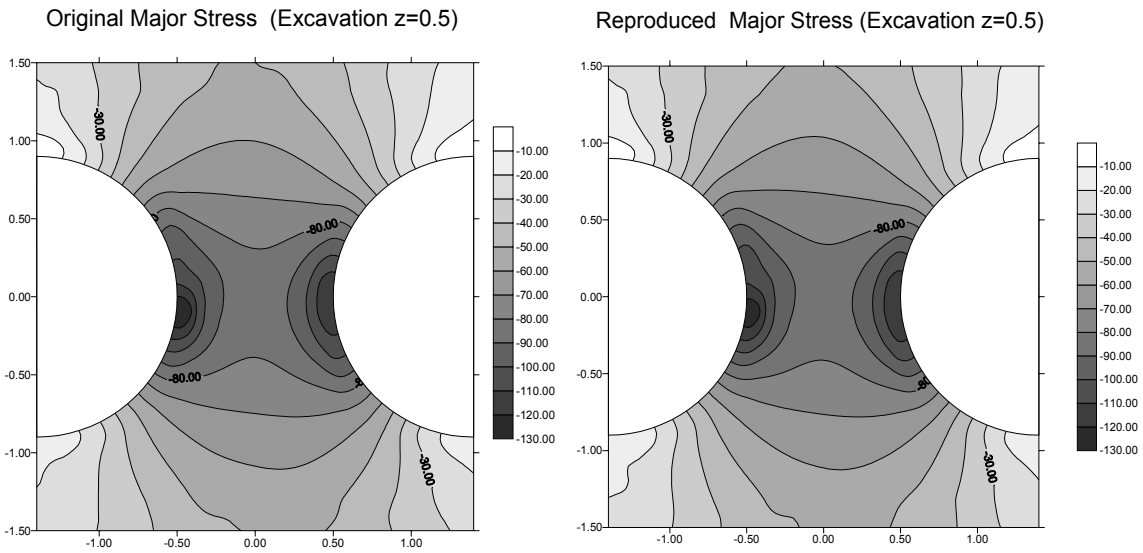

(a)

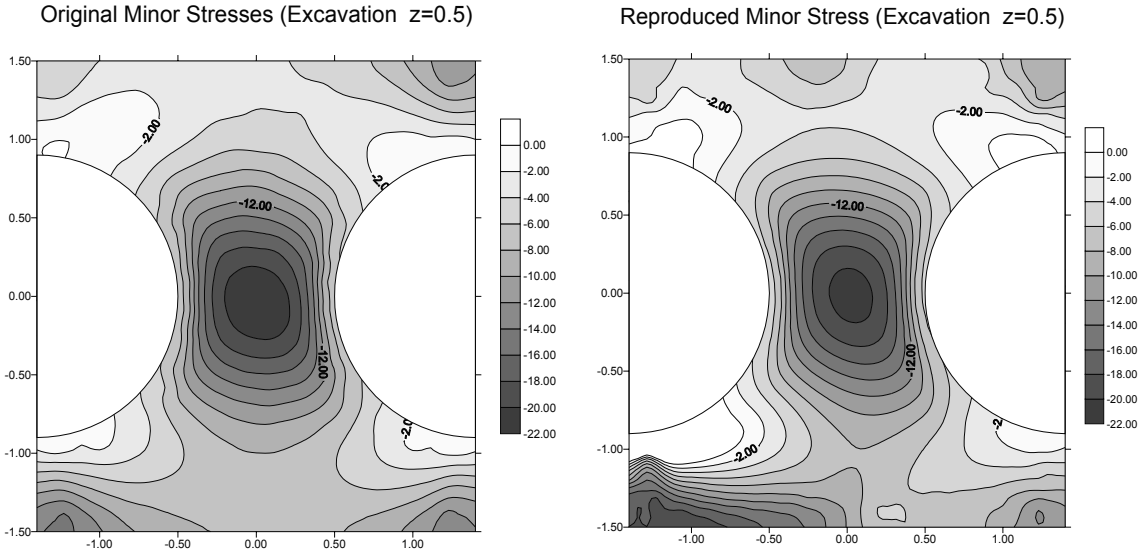

(b)

Figure 4-3. *Comparison between the original and the reproduced stress distribution for excavation without slots at 0.5 m below the tunnel floor (left: original stress, right: reconstructed stress). (a) Major principal stress (σ_1). (b) Minor principal stress (σ_3).*

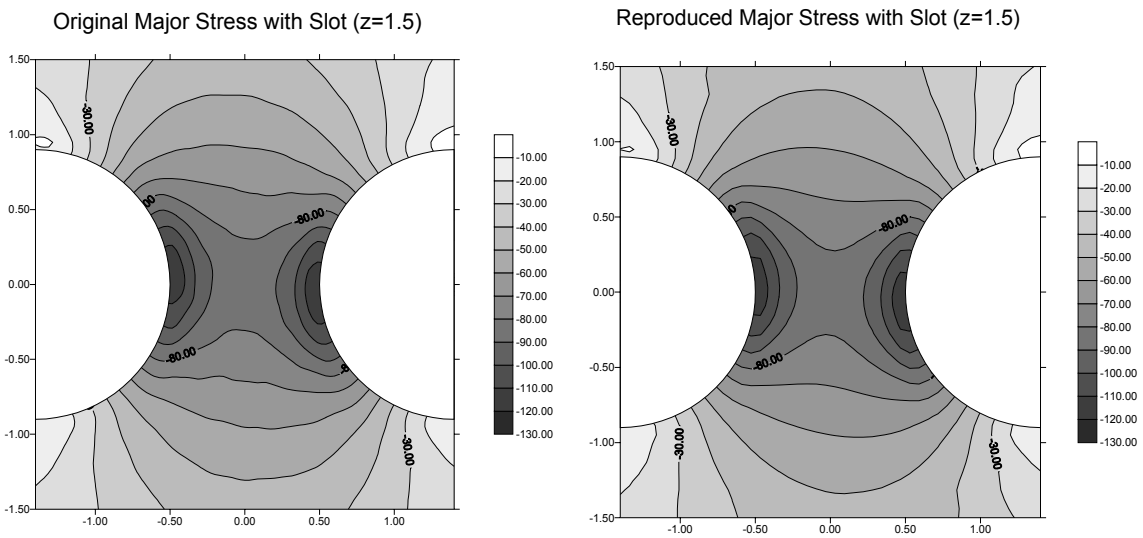

(a)

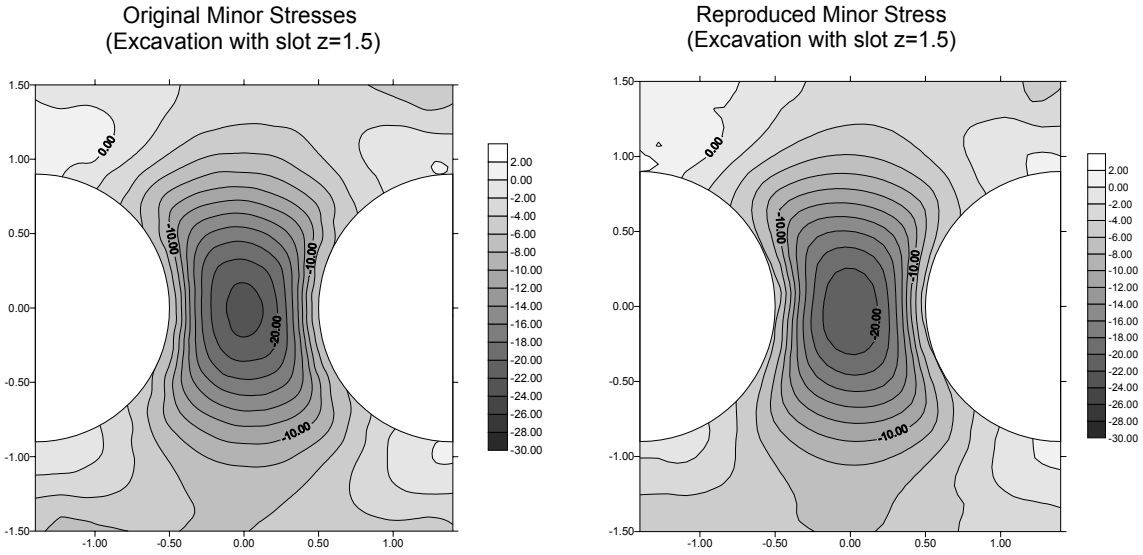

(b)

Figure 4-4. *Comparison between the original and the reproduced stress distribution for excavation with slots at 1.5 m below the tunnel floor (left: original stress, right: reconstructed stress). (a) Major principal stress (σ_1). (b) Minor principal stress (σ_3).*

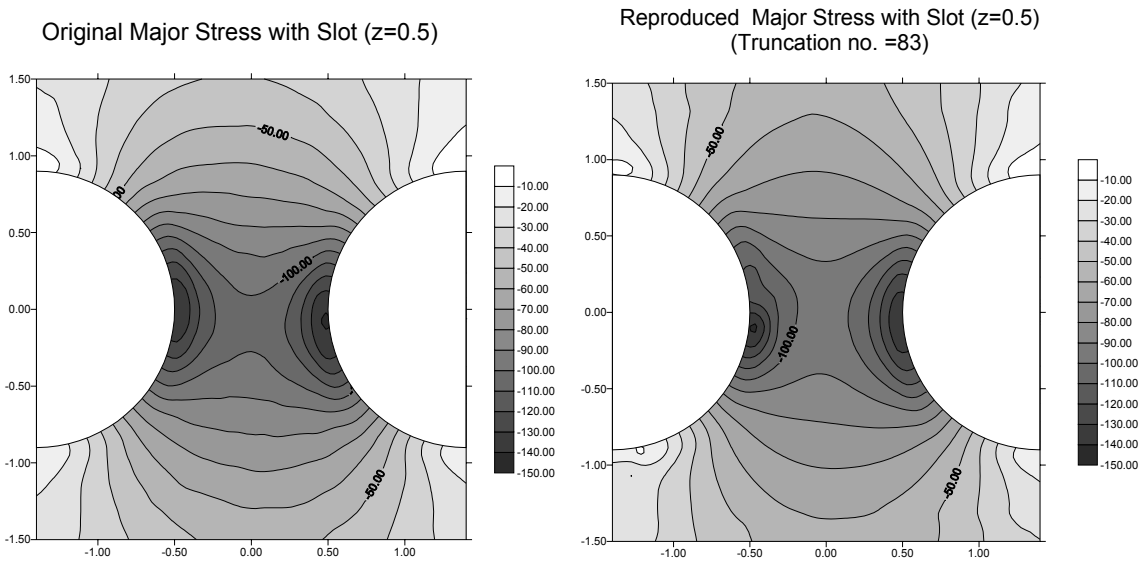

(a)

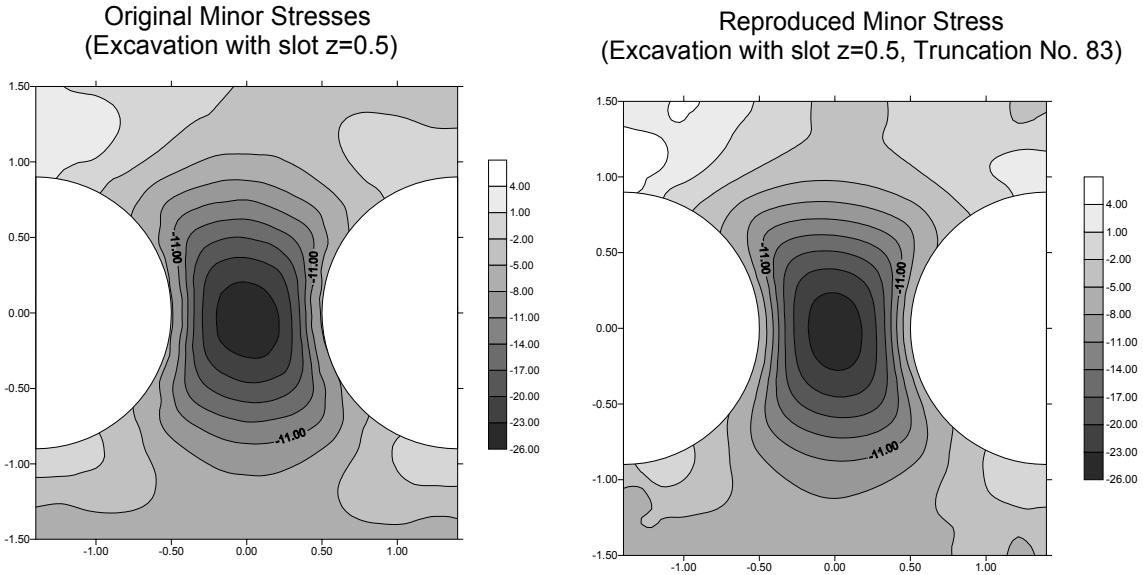

(b)

Figure 4-5. *Comparison between the original and the reproduced stress distribution for excavation with slots at 0.5 m below the tunnel floor (left: original stress, right: reconstructed stress, truncation number: 41). (a) Major principal stress (σ_1). (b) Minor principal stress (σ_3).*

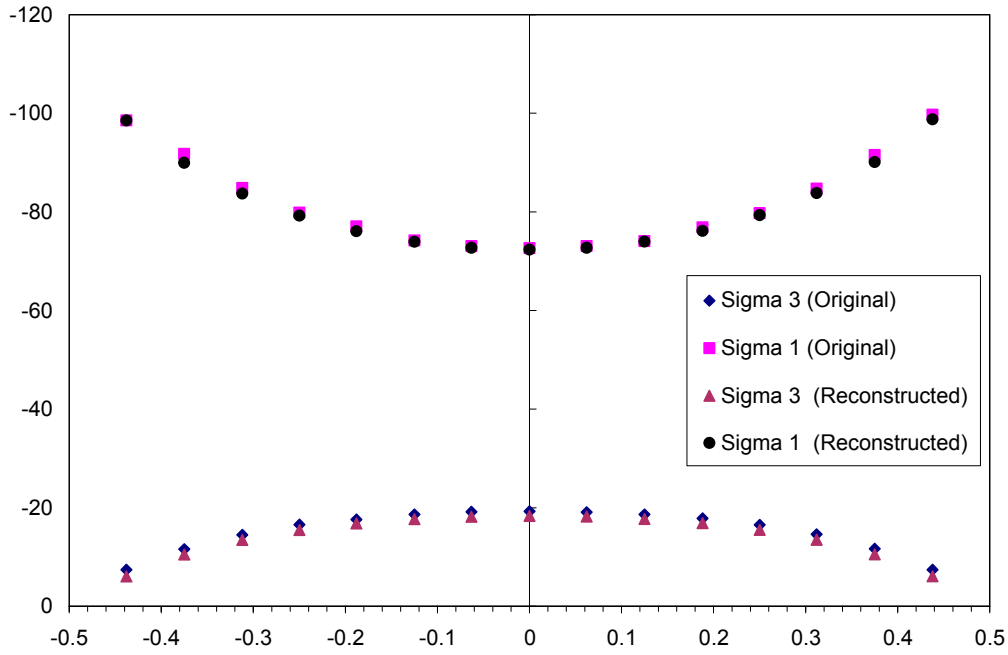

(a)

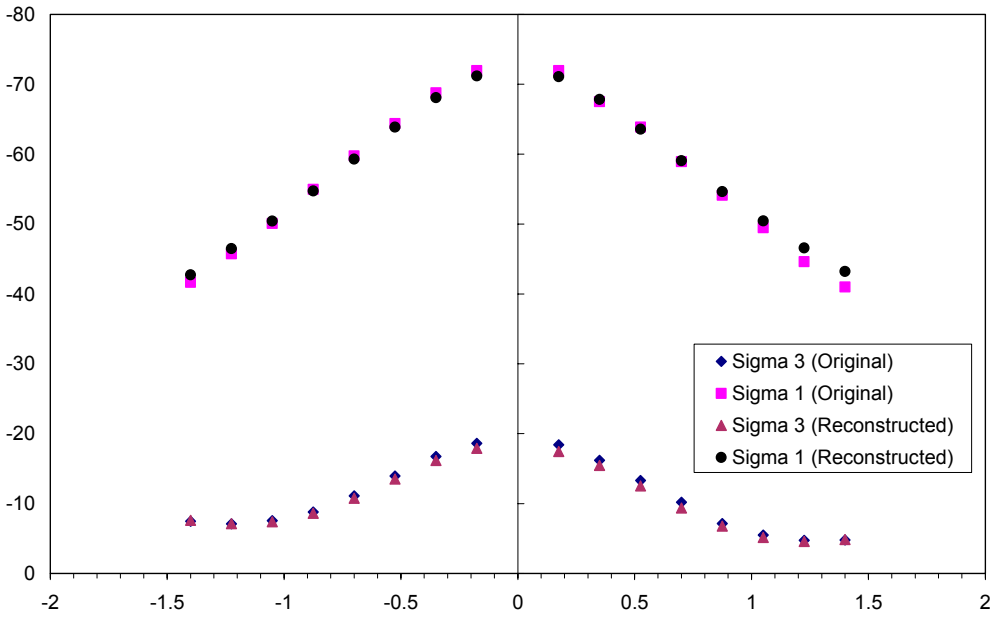

(b)

Figure 4-6. *Comparison of the stresses along horizontal and vertical sections inside pillar at 1.5 m below the tunnel floor. (a) Horizontal section. (b) Vertical section.*

4.3 Reconstruction of stress field after heating

Thermal induced stress distributions calculated by JobFem /Fredrikkson, 2002/, were reproduced with equivalent inverse traction for the pillar model. Figure 4-7 to Figure 4-10 show comparison between the original and the reproduced stress distribution for both major and minor principal stresses at each time steps.

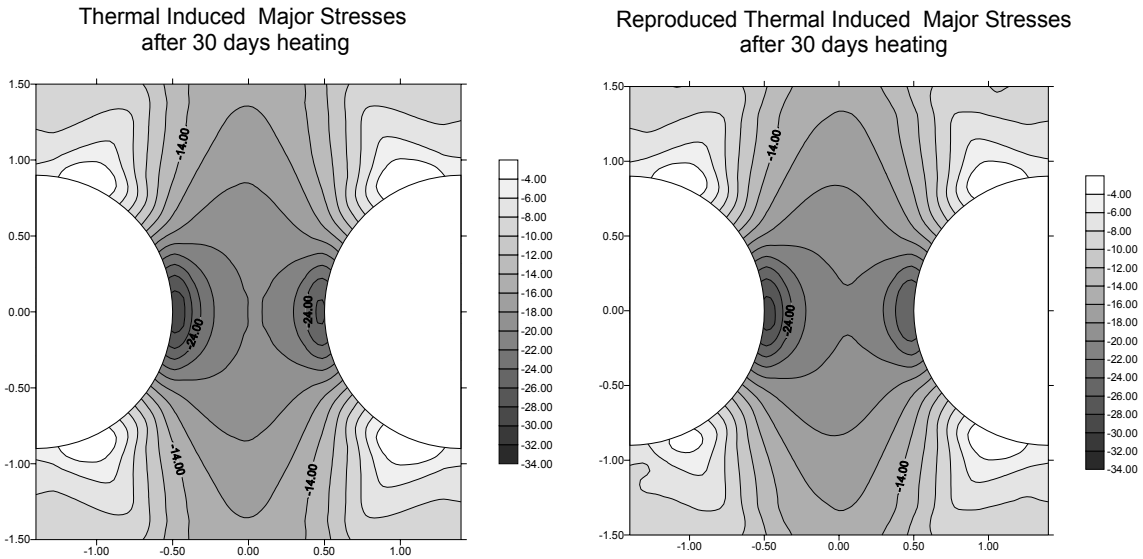

(a)

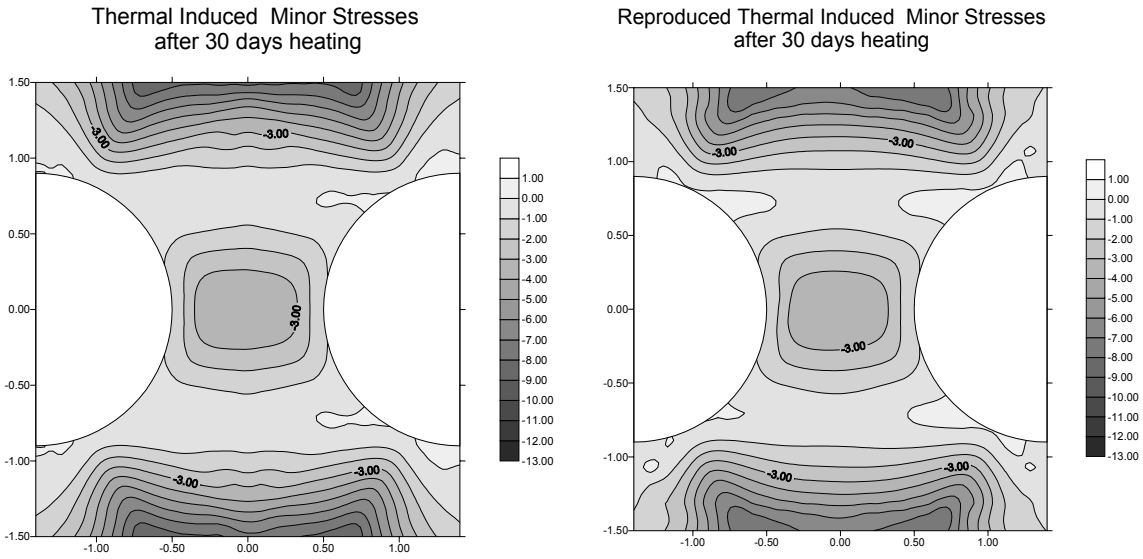

(b)

Figure 4-7. *Comparison between the original and the reproduced stress distribution after 30 days of heating (left: original stress, right: reconstructed stress). (a) Major principal stress (σ_1). (b) Minor principal stress (σ_3).*

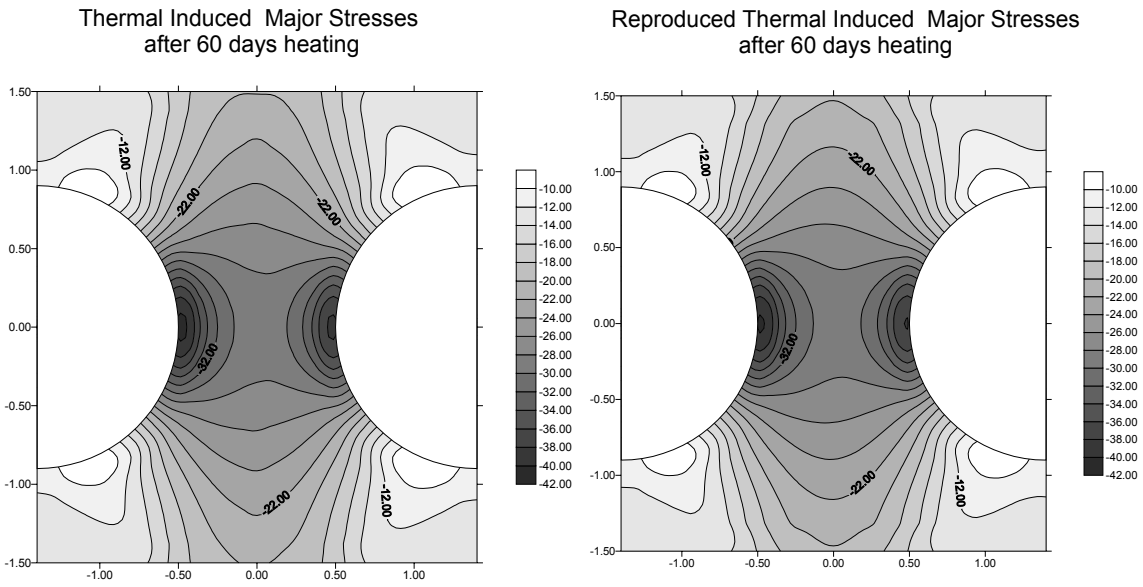

(a)

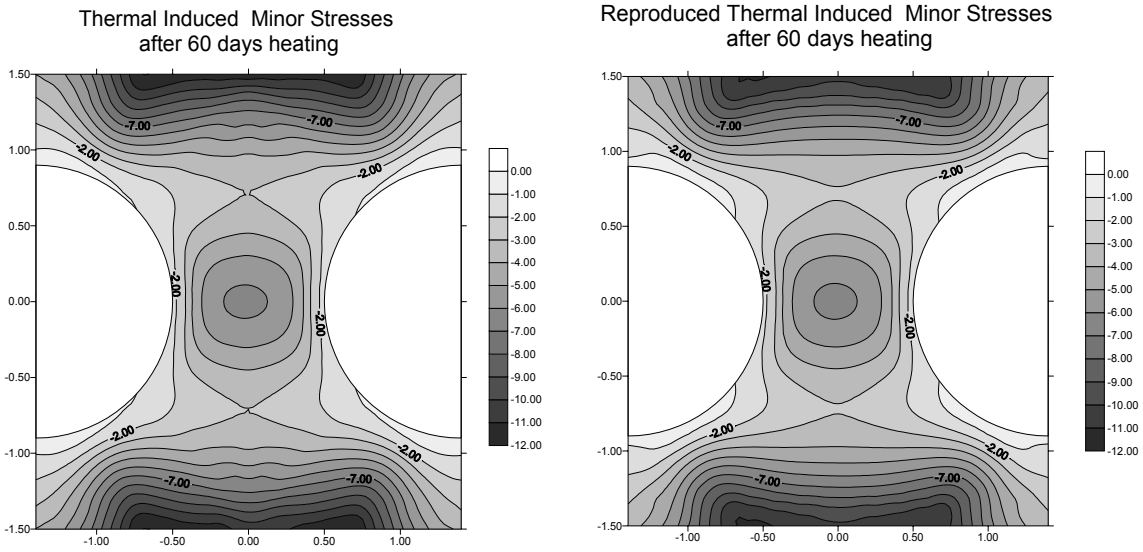

(b)

Figure 4-8. *Comparison between the original and the reproduced stress distribution after 60 days of heating (left: original stress, right: reconstructed stress). (a) Major principal stress (σ_1). (b) Minor principal stress (σ_3).*

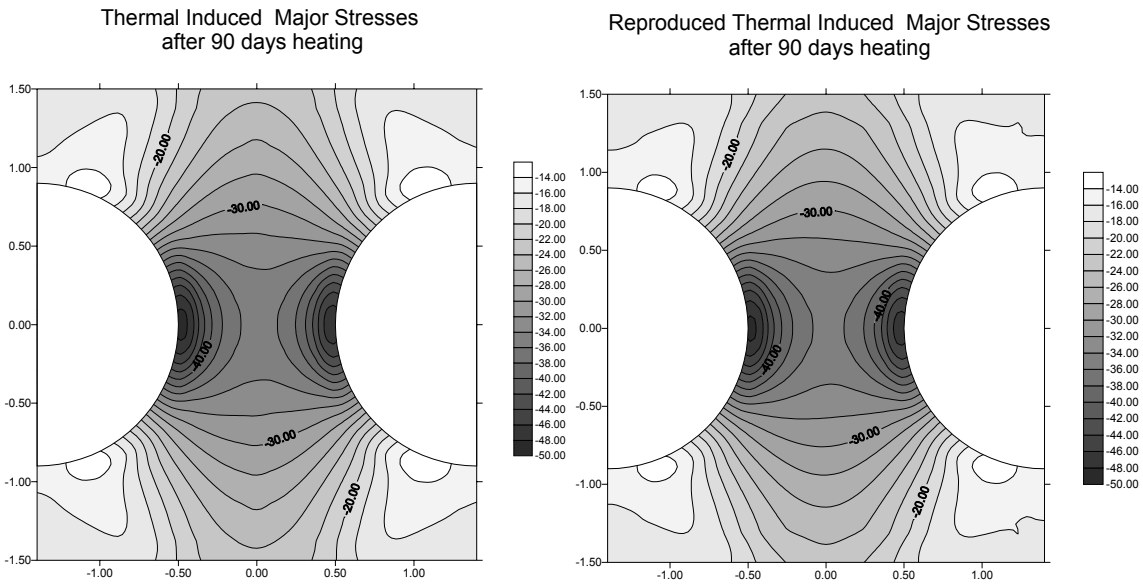

(a)

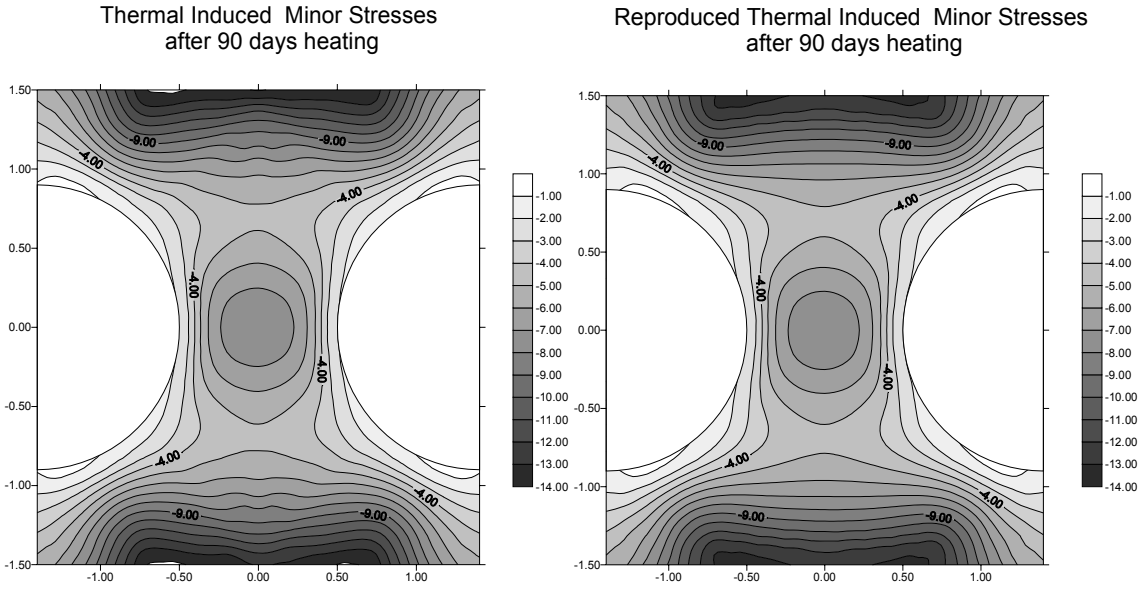

(b)

Figure 4-9. *Comparison between the original and the reproduced stress distribution after 90 days of heating (left: original stress, right: reconstructed stress). (a) Major principal stress (σ_1). (b) Minor principal stress (σ_3).*

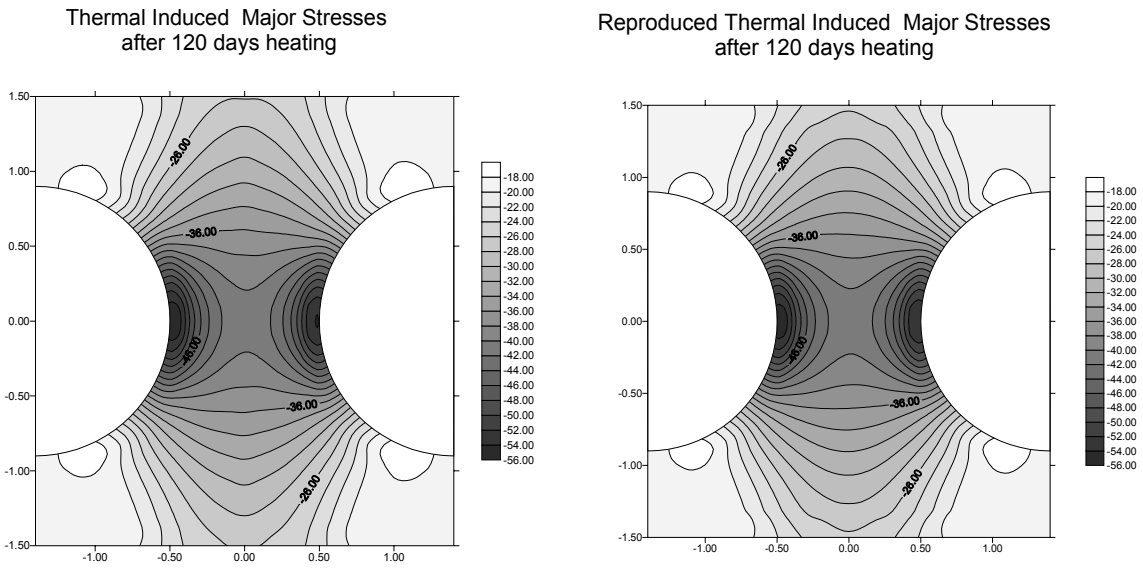

(a)

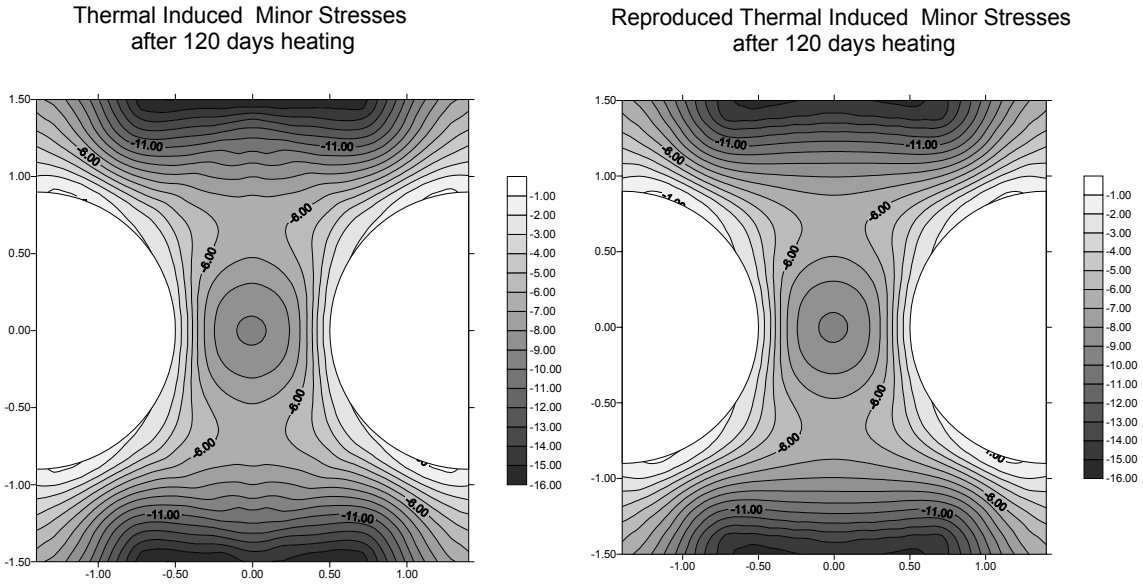

(b)

Figure 4-10. *Comparison between the original and the reproduced stress distribution after 120 days of heating (left: original stress, right: reconstructed stress). (a) Major principal stress (σ_1). (b) Minor principal stress (σ_3).*

All results are from regular SVD solution without truncation, because the accuracy of the stress field was quite similar for all truncation numbers. Compared to the excavation effect, excellent accuracy between two models could be obtained for both major and minor principal stresses as shown in the figures

Table 4-1 lists relative errors at some selected points inside pillar. Stress distributions could be reproduced very well in all cases of time steps. In most cases, errors for the major principal stress show below 1% except in the case of 0.5 m below the tunnel floor. Errors were quite small especially in the case of thermal stresses compare to the case of excavation.

This is because thermal stress field were originally obtained from 2D model. 3D nature of excavation stress field would induce larger error. Even though errors seem to be big at some, real differences can be small because this error is relative one and original values at those points were very small.

Figure 4-11 shows the comparison of stresses along horizontal and vertical sections after 120 days of heating. Stress distribution for other cases showed very similar pattern as Figure 4-9. The reproduced stress distribution at all points showed excellent agreement with the original one, so thermal stress field could be well reproduced with the proposed method.

Table 4-1. Comparison of relative errors at some points (%)

Location		Z=1.5 m		Z=0.5 m		t=30 day		t=60 day		t=90 day		t=120 day	
(x,y)		σ_1	σ_3	σ_1	σ_3	σ_1	σ_3	σ_1	σ_3	σ_1	σ_3	σ_1	σ_3
0.00	0.00	-0.46	-4.76	-4.02	-0.23	0.96	1.09	0.62	0.61	0.52	0.37	0.47	0.21
0.31	0.00	-1.07	-7.51	-3.77	-2.56	0.62	-0.25	0.42	-0.27	0.38	-0.32	0.37	-0.36
0.19	0.00	-0.46	-4.76	-4.49	-5.66	-0.04	-1.18	0.01	-0.86	0.06	-0.76	0.08	-0.72
0.44	0.00	-0.94	-17.87	-5.39	-20.53	-0.86	-1.57	-0.46	-1.28	-0.29	-1.14	-0.20	-1.09
0.00	0.35	0.46	-4.57	-0.04	-4.67	0.47	-3.78	0.14	-1.09	0.03	-0.85	-0.02	-0.74
0.00	0.70	0.24	-7.75	8.44	-10.58	-0.19	-5.57	-0.55	-1.27	-0.69	-0.76	-0.76	-0.53
0.00	1.23	4.40	-3.73	27.88	-26.49	-1.27	6.15	-1.37	3.59	-1.42	3.03	-1.45	2.75

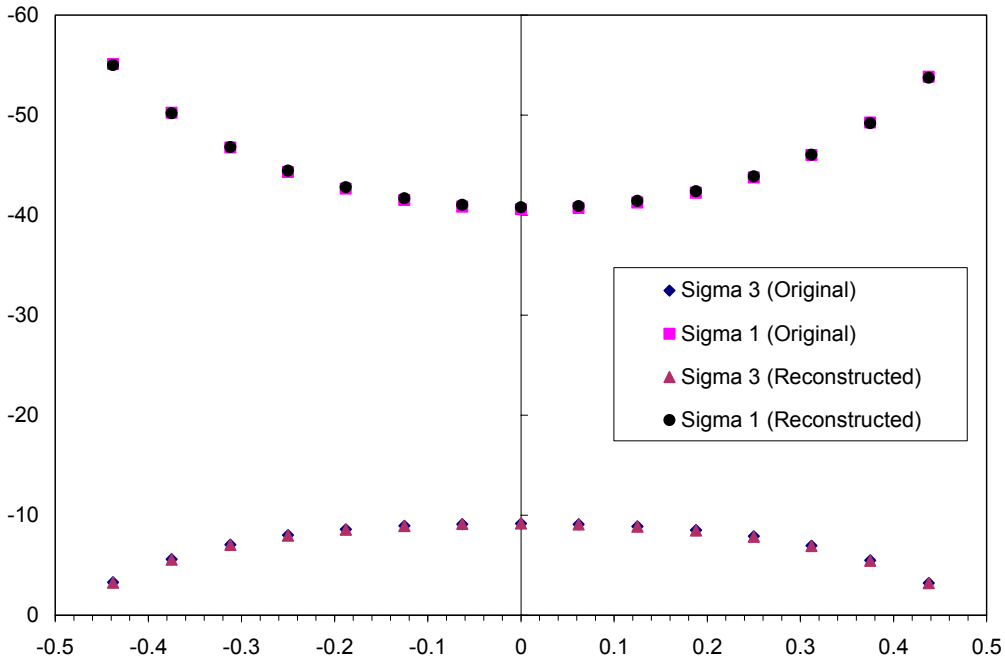

(a)

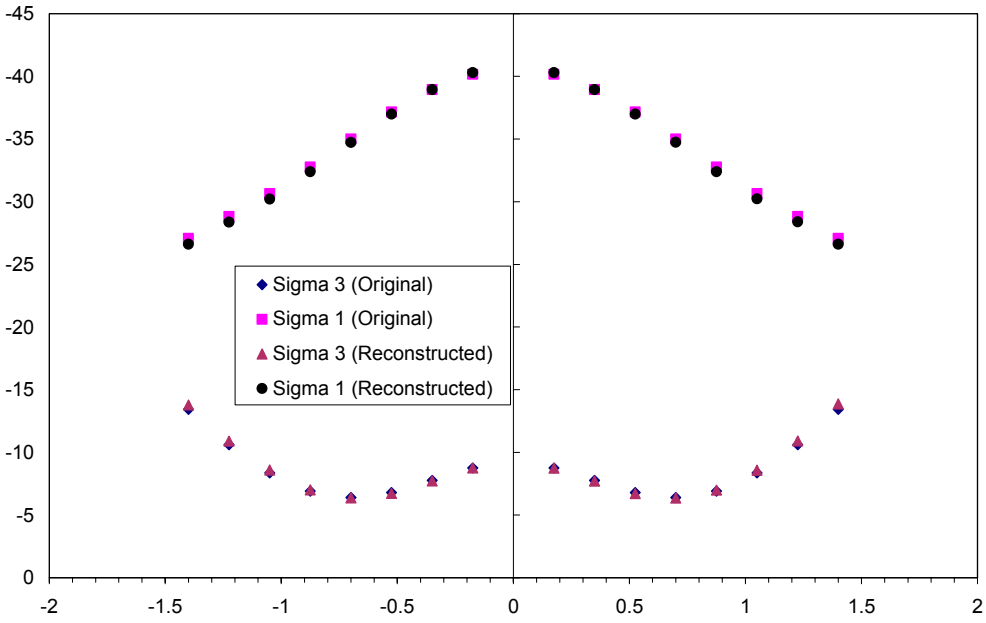

(b)

Figure 4-11. *Comparison of the stresses along horizontal and vertical sections inside pillar after 120 days of heating. (a) Horizontal section. (b) Vertical section.*

5 Conclusions

From the suggested inverse BEM technique, stress distribution inside pillar has been successfully reconstructed. Detailed FRACOD simulation with the reconstructed stresses will be presented in Part I /Rinne et al., 2003/. Conclusions from this work can be summarized as follows:

Overall stress distribution with the suggested pillar model could be well reproduced with sufficient accuracy by the proposed reconstruction method. Using more refined elements and advanced scheme can increase accuracy a lot.

Any stress distribution from other modelling or measurements can be reproduced and used for the FRACOD simulation.

For the pillar model, no other advanced regularization scheme would be needed if the sufficient information of stresses were available.

Reproduced stress field has been successfully used for FRACOD simulation for fracture propagation.

It is expected that more refined model involving excavation and thermal loading with accurate input data can be modelled with the proposed technique and FRACOD when the real in-situ APSE experiments are conducted.

6 References

Andersson C, 2003. Feasibility study. Äspö Pillar Stability Experiment. International Progress Report, IPR-03-01. Swedish Nuclear Fuel and Waste Management Company, Stockholm.

Bezerra L, Saigal S, 1995. Inverse Boundary Traction Reconstruction with the BEM. Int. J. Solids Structures 32(10):1417-1431.

Fredriksson A, Staub I, Janson T, 2003. Design of heaters and preliminary results from coupled 2D thermo-mechanical modelling. Äspö Pillar Stability Experiment. International Progress Report, IPR-03-03. Swedish Nuclear Fuel and Waste Management Company, Stockholm.

Gao XW, Davis TG, 2002. Boundary Element Programming in Mechanics. Cambridge University Press, 252p.

Golub GH, Loan CFV, 1996. Matrix Computation, 3rd edition. The Johns Hopkins University Press, 686p.

Hansen PC, 1992. Regularization Tools: A Matlab Package for Analysis and Solution of Discrete Ill-Posed Problems. Technical University of Denmark.

Staub I, Janson T, Fredriksson A, 2003. Geology and properties of the rock mass around the experiment volume. Äspö Pillar Stability Experiment. International Progress Report, IPR-03-02. Swedish Nuclear Fuel and Waste Management Company, Stockholm.

Lu S, Rizzo FJ, 1999. A Boundary Element Strategy for Elastostatic Inverse Problems involving Uncertain Boundary Conditions. Int. J. Numer. Meth. Engng. 46:957-972.

Martin L, Lesnic D, 2002. Boundary Element Solution for the Cauchy Problem in Linear Elasticity using Singular Value Decomposition. Comput. Methods Appl. Mech. Engrg. 191:3257-3270.

Rinne M, Shen B, Lee HS, 2003. Äspö Pillar Stability Experiment: Modelling of Fracture Stability FRACOD, Part I: Modelling Fracturing Process with Preliminary Data by FRACOD. International Progress Report, IPR-03-05. Swedish Nuclear Fuel and Waste Management Company, Stockholm.

Sakurai S, 1997. Lessons Learned from Field Measurements in Tunnelling. Tunnelling and Underground Space Technology, 12(4):453-460.

Turco E, 2001. An Effective Algorithm for Reconstructing Boundary Conditions in Elastic Solids. Comput. Methods Appl. Mech. Engrg. 190: 3819-3829.

William HP, Saul AT, William TV, Brian PF, 1996. Numerical Recipes in Fortran90. Cambridge University Press, 1486p.

Zhang F, Kassab AJ, Nicholson DW, 1997. A Boundary Element Solution of an Inverse Elasticity Problem and Applications to Determining Residual Stress and Contact Stress. Int. J. Solids Structures 34(16):2073-2086.